

ABSTRACT

Title of Document: ESTIMATING SURFACE LONGWAVE
RADIATION AND APPLICATIONS TO HIGH
LATITUDE ISSUES

Eric A. Nussbaumer, Doctor of Philosophy, 2012

Directed By: Professor Rachel T. Pinker
Department of Atmospheric and Oceanic Science

Two models, with distinct advantages for calculating downwelling surface longwave (DSLW) radiation under all sky conditions are presented. Both models are driven with a combination of Moderate Resolution Imaging Spectroradiometer (MODIS) level-3 cloud parameters and information from the European Centre for Medium-Range Weather Forecasts (ECMWF) ERA-Interim model. To compute the clear sky component of DSLW the first model DSLW/UMD v1 utilizes a globally applicable parameterization. The second generation model DSLW/UMD v2 utilizes a two layer feed-forward artificial neural network with sigmoid hidden neurons and linear output neurons. When computing the cloud contribution to DSLW, DSLW/UMD v1 implements a commonly used statistical model to calculate cloud vertical height while in DSLW/UMD v2 the cloud base temperature is estimated by using an independent artificial neural network based on spatially and temporally co-

located MODIS and Cloudsat Cloud Profiling Radar (CPR) and the Cloud-Aerosol Lidar and Infrared Pathfinder Satellite Observation (CALIPSO) Cloud-Aerosol Lidar with Orthogonal Polarization (CALIOP) observations. Daily average estimates of DSLW for 2003 to 2009 are compared against ground measurements from the Baseline Surface Radiation Network (BSRN) and show significant improvements over currently available model estimates.

DSLW/UMD v2 as optimized for Polar Regions along with a UMD developed shortwave model are used to investigate the role of radiative components in Arctic sea ice anomalies. The correlation between downwelling surface longwave and shortwave radiation and sea ice anomaly for the period from 2003 to 2007 is investigated using the latest Moderate Resolution Imaging Spectroradiometer (MODIS) level-3 cloud parameters and information from the European Centre for Medium-Range Weather Forecasts (ECMWF) ERA-Interim model. All sky downwelling surface longwave radiation (DSLW), all sky downwelling shortwave radiation (DSSW), all sky total downwelling shortwave and longwave radiation (DSSW + DSLW), and cloud total cloud forcing are individually examined to determine their respective correlation to sea ice anomaly. It is determined that these radiation components are not the primary drivers for major sea ice anomalies that occur during the investigated time frame within the 120°E to 210°E region.

ESTIMATING SURFACE LONGWAVE RADIATION AND APPLICATIONS TO
HIGH LATITUDE ISSUES

By

Eric A. Nussbaumer

Dissertation submitted to the Faculty of the Graduate School of the
University of Maryland, College Park, in partial fulfillment
of the requirements for the degree of
Doctor of Philosophy
2012

Advisory Committee:
Professor Rachel T. Pinker, Chair
Professor Hugo Berbery
Professor Michael Evans
Professor Robert Hudson
Professor Sumant Nigam

© Copyright by
Eric Nussbaumer
2012

Acknowledgements

I am deeply indebted to the following people: Rachel Pinker, Kshama Jaiswal, and my parents. Without their kindness and guidance this would not be possible.

Table of Contents

Acknowledgements	ii
Table of Contents	iii
List of Tables	vi
List of Figures	viii
Acronym List	xiv
Chapter 1: Introduction	1
1.1. Introduction	1
1.2. Motivation and Objectives	3
1.3. Statement of Originality	4
Chapter 2: Developing Models for DSLW	8
2.1. Abstract	8
2.2. Parameterizations and Artificial Neural Networks	10
2.3. Clear Sky Contribution	13
2.3.1. DSLW/UMD v1	13
2.3.2. DSLW/UMD v2	18
2.4. Cloud Contribution	23
2.4.1. DSLW/UMD v1	24
2.4.2. DSLW/UMD v2	26
Chapter 3: Validation and Comparison	30
3.1. Abstract	30

3.2.	Clear Sky Component	30
3.2.1.	DSLW/UMD v1	30
3.2.2.	DSLW/UMD v2	32
3.3.	Evaluation of the Cloud Base Temperature Model	34
3.4.	All Sky Component	37
3.4.1.	DSLW/UMD v1	40
3.4.2.	DSLW/UMD v2	51
3.5.	Conclusion	72
Chapter 4:	Application to Arctic Sea Ice Melt	75
4.1.	Abstract	75
4.2.	Methodology	78
4.2.1.	Downwelling Surface Longwave Radiation (DSLW)	78
4.2.2.	Downwelling Surface Shortwave Radiation (DSSW)	80
4.2.3.	Sea Ice Data	82
4.2.4.	Equal Area Comparison	83
4.3.	Results	83
4.3.1.	Cloud Fraction and Arctic Sea Ice Melt Area	83
4.3.2.	Radiant Exposure	91
4.3.3.	DSSW	94
4.3.4.	DSLW	103
4.3.5.	DSLW + DSSW	105
4.3.6.	Cloud Forcing	105
4.4.	Conclusion	108

Chapter 5:	Conclusions and Future Plans	110
5.1.	Conclusions and Summary	110
5.2.	Future Plans	112

List of Tables

Table 2.1 Input and output parameters for the clear sky artificial neural network.	22
Table 2.2 Input and output parameters for the cloud base temperature artificial neural network.	27
Table 3.1 Statistical comparison between the clear sky contribution to DSLW from DSLW/UMD v2 (MODIS) artificial neural network and the Rapid Radiative Transfer Model (RRTM).....	33
Table 3.2 Information on DSLW/UMD v1 and four commonly used radiative transfer based methods for calculating DSLW, including name of radiative transfer model or parameterization, resolution of global DSLW, cloud input source, and primary source for temperature and humidity profiles.	40
Table 3.3 Statistics for daily average comparison of DSLW predicted by each model compared with BSRN ground station observations for each year. Statistics include correlation coefficient, bias, root mean square error, and number of ground stations included in analysis.	43
Table 3.4 Statistics for daily average comparison of DSLW predicted by each model compared with BSRN ground station observations for each year. Statistics include correlation coefficient, bias, and root mean square error.	54
Table 3.5 Total global clear sky, cloud forcing, and all sky DSLW for each year between 2003 and 2009 along with average aggregated overall years.	69
Table 4.1 A summary of the correlation statistics between DSLW estimated from the DSLW/UMD v2 Polar model and two ARM ground stations. Comparison was	

done on a daily and monthly time scale.....	79
Table 4.2 A summary of the correlation statistics between DSSW estimated from the DSLW/UMD v2 Polar model and two ARM ground stations. Comparison was done on a daily and monthly time scale.....	82
Table 4.3 A summary of the cloud fractions averaged over June, July and August for years 2003 to 2007 for each region discussed in this section. Red numbers indicate the lowest cloud fraction for melt year.....	91
Table 4.4 Maximum value of radiant exposure for DSSW, DSLW, DSSW + DSLW, and Cloud Forcing cumulated from the beginning of the year. Red values indicate the largest occurring value for each type of radiant exposure for time period 2003 to 2007.	94
Table 4.5 Radiant exposure for DSSW, DSLW, DSSW + DSLW, and Cloud Forcing cumulated from the beginning of the year to melt onset (June). Red values indicate the largest occurring value for each type of radiant exposure for time period 2003 to 2007.	96

List of Figures

- Figure 2.1 A single neuron with N inputs. Where, X_i , W_i , and Θ_i represent the input value, weight and bias for the i th input. The activation function is represented by f and can be either linear or non-linear. Each input is multiplied by its respective weight and then added to its bias, which is summed over all inputs. The activation is applied to the sum over all inputs giving the output of the neuron. Each neuron is associated with one output. 11
- Figure 2.2 A density plot of the effective clear sky emissivity versus the total column water vapor. The clear sky effective emissivity is given as the ratio of the DSLW calculated by RRTM over DSLW calculated by the Stefan-Boltzmann law using the screen level temperature. The x-axis is the total column water vapor from ERA-Interim re-analysis data. The black line is the 3rd order rational fit of the DSLW/UMD v1 parameterization for effective emissivity. The color scale is given as \log_{10} of the density. All values are based on daily data from 2007. 17
- Figure 2.3 The bars represent the contribution to total DSLW from each layer of the atmosphere from the surface to a specified height above the surface for two ground stations calculated using Radiosonde data and RRTM. Radiosonde data are taken from the island nation of Nauru in the South Pacific (0.521° N; 166.9° E) representing a warm humid climate, and the German Polar Research Station, Georg von Neumayer (70.65° N; 8.25° E) in Antarctica representing a cold dry climate with a slight temperature inversion. 19

Figure 2.4 Algorithm to calculate cloud base temperature from *Wang et al.* (2000) statistical model. 26

Figure 3.1 A plot comparing the clear sky contribution to DSLW as calculated by RRTM versus the UMD parameterization. The color scale is given as \log_{10} of the density. All values are based on daily data from 2007. 31

Figure 3.2 Comparison of the DSLW/UMD v2 (MODIS) artificial neural network model (x-axis) and the RRTM (y-axis) for calculation of the clear sky contribution to DSLW for daily averages of 2007. Because of the large number of data points used in the comparison and high overlap colors are used to indicate the \log_{10} density of observations. 34

Figure 3.3 Comparison of cloud base temperature observed by CPR and CALIOP in 2008 vs temperature calculated from DSLW/UMD v2 artificial neural network (top) and the cloud thickness model from *Wang et al.* 2000 (bottom). 36

Figure 3.4 A global map showing the locations of the BSRN ground stations used in the analysis. 37

Figure 3.5 A plot of DSLW/UMD v1 derived data versus BSRN ground stations for each year and for aggregated years 2003 to 2007. The black line follows a one-to-one comparison. The color scale is given as \log_{10} of the density. The bias and RMS are given in $W m^{-2}$ 41

Figure 3.6 A plot of the model derived DSLW (DSLW/UMD, ISCCP-FD, ERA-Interim, GEWEX-SRB, GEWEX-QC, and NCEP-DOE II) versus the BSRN ground station measured values. The black line follows a one-to-one

comparison. The color scale is given as \log_{10} of the density. All values are based on daily data from 2003 to 2007. The bias and RMSE are given in $W m^{-2}$ 45

Figure 3.7 A sample plot of monthly averaged DSLW calculated from DSLW/UMD v1 and the difference between DSLW/UMD v1 and ERA-Interim, NCEP DOE II and ISCCP. For the difference plots a negative value indicates that a particular model predicts a higher value of DSLW compared to the DSLW/UMD v1 model. 47

Figure 3.8 Zonally and globally averaged daily DSLW for 2003-2007 for all models used in comparison. 48

Figure 3.9 In the first five panels, the bars for each model represent the average value of RMSE ($W m^{-2}$) for each month for the combined years 2003 to 2004. The comparison is broken down into latitudinal regions: Tropical (blue), Mid-Latitude (green), and Polar (red). The black line is the mean RMSE of all ground stations for the entire period. The last graph depicts the averaged total column water vapor ($kg m^{-2}$) derived from ERA-Interim re-analysis broke down by month and region. The lines correspond to 2-meter surface temperature from ERA-Interim re-analysis. The blue line represents the Tropical, green the Mid-Latitudes, and the red corresponds to the Polar Regions. 50

Figure 3.10 Model derived DSLW data versus BSRN ground stations aggregated over 2003 to 2007. The black line follows a one-to-one comparison. The color scale is given as \log_{10} of the density. GEWEX QC is a parameterization based

quality control check for GEWEX SRB.	57
Figure 3.11 A colored circle is given at the geospatial location of each BSRN ground station. The color of each circle indicates the RMSE (W m^{-2}) between each model and BSRN ground station for daily averages (2003-2007).....	58
Figure 3.12 The bars for each model represent the average value of RMSE	60
Figure 3.13 The time-series for monthly averaged DSLW calculated by DSLW/UMD v2 from MODIS and DX and measured by a BSRN ground station. DSLW as calculated from DSLW/UMD v2 is taken from the grid cell that includes the BSRN ground station. The GCR BSRN ground station is located at Goodwin Creek in Mississippi, USA. SPO BSRN ground station is located at the South Pole in Antarctica.....	62
Figure 3.14 Top two figures show the monthly averaged cloud fraction as given by MODIS and ISCCP-DX over GCR and SPO BSRN ground stations. The bottom two figures show the monthly averaged cloud top pressure as given by MODIS and ISCCP-DX over GCR and SPO BSRN ground stations.	64
Figure 3.15 Lines represent zonally averaged all sky DSLW each model taken from daily data averaged over 2003 to 2007. The total global average for each model is also given.....	66
Figure 3.16 Solid-line represents the zonally averaged clear sky contribution to DSLW for all years 2003 to 2009. The dashed-line represents the cloud contribution to DSLW for all years 2003 to 2009. DSLW is calculated from DSLW/UMD v2 (MODIS) model. Shaded region represents the bounds as given by daily data averaged for each year between 2003 and 2009.....	67

Figure 3.17 Plots of the clear sky and cloud contribution to DSLW from daily values averaged over 2007. DSLW calculations are from DSLW/UMD v2 (MODIS) model..... 68

Figure 3.18 Monthly and zonally averaged clear sky DSLW and cloud forcing DSLW for 2003 to 2009..... 71

Figure 4.1 Comparison of monthly averaged values of DSSW, DSLW, and DSSW + DSLW, as calculated by the UMD models and observed by ground stations (NSA and NYA) for the period 2003-2007. 80

Figure 4.2 Time-series of Arctic sea ice concentration anomalies for different regions of the Arctic. Graphs c) and d) make up the region analyzed by *Kay et al.* (2008), 180° E to 240° E. Graphs a) and b) show additional regions displaying the characteristic 2007 large decrease in sea ice with the region 150° E to 180° E showing the largest anomaly. 85

Figure 4.3 Monthly averaged Arctic sea ice concentration anomaly for October 2007. This time represents when the 2007 sea ice concentration anomaly was at its largest (negative) value. 86

Figure 4.4 Monthly averaged daytime cloud fraction from MODIS using both Aqua and Terra spacecraft over 180° E to 210° E and 70° N to 90° N region. 87

Figure 4.5 Monthly averaged daytime cloud fraction from MODIS using both Aqua and Terra spacecraft over 180° E to 210° E and 70° N to 90° N region. 88

Figure 4.6 Monthly averaged daytime cloud fraction from MODIS using both Aqua and Terra spacecraft over 120° E to 210° E and 70° N to 90° N region. 90

Figure 4.7 Shows the cumulated radiant exposure for DSSW (a), DSLW (b), DSSW +

DSLW (c), and Cloud Forcing (d) cumulated from the beginning of each year along with the monthly averaged sea ice concentration anomaly. The solid line represents the area from 120° E to 210° E while the dashed line represents ... 93

Figure 4.8 Maximum radiant exposure (blue bar) and radiant exposure cumulated until melt onset (red bar) for years 2003-2007 for DSSW (a), DSLW (b), DSSW + DSLW (c), and Cloud Forcing (d)..... 95

Figure 4.9 Plots a) through d) show the spatial distribution of the change in radiant exposure between melt onset (June) and the maximum decrease in sea ice concentration anomaly for 2007 (October). Plot e) shows the monthly average of the spatial distribution of the sea ice concentration anomaly for October 2007. Grey areas indicate areas with no change in radiant exposure or sea ice concentration anomaly. 98

Figure 4.10 Monthly averaged DSSW for 120° E to 210° E and 70° N to 90° N. 99

Figure 4.11 Monthly averaged irradiance (blue line) for DSSW (a), DSLW (b), DSSW + DSLW (c), and Cloud Forcing (d), monthly averaged observed sea ice concentration (black solid line) and monthly averaged sea ice concentration from climatology (black dashed line) bounded by 120° E to 210° E/70° N to 90° N. 101

Figure 4.12 The cross correlation between radiative components and Arctic sea ice concentration for region 120° E to 210° E and 70° N to 90° N. A negative lag corresponds to radiation signal preceding the sea ice signal and a positive signal corresponds to the opposite. The dashed line indicates the 95% confidence interval..... 102

Acronym List

AER.....	Atmospheric and Environmental Research
AIRS.....	Atmospheric InfraRed Sounder
AMSR-E.....	Advanced Microwave Scanning Radiometer – Earth Observing System
ARM.....	Atmospheric Radiation Measurement
BSRN.....	Baseline Surface Radiation Network
CALIOP.....	Cloud-Aerosol Lidar with Orthogonal Polarization
CALIPSO.....	CloudSat and Cloud-Aerosol Lidar and Infrared Pathfinder Satellite
CAM.....	Community Atmospheric Model
CISL.....	Computational and Information Systems Laboratory
DISC.....	Data and Information Services Center
DMSP.....	Defense Meteorological Satellite Program
DOE.....	Department of Energy
DSLW.....	Downwelling Surface Longwave Radiation
DSSW.....	Downwelling Surface Shortwave Radiation
ECMWF.....	European Centre for Medium-Range Weather Forecasts
ESRL.....	Earth System Research Laboratory
GCM.....	Global Circulation Model
GDAS.....	Global Data Assimilation System
GES.....	Goddard Earth Sciences

SRB.....Surface Radiation Budget
SSM/I..... Special Sensor Microwave/Imager
TIROS.....Television Infrared Observation Satellite
TOA.....Top Of the Atmosphere
TOVS..... TIROS Operational Vertical Sounder
UMD.....University of Maryland, College Park
USGS.....United States Geological Survey
WCRP.....World Climate Research Programme
WRMC.....World Radiation Monitoring Center

Chapter 1: Introduction

1.1. Introduction

Surface energy balance plays a key role in many atmospheric and oceanic processes. On a global scale, the surface energy budget is closely tied to the hydrological cycle and to the atmospheric heat budget (*Mitchell 1983; Mitchell et al. 1987; Boer 1993; Allen and Ingram 2002*). An important component of the surface energy budget and one of the most difficult to model is downwelling surface longwave radiative flux (DSLW). Information on surface longwave fluxes at global scales are required by many research programs as identified in the Global Energy and Water Cycle Experiment (GEWEX) research plan (*WCRP-5 1985*).

In-situ measurements of DSLW, while most accurate, are geographically limited. Satellites offer an alternative for calculating such fluxes and have the advantage of global coverage. Passive satellite instruments measure radiances emerging from the top of the atmosphere (TOA), which can be directly used to calculate outgoing longwave radiation (OLR). However, these measurements are decoupled from DSLW which is determined by the atmospheric structure and is not directly observable from TOA (*Stephens et al. 1984; Ramanathan 1986; Zhou et al. 2007*). In order to derive surface longwave fluxes from satellites, one must rely on either active sensors or auxiliary information on atmospheric structure. Detailed information on the vertical profiles of absorbing species and cloud

properties are necessary to accurately calculate DSLW.

There are several factors specific to the longwave that make retrieval of surface fluxes from models difficult. Various atmospheric gases have strong absorption and emission properties, of which the largest contributors are water vapor, carbon dioxide, and ozone. Minor constituents are methane, nitric oxide, carbon monoxide, and nitrous oxide. Water vapor, which is highly variable both spatially and temporally, is by far the single most important atmospheric absorber in the longwave region (10 to 3250 cm^{-1}). Water vapor can range from 10 ppm in cold dry regions and up to 5% by volume in hot humid regions (*Wallace et al.* 2006). Spatially, water vapor amount is influenced by the local hydrological cycle (evaporation, condensation, and precipitation), which is governed by land/ocean location and local biodiversity and atmospheric transport from semi-permanent atmospheric features such as stationary planetary waves. Temporally, water vapor is controlled by temperature (e.g., diurnal temperature cycle) and atmospheric transport, occurring locally and on relatively small time scales.

In addition, retrieval of cloud vertical structure from satellite observations is problematic. The Earth's atmosphere contains several radiative windows in which longwave energy can pass through with little absorption such as between 8 and 12 μm . Clouds can fill in this window preventing energy from escaping through scattering and absorption thereby having an effect on the surface energy balance. It is not enough to just detect the presence of clouds, but one must also be able to observe the vertical structure. Following the Stefan-Boltzmann law the longwave emissive power is proportional to the T^4 , where T is the temperature.

The cloud base temperature, which is the main source of cloud emission to the ground, is highly dependent on the cloud base height; therefore, it is important to know the cloud top height and vertical structure. The situation becomes even more complex due to multiple cloud layers (occurring 42% of the time) with a predominate mode of two layers (*Wang et al. 2000*). Passive satellite sensors can provide information at a global scale but are limited to sensing cloud top properties. Active satellite sensors such as the Cloud-Aerosol Lidar with Orthogonal Polarization (CALIOP) and the Cloud Profiling Radar (CPR) can provide the necessary information on the cloud vertical structure; however, not at full global coverage.

1.2. Motivation and Objectives

DSLW is among the largest components of the globally averaged surface energy balance and is fundamental for reliable weather prediction, climate simulation, and land surface modeling (*Wild et al. 2001*). It is also among the most difficult components to estimate because of its decoupled nature from top of the atmosphere satellite observations and its complex dependence on the vertical structure of atmospheric parameters such as temperature, water vapor, and clouds.

Many scientific programs including The Global Energy and Water Cycle Experiment (GEWEX) have identified a need for surface energy budgets with an accuracy of 10 W m^{-2} (*WCRP-5 1985*). Current models show daily average accuracies (when compared to ground station observations) between 22 and 31 W m^{-2} (*Nussbaumer and Pinker 2011*) and therefore, significant improvement

in estimating DSLW is needed. This is especially true in Polar Regions where models show the greatest disagreement with ground observations and clouds play a critical role in the surface radiation budget. To this end, we develop a new model to estimate DSLW based on the latest high resolution meteorological data from ERA-Interim re-analysis and cloud data from 1° MODIS level-3 cloud parameters. In addition, we evaluate current models to identify areas of potential improvement in estimating DSLW. With these areas identified we further develop a new model which incorporates artificial neural networks. With better estimate of DSLW from the new model we evaluate the role of radiation in the Arctic sea ice concentration anomalies from 2003 to 2007.

1.3. Statement of Originality

This document contains original scientific content produced by the author.

Significant scientific contributions include:

- Development of a parameterization model (DSLW/UMD v1) to calculate DSLW based on the latest high resolution ERA-Interim re-analysis and 1° MODIS level-3 cloud parameters. This included the development of a parameterization with global applicability to calculate the clear sky contribution to DSLW based on radiative transfer model runs. Previous parameterizations were based on a small sample of data points with limited spatial and temporal resolution. DSLW/UMD v1 clear sky parameterization was developed using global ERA-Interim re-analysis

data (over 42 million data points) and therefore has global applicability.

- Evaluation of DSLW/UMD v1 along with several other present day models used to calculate DSLW against a worldwide network of ground station observation. Evaluation reveals that the DSLW/UMD v1 model has better agreement to ground observations than the other models that were evaluated and shows areas needing improvement in estimating DSLW.
- Based on the evaluation of DSLW/UMD v1 and other models, highlighting areas of needed improvement for estimating DSLW, a new model is developed (DSLW/UMD v2) utilizing artificial neural networks to calculate the clear sky and cloud contribution to DSLW.
- An artificial neural network for calculating clear sky DSLW is developed based on the Rapid Radiative Transfer Model (RRTM). Comparison with RRTM shows that the artificial neural network does an excellent job estimating clear sky DSLW with significant reduction in computation time and input data.
- An artificial neural network is developed to predict cloud base temperature based on data derived from an algorithm that co-located MODIS passive instrument data to Cloudsat Cloud Profiling Radar (CPR) and Cloud-Aerosol Lidar and Infrared Pathfinder Satellite Observation (CALIOP) active instrument data. Evaluation shows that the artificial neural network significantly improves the estimate of cloud base temperature over the model developed by *Wang et al.* (2000).

- Evaluation of DSLW/UMD v2 shows improvement over its predecessor (v1) especially in the high latitude regions.
- A modified version of DSLW/UMD v2 is developed (DSLW/UMD v2 Polar) specifically to estimate DSLW in the Polar Regions by training the artificial neural networks with high latitude data exclusively.
- DSLW data from DSLW/UMD v2 Polar and downwelling surface shortwave data (DSSW) from a UMD developed model utilizing MODIS data are used to determine role of radiation in the Arctic sea ice anomalies between 2003 and 2007. Analysis shows that DSLW, DSSW, and cloud forcing were not the primary drivers of the Arctic sea ice anomalies for this time period.

Papers published or in the process of being published and awards based on this work:

- 1) Outstanding Presentation at the World Climate Research Programme (WCRP) Conference, Denver, Colorado (October 2011).
- 2) Nussbaumer, E. A., and R. T. Pinker, 2011: Estimating surface long-wave radiative fluxes at global scale. *Q. J. R. Meteorol. Soc.*, DOI: 10.1002/qj974.
- 3) Nussbaumer, E. A., and R. T. Pinker, 2012: Estimating surface longwave radiative fluxes from satellites utilizing artificial neural networks, *J. Geophys. Res-Atmos.* (in press).

- 4) Nussbaumer, E. A., and R. T. Pinker, 2012: The role of shortwave and longwave radiation in Arctic sea ice from 2003 to 2007. *J. Climate.*, (to be submitted).

Chapter 2: Developing Models for DSLW

2.1. Abstract

Two novel approaches for calculating downwelling surface longwave (DSLW) radiation under all sky conditions are presented. The first model (DSLW/UMD v1) is based on parameterizations to calculate clear sky and cloud contribution while the second one (DSLW/UMD v2) utilizes artificial neural networks. Both models are driven with a synthesis of the latest 1° resolution Moderate Resolution Imaging Spectroradiometer (MODIS) level-3 cloud parameters and information from the European Centre for Medium-Range Weather Forecasts (ECMWF) ERA-Interim model.

The clear sky contribution from DSLW/UMD v1 is parameterization based on the Rapid Radiative Transfer Model (RRTM) (*Mlawer et al. 1997*) and is globally applicable, while a statistical cloud structure model and parameterization determine the cloud contribution to DSLW. In DSLW/UMD v2 a two layer feed-forward artificial neural network with sigmoid hidden neurons and linear output neurons is implemented and trained with simulations derived from runs of the Rapid Radiative Transfer Model (RRTM).

Both versions of DSLW/UMD rely on a parameterization to calculate the cloud contribution to DSLW that is dependent on cloud base temperature. In DSLW/UMD v1 the cloud based temperature is determined by a statistical model by *Wang et al. (2000)* to determine the cloud vertical height. When computing the

cloud contribution to DSLW from DSLW/UMD v2, the cloud base temperature is estimated by using an independent artificial neural network approach of similar architecture as previously mentioned, and parameterizations. The cloud base temperature neural network approach is trained using spatially and temporally co-located MODIS and Cloudsat Cloud Profiling Radar (CPR) and CALIPSO Cloud-Aerosol Lidar with Orthogonal Polarization (CALIOP) observations. The MODIS data were acquired as part of the activities of NASA's Science Mission Directorate, and are archived and distributed by the Goddard Earth Sciences (GES) Data and Information Services Center (DISC) [http://modis-atmos.gsfc.nasa.gov/MOD08_D3/index.html]. The CALIOP/CPR data were taken from the CloudSat Data Processing Center [<http://www.cloudsat.cira.colostate.edu/dataHome.php>].

Daily averaged estimates of DSLW for 2003 to 2007 (2009 v2) along with four commonly used methods based on radiative transfer (RT) theory are compared against ground measurements from the Baseline Surface Radiation Network (BSRN) (*World Radiation Monitoring Center – Baseline Surface Radiation Network* http://www.bsrn.awi.de/en/data/data_retrieval_via_pangaea/). It is shown that for all four years, both versions perform as well or better than the available RT based models when evaluated against BSRN measurements, while v2 is an improvement over v1. Further analysis shows that when ground measurements are stratified into Tropical, Mid-Latitude, and Polar Latitudinal belts, largest discrepancies against ground truth for all models are found in the Polar Regions.

2.2. Parameterizations and Artificial Neural Networks

Parameterizations are a way to represent a physical process using a set of predefined variables that are important to the process. They are often employed when actual calculation of the governing equations is too computationally extensive or the full set of input data is unknown. Parameterizations for DSLW are given in terms of easily measurable parameters such as surface temperature, humidity, and water vapor. They are usually separated into a clear-sky flux and a cloudy contribution which typically involve the Stefan-Boltzmann law modified by emissivity. The emissivity is directly related to the transmissivity through absorption. This implies that the emissivity is governed by the vertical distribution of absorbing constituents and the vertical temperature profile.

At global coverage at high resolution of re-analysis and satellite observations, the amount of data to process is formidable. The inherent parallel distributed processing structure of artificial neural networks makes them an ideal candidate for determining DSLW from a vast volume of observations.

We define an artificial neural network as a pool of processing units or neurons that communicate to each other via transmitting signals over a number of weighted connections (*Krose and van der Smagt 1996*). Figure 2.1 illustrates a single neuron, which utilizes the summation of the weighting functions (a product of the weight times the input) with N inputs. For a layer of M neurons the outputs for a layer is represented by the following equation:

$$y = f(wx + \theta) \tag{2.1}$$

where y is a $M \times 1$ output vector

f is the activation function

w is a $M \times N$ synaptic weighting matrix

x is a $N \times 1$ input vector

θ is a $N \times 1$ bias vector

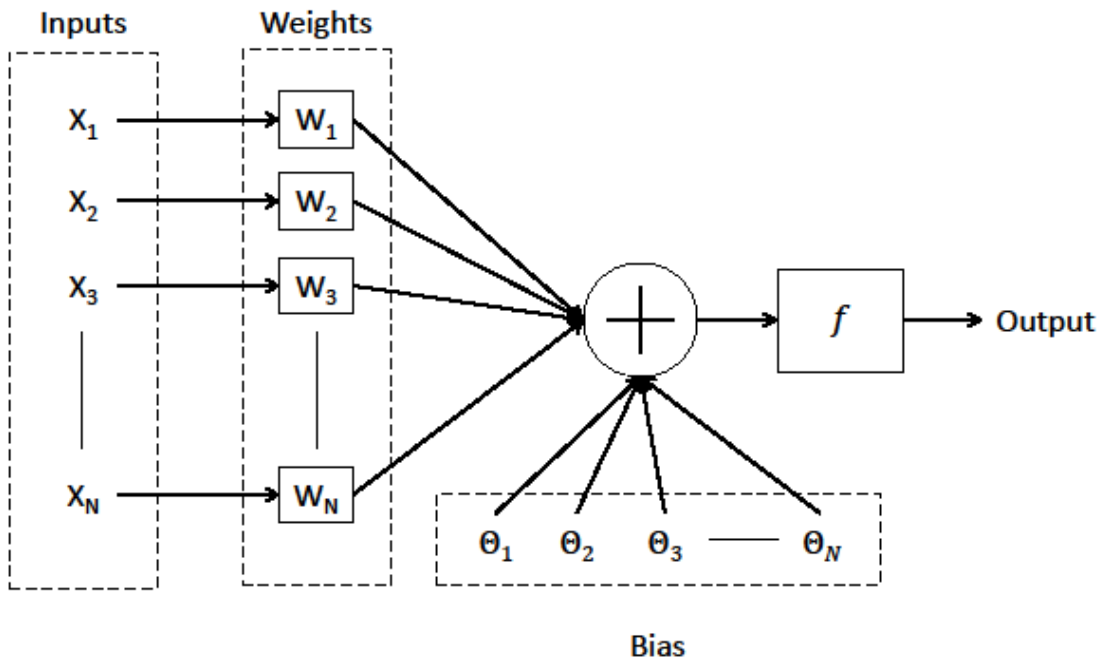


Figure 2.1 A single neuron with N inputs. Where, X_i , W_i , and Θ_i represent the input value, weight and bias for the i th input. The activation function is represented by f and can be either linear or non-linear. Each input is multiplied by its respective weight and then added to its bias, which is summed over all inputs. The activation is applied to the sum over all inputs giving the output of the neuron. Each neuron is associated with one output.

A multiple layer network is realized by allowing the outputs of the

intermediate layer to serve as the input to the following adjacent layer. A multi-layer network with a sigmoid activation function in the first layer and linear activation function in the second layer can be trained to approximate any well behaved function (*Hornik 1991*). A more in depth and mathematically rigorous treatment of the various types of artificial neural networks can be found in *Dreyfus (2004)*.

The use of artificial neural networks in atmospheric sciences is not new. They have been applied to retrievals of physical parameters from satellite observations at regional and global scales, numerical weather prediction, and climate models. *Krasnopolsky (2007)* reviews various applications of artificial neural networks to atmospheric and oceanic sciences along with an excellent introduction to the general theory of neural networks. Application of artificial neural networks to atmospheric longwave radiative transfer calculations has been developed by both *Chevallier et al. (1998, 2000)* and *Krasnopolsky et al. (2005)*.

Chevallier et al. (1998) developed an artificial neural network based longwave radiation parameterization (NeuroFlux) by splitting the contribution to longwave flux from clear sky and from clouds. Separate artificial neural networks are used to calculate the clear sky contribution and for each cloud layer present. Data used to train NeuroFlux were produced using both a band and a line-by-line radiative transfer models. NeuroFlux is currently operational in the European Centre for Medium-Range Weather Forecasts (ECMWF) 4-dimensional variational data assimilation (4D-VAR) system and has been in use since 2003.

Krasnopolsky et al. (2005) developed an artificial neural network trained

with data produced by the National Center for Atmospheric Research Community Atmospheric Model (NCAR CAM) LW radiation parameterizations (*Collins* 2001). It is a single artificial neural network that calculates LW fluxes and heating rates from various profiles of absorbing gases, temperature, cloudiness, and the surface upward LW flux.

The DSLW/UMD v2 model is implemented with two separate artificial neural network models. The first one, following the nomenclature of *Kransopolsky et al.* (2005), is an artificial neural network emulation of the Rapid Radiative Transfer Model (RRTM) and is used to calculate the clear sky contribution to DSLW. The second artificial neural network is an empirical artificial one and is used to calculate the cloud base temperature. This network is termed empirical because it is trained with, satellite observations and is meant to represent an actual physical process and not a model.

2.3. Clear Sky Contribution

2.3.1. DSLW/UMD v1

The clear-sky parameterization of DSLW/UMD v1 is predicated on the Stefan-Boltzman law with a modified emissivity, or an effective atmospheric emissivity model, given as:

$$F_{LW}^{\downarrow} = \varepsilon_{\alpha} \sigma T_o^4 \quad (2.2)$$

T_o temperature at screen level (2-meters above surface), K

ε_a effective atmospheric emissivity.

The choice of screen-level values (2-meters above the surface) of temperature in Eq. (2.2) has been suggested by *Brutsaert (1975)*, *Swinbank (1963)*, *Prata (1996)*, and many others. DSLW depends strongly on water vapor; therefore, it is included in most parameterizations of the effective atmospheric emissivity. Yet, parameterizations based on screen level values have limitations in regions of cold and dry conditions especially where inversions are present. Based on previous work, total column water vapor was chosen to parameterize the effective atmospheric emissivity. The development of effective emissivity parameterization comes from either purely empirically derived relationship (*Swinbank 1963*) or a statistical regression against limited number of ground observations and loosely based on radiative transfer theory (*Prata 1996*). Previous clear sky parameterizations have been site dependent. For instance, the formula for clear sky DSLW developed by *Idso (1981)* is based on three points: Arizona (USA), Indian Ocean, and Alaska (USA). The formulation developed by *Brutsaert (1975)* is based on a standard atmosphere with a constant lapse rate of -6.5 K km^{-1} and limited clear sky emissivity measurements. The DSLW/UMD v1 clear sky parameterization is based on a non-linear regression of the RRTM runs over the entire globe for all seasons, using the ERA-Interim N128 Gaussian grid data. Daily averaged values from ERA-Interim for 2007 over the entire N128 Gaussian grid are used to drive the RRTM allowing the development of a parameterization based on over 42 million observations.

The RRTM utilizes a correlated-k distribution obtained from a line-by-line radiative transfer code to calculate fluxes. These fluxes are calculated in sixteen contiguous bands of the longwave spectrum $10\text{-}3250\text{ cm}^{-1}$ and agree with line-by-line calculations to within 1.5 W m^{-2} (Mlawer *et al.* 1997).

The absorbing species of H_2O , CO_2 , O_3 , CH_4 , and N_2O are accounted for in the RRTM when calculating the DSLW. Values of H_2O and O_3 are taken from the ERA-Interim data as provided on a N128 Gaussian grid. The atmospheric temperature profile, necessary for calculating DSLW is also taken from ERA-Interim. The values of CO_2 are derived from AIRS level-3 CO_2 data (AIRX3C2D; <http://disc.sci.gsfc.nasa.gov/AIRS/data-holdings/by-data-product/AIRX3C2D>). The concentration of CO_2 is assumed well mixed in the vertical and the entire atmospheric column is given the value specified by AIRS. Missing values are filled from globally averaged surface monthly mean data from the Global Monitoring Division of NOAA/Earth System Research Laboratory (NOAA/ESRL) (Pieter Tans, NOAA/ESRL (www.esrl.noaa.gov/gmd/ccgg/trends/)). CH_4 values are monthly averages, stratified by latitude, derived from the GLOBALVIEW- CH_4 data set provided by the National Oceanic and Atmospheric Administration Earth System Research Laboratory (NOAA/ESRL) (GLOBALVIEW- CH_4 , 2009). N_2O values are also monthly averages supplied by NOAA/ESRL halocarbons program and are separated into northern and southern hemispherical averages. The work of Clough *et al.* (1995) showed that the contribution to DSLW from additional absorbing gases (e. g. CCl_4 , CFC-11, CFC-12) is negligible.

Aerosols were not considered in this study since they emanate from local sources and remain in the troposphere for only a few days (*Coakley et al. 1983*) resulting in high spatial and temporal variability. In addition, the overall impact of aerosols on DSLW was estimated to be $< 2 \text{ W m}^{-2}$ (*Morcrette 2002*), which is small compared to the overall uncertainty of 22 to 31 W m^{-2} for current day models when compared to the Baseline Surface Radiation Network (BSRN) ground stations (*Nussbaumer and Pinker 2011*).

Figure 2.2 is a density plot of the effective clear sky emissivity versus the total column water vapor. From Eq. (2.2) the effective emissivity can be calculated as:

$$\varepsilon_{\alpha} = \frac{F_{LW}^{\downarrow}}{\sigma T_o^4} \quad (2.3)$$

F_{LW}^{\downarrow} DSLW calculated from RRTM (W m^{-2})

T_o screen level temperature (K).

The solid line in Figure 2.2 represents the cubic rational that was fit to the data.

The expression for this fit is given as:

$$\varepsilon_{\alpha} = \frac{1.04 X^3 + 1.629 X^2 - 0.3143 X + 0.03349}{X^3 + 2.806 X^2 - 0.5639 X + 0.05783} \quad (2.4)$$

X total column water vapor, g cm^{-2} .

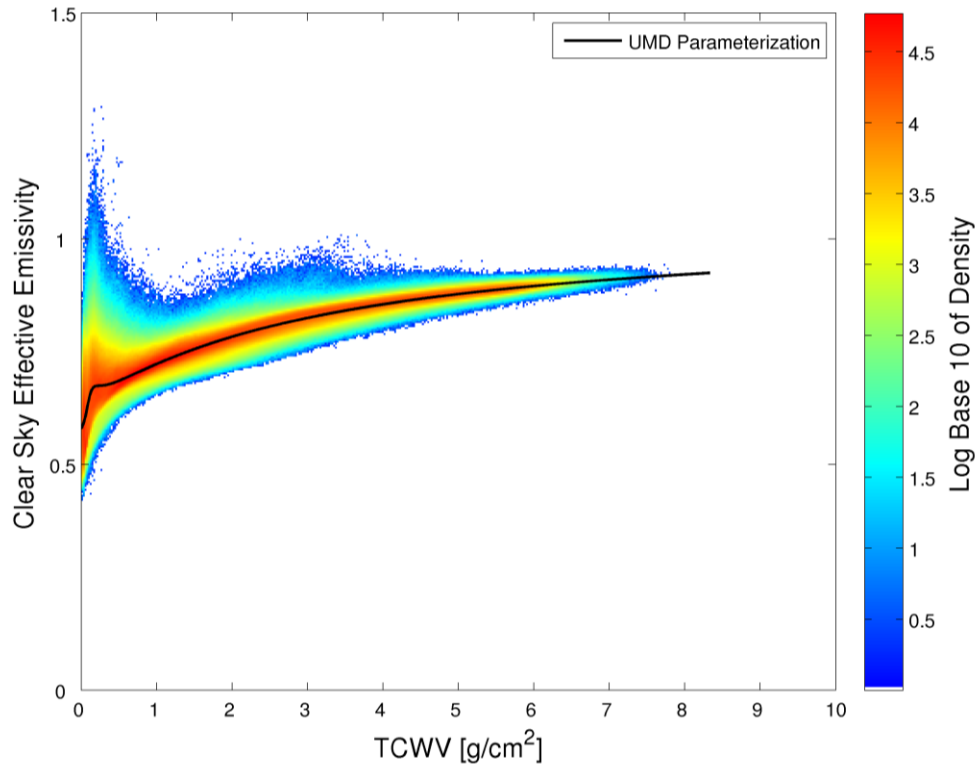


Figure 2.2 A density plot of the effective clear sky emissivity versus the total column water vapor. The clear sky effective emissivity is given as the ratio of the DSLW calculated by RRTM over DSLW calculated by the Stefan-Boltzmann law using the screen level temperature. The x-axis is the total column water vapor from ERA-Interim re-analysis data. The black line is the 3rd order rational fit of the DSLW/UMD v1 parameterization for effective emissivity. The color scale is given as \log_{10} of the density. All values are based on daily data from 2007.

As evident from Figure 2.2, parameterizations that use screen level values of temperature have difficulties in dry regions especially during inversions.

2.3.2. DSLW/UMD v2

In DSLW/UMD v2, calculation of the clear sky contribution to DSLW is improved by accounting for the change in atmospheric temperature with height. In DSLW/UMD v1, a single measurement of screen level temperature is used to describe the temperature of the entire atmospheric column. This is computationally efficient because of the two dimensional nature of the input data; only horizontal changes in temperature and total column water vapor are considered. Ignoring the vertical distribution of temperature can lead to errors in the calculation of the clear sky contribution to DSLW. This is true especially in cold and dry climates where temperature inversions exist and a stronger contribution to DSLW from atmospheric layers above the surface occurs as seen in Figure 2.3.

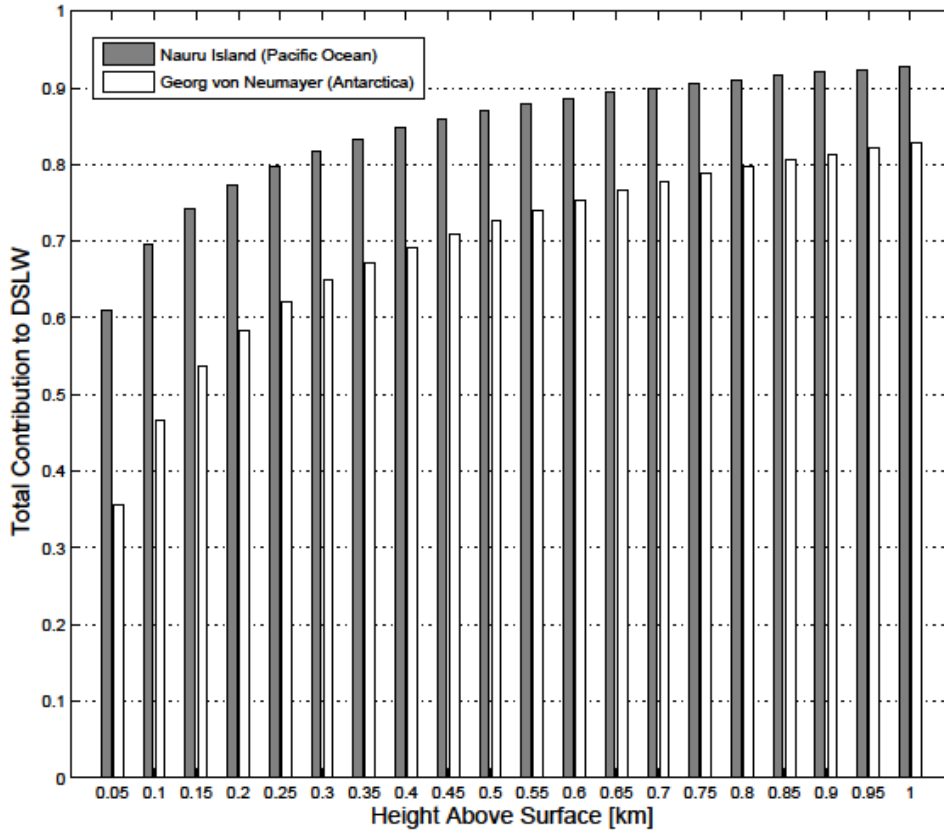


Figure 2.3 The bars represent the contribution to total DSLW from each layer of the atmosphere from the surface to a specified height above the surface for two ground stations calculated using Radiosonde data and RRTM. Radiosonde data are taken from the island nation of Nauru in the South Pacific (0.521° N; 166.9° E) representing a warm humid climate, and the German Polar Research Station, Georg von Neumayer (70.65° N; 8.25° E) in Antarctica representing a cold dry climate with a slight temperature inversion.

Figure 2.3 shows the contribution to total DSLW from each layer of the atmosphere from the surface to a specified height above the surface as calculated using RRTM and Radiosonde data taken from two separate BSRN stations. The island nation of Nauru in the South Pacific (0.521° N; 166.9° E) represents a warm humid climate. The second station is located at the German Polar Research

Station, Georg von Neumayer (70.65° N; 8.25° E) in Antarctica and represents a cold dry climate with a slight temperature inversion. Over 80% of the total DSLW is accounted for in the first 250 meters of atmosphere for Nauru Island, whereas for the station in Antarctica, 80% of the total DSLW is reached at about 850 meters above the surface.

The clear sky model of DSLW/UMD v2 takes into consideration the vertical structure of temperature using a two layer feed forward artificial neural network emulation. The first layer or the hidden layer is composed of 40 neurons utilizing a sigmoid activation function. The second or output layer is a linear activation function. The Levenberg-Marquardt back-propagation algorithm is utilized to train the network. In general, training of a neural network is accomplished by an optimization of the least squares cost function or least square error given by (for one output):

$$E(\mathbf{w}) = \frac{1}{2} \sum_{j=1}^N [t_j(\mathbf{x}_j) - g_j(\mathbf{x}_j, \mathbf{w})]^2 \quad (2.5)$$

Where t is the target value given by the training data for an input array \mathbf{x}

g is the output of the model for an array of inputs \mathbf{x} and weights \mathbf{w}

N is the number of data samples within the training set.

Basically, one trains the network to reduce the difference between the observational or training data and the model output. This is accomplished through adjustment of the weights of the network. The weights are adjusted according to the negative gradient (or second order gradient) of the cost function. However, because we do not know the direct relationship between the weights of the hidden

layers and the cost function, one has to rely on a method such as back-propagation to adjust these weights. In back-propagation the gradient of the cost function for a hidden neuron can be inferred by realizing that the cost function depends on the activation potential of the hidden neuron through the potentials that are downstream and connected to the hidden neuron. For a mathematical treatment of back-propagation the reader is referred to *Rumelhart et al.* (1986). The Levenberg-Marquardt algorithm is based on minimizing the cost function using second order gradients. A concise mathematical description of the Levenberg-Marquardt algorithm can be found in *Marquardt* (1963) for the description of the algorithm and in *Hagen and Menhaj* (1994) for application to training neural networks.

The inputs to the clear sky neural network model are: screen level temperature (temperature 2 m above surface), the temperature at 15 pressure levels above the surface (as described by ERA-Interim), total column water vapor, latitude bands (20° for each band), and month (Table 2.1). These data are from the Research Data Archive (RDA) which is maintained by the Computational and Information Systems Laboratory (CISL) at the National Center for Atmospheric Research (NCAR). The original data are available from the RDA [<http://dss.ucar.edu>] in dataset number ds627.0. The inputs of latitude band and month are used to capture the temporal and spatial variations of clear sky DSLW due to absorbing gases other than water vapor. These gases, however, are not directly included as inputs in the artificial neural network because the feed-forward multi-layer network performance significantly deteriorates when input

values are outside the bounds of the training vector. The strength of artificial neural networks to estimate values lies in interpolation and not extrapolation. Since other major absorbing species vary more slowly than water vapor and temperature, a complete set of data with variation of water vapor and temperature would be needed for each variation of the other gases. Including additional information to capture possible bounds on other parameters than water vapor and temperature would make it difficult to train the network with current computer resources. This is justified since water vapor is the most dominant greenhouse gas to clear sky DSLW (Kiehl and Trenberth 1997) and many parameterizations used previously include water vapor and temperature only as input parameters.

Table 2.1 Input and output parameters for the clear sky artificial neural network.

<i>Input Parameters</i>	<i>Units</i>	<i>Input Type</i>
Total Column Water Vapor	Kg m ⁻²	Re-analysis
Screen Level Temperature	K	Re-analysis
Air Temperature (first 15 pressure levels)	K	Re-analysis
Surface Elevation	m	Satellite
Land Sea Mask	0/1	Satellite
<i>Output Parameter</i>	<i>Units</i>	
Clear Sky DSLW	W m ⁻²	

The same type and sources of training data (previously described) which were used for DSLW/UMD v1 are used for DSLW/UMD v2. In addition, aerosols were also not considered for v2.

2.4. Cloud Contribution

Clouds have a critical role in the balance of energy at the Earth's surface; however, they are one of the most difficult to model. The 4th Assessment Report of the Intergovernmental Panel on Climate Change (IPCC-AR4) has identified cloud feedback as the largest source of uncertainty in the climate system. Clouds have a significant contribution to DSLW, especially in the region of 8-12 μm which is an important component of the cloud feedback system. Within this region there is also absorption from atmospheric constituents such as ozone and water vapor. Therefore, the contribution of clouds to DSLW must take into account the atmosphere between the surface and the cloud base. We define the cloud contribution (or cloud forcing) to DSLW as the difference between all sky and clear sky:

$$F_{cld}^{\downarrow} = F_{all_sky}^{\downarrow} - F_{clr}^{\downarrow} \quad (2.6)$$

Where F_{cld}^{\downarrow} is the cloud contribution (or cloud forcing) to DSLW (W m^{-2})

$F_{all_sky}^{\downarrow}$ is the all sky value of DSLW (W m^{-2})

and F_{clr}^{\downarrow} is the clear sky component of DSLW (W m^{-2})

Following the work by *Schmetz et al.* (1986), for both versions of DSLW/UMD we parameterize the contribution of clouds to DSLW using the Stefan-Boltzman law with a modified emissivity and the screen level temperature:

$$F_{cld}^{\downarrow} = \varepsilon^* T_o^4 \quad (2.7)$$

where T_o is the screen level temperature (K)

and ε^* is the effective emittance related to the cloud contribution and is given as:

$$\varepsilon^* = (1 - \varepsilon_o) \varepsilon_{cld} C \exp \left[\frac{-(T_o - T_B)}{\alpha} \right] \quad (2.8)$$

where ε_o is the clear sky effective emittance, ε_{cld} is the cloud emittance, C is the cloud fraction, T_B is the temperature of the cloud base, and α is a fitting coefficient.

The exponential function was suggested by *Martin and Berdahl* (1984) using model runs of an opaque cloud deck at various altitudes. Calculating the cloud contribution to the effective atmospheric emissivity is more complex than the clear sky contribution and requires multiple inputs.

2.4.1. DSLW/UMD v1

The cloud fraction, cloud emissivity, and screen-level temperature used in the parameterization of cloud contribution are taken from MODIS and ERA-Interim data. The cloud base temperature is the most difficult variable to determine. One must use cloud top pressure and optical depth, land sea mask, and a cloud vertical structure model. DSLW/UMD v1 and other satellite based

models utilize the cloud vertical structure model, which is based on a statistical approach of global cloud layer thickness, developed from 20 years of global rawinsonde humidity profiles (*Wang et al.* 2000). They used relative humidity thresholds of 85% identify cloud layers, while the maximum relative humidity within the cloud was set to be at least 87%. Cloud layer tops and bases were identified from relative humidity jumps greater than 3%. The relative humidity threshold is based on comparison with rawinsonde humidity profiles and aircraft observations of cloud top and base heights (*Poore et al.* 1995) and surface estimates of cloud base heights (*Wang and Rossow* 1995). The cloud layer thickness is determined in the DSLW/UMD v1 model by fitting the vertical structure climatology model from *Wang et al.* (2000) to cloud top height, interpolated from cloud top pressure as well as latitude and month for land and ocean. The cloud top height is interpolated from satellite derived cloud top pressure and geopotential height along constant pressure surface from ERA-Interim. After a cloud layer thickness is computed it is added to the cloud top height to derive a cloud base height. The cloud base height is then interpolated using the ERA-Interim atmospheric temperature profile to find a cloud base temperature. The algorithm for determining cloud base temperature from the statistical model of *Wang et al.* (2000) is shown in Figure 2.4.

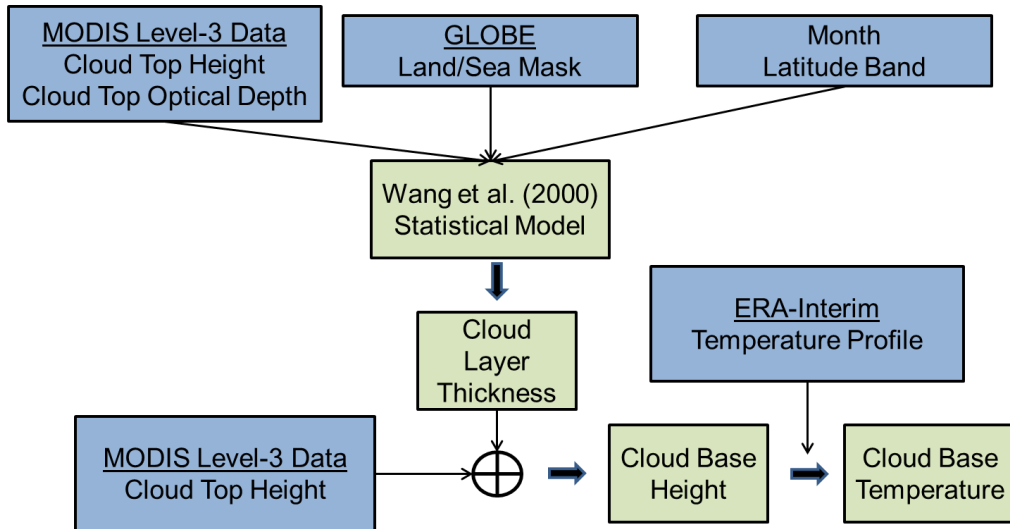


Figure 2.4 Algorithm to calculate cloud base temperature from *Wang et al.* (2000) statistical model.

2.4.2. DSLW/UMD v2

A novel approach for determining cloud base height has been developed using artificial neural networks which shows significant improvement over the earlier statistical model. Since DSLW/UMD v2 (MODIS) employs the same parameterization to calculate the cloud contribution as v1 the full cloud vertical profile such as optical depth or particle effective radius is not necessary; however, the parameterization requires the temperature of the cloud base, namely, the cloud vertical height. Version DSLW/UMD v1 relied on a statistical model developed by *Wang et al.* (2000) to determine the cloud vertical height. We replace this with an artificial neural network based on the co-location of satellite MODIS, CloudSat, and re-analysis ERA-Interim data.

The new artificial neural network used to determine cloud base

temperature from passive satellite observations is of the same type as the clear sky network and is trained using the same algorithm as previously discussed. The inputs to the artificial neural network include the cloud top height, cloud top temperature, cloud top emissivity, and the atmospheric temperature profile. The output of the model is the temperature of the cloud base. The inputs were chosen based on the inputs of the cloud layer thickness statistical model of *Wang et al.* (2000) and trial and error (Table 2.2).

Table 2.2 Input and output parameters for the cloud base temperature artificial neural network.

<i>Input Parameters</i>	<i>Units</i>	<i>Input Type</i>
Cloud Top Height	km	Satellite
Cloud Top Temperature	K	Satellite/Re-analysis
Cloud Emissivity	0-1	Satellite
Screen Level Temperature	K	Re-analysis
Air Temperature (first 15 pressure levels)	K	Re-analysis
<i>Output Parameter</i>	<i>Units</i>	
Temperature Cloud Base	K	

The input and target data used to train the network are key elements in merging passive and active satellite observations. An algorithm was developed to co-locate 5-km MODIS level-2 observations from Aqua with CloudSat's CPR and CALIPSO's CALIOP and daily averaged ERA-Interim data. MODIS level 2

cloud product data were used in conjunction with CloudSat's 1 km 2B-GEOPROF-LIDAR data set. The MODIS data were acquired as part of the activities of NASA's Science Mission Directorate, and are archived and distributed by the Goddard Earth Science (GES) Data and Information Services Center (DISC). CloudSat flies in close formation to Aqua as part of NASA's A-train. Nominally, CloudSat lags Aqua by 43 seconds +/- 15 seconds, therefore in order to co-locate observations between these two satellites, for each MODIS observation the 2B-GEOPROF-LIDAR data set was first temporally filtered according to which observation falls within 60 seconds of the MODIS observation. The 2B-GEOPROF-LIDAR data set was then spatially filtered according to which observations fall within a 2.5 km radius of the MODIS observation. If more than one CloudSat observation was found, the observation closest to MODIS centered coordinates was selected. If no 2B-GEOPROF-LIDAR observations were found within a 2.5 km radius of the 5-km MODIS observation, then the MODIS observation was discarded. It is then determined which ERA-Interim grid box (Gaussian N128 grid) that the observations fall within in order to corresponding meteorological parameters. The 5-km MODIS data provides the cloud top pressure and emissivity. The cloud top pressure was used to interpolate cloud top height and temperature from daily average ERA-Interim geopotential height, pressure, and temperature profiles. The cloud top height, temperature, and emissivity derived from MODIS observation and ERA-Interim data along with total column water vapor and atmospheric temperature profile from ERA-Interim composed the inputs for the training data set. The 2B-

GEOPROF-LIDAR data set provides a geometric description of the clouds vertical structure. The height of the base of the lowest cloud layer from the 2B-GEOPROF-LIDAR data set was used to interpolate cloud base temperature from geopotential height and temperature profiles from ERA-Interim. This served as the target for the training set. A random subset of all the co-located observations for the year 2007 was used to train the neural network.

Chapter 3: Validation and Comparison

3.1. Abstract

While both models can provide information on clear and cloudy sky contributions to DSLW, the evaluation is accomplished differently for each component to be described in what follows. The clear sky component of each model is evaluated against a radiative transfer model. This is common practice because of the lack of separation between clear sky and cloudy sky alone ground observations. Therefore, all sky estimates are used in evaluation against ground observations.

3.2. Clear Sky Component

3.2.1. DSLW/UMD v1

Clear sky DSLW radiation as calculated by the DSLW/UMD v1 parameterization is compared against the clear sky component of DSLW calculated from the RRTM using the inputs described in the model description section. The DSLW/UMD v1 parameterization is driven with daily averaged values of screen level temperature and total column water vapor from ERA-Interim for 2007 at global scale (Figure 3.1). The results are plotted as a \log_{10} of density because of the large number of data points (over 42 million). The agreement between the parameterization and the radiative transfer model

computations has a correlation coefficient of 0.998, a RMSE of 6.72 W m^{-2} , and a bias of -0.05 W m^{-2} . The p-value of the correlation is 0.0000, where the p-value is the probability of getting a correlation as large as the observed value by random chance, when the true correlation is zero. With correlation coefficient of 0.998 and a sample size of ~42 million this should come as no surprise.

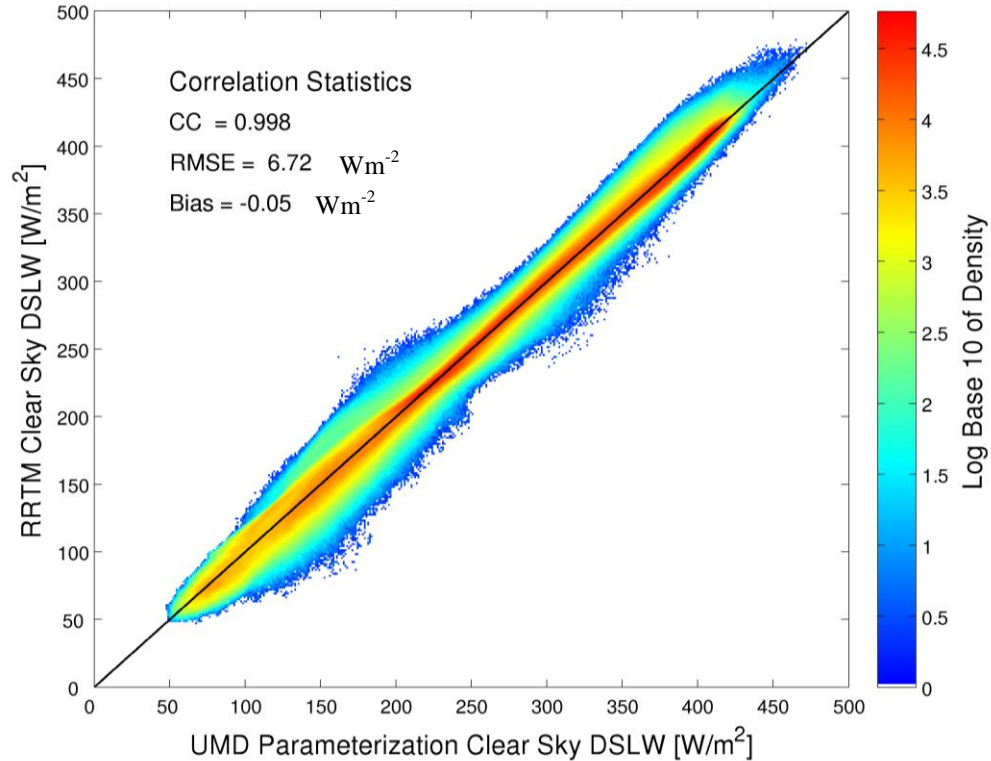


Figure 3.1 A plot comparing the clear sky contribution to DSLW as calculated by RRTM versus the UMD parameterization. The color scale is given as \log_{10} of the density. All values are based on daily data from 2007.

3.2.2. DSLW/UMD v2

The clear sky portion of DSLW/UMD v2 is also evaluated against the RRTM radiative transfer model. There is excellent agreement between the clear sky artificial neural network and the RRTM calculations with a correlation of 1.00 a RMSE of 2.31 W m^{-2} and a bias of 0.00 W m^{-2} for 2007, demonstrating the ability of the neural network to emulate a full radiative transfer model while having the advantage of computational efficiency. The p-value of the correlation is 0.0000, indicating that the correlation is significant. The clear sky artificial neural network is an improvement over the previous DSLW/UMD v1 clear sky parameterization (*Nussbaumer and Pinker 2011*) which was based on total column water vapor and screen level temperature. Because of the large number of data points used in the comparison ~42 million, Figure 3.2 shows the \log_{10} density of the data points. The artificial neural network model is also compared to the clear sky calculations of RRTM for 2005, 2006, and 2008. The agreement between the neural network and RRTM for these years is slightly less than for 2007, which is attributed to the fact that the clear sky artificial neural network does not directly incorporate absorbing species other than water vapor and the network has been trained for levels of these species for 2007. The maximum drift in bias from 2007 is $< 0.4 \text{ W m}^{-2}$ while the change in RMSE is $< 0.15 \text{ W m}^{-2}$ (Table 3.1).

Table 3.1 Statistical comparison between the clear sky contribution to DSLW from DSLW/UMD v2 (MODIS) artificial neural network and the Rapid Radiative Transfer Model (RRTM).

Year	Correlation Coefficient	Bias (W m⁻²)	RMSE (W m⁻²)
<i>2005</i>	1.00	0.04	2.42
<i>2006</i>	1.00	-0.05	2.44
<i>2007</i>	1.00	0.00	2.31
<i>2008</i>	1.00	0.39	2.43

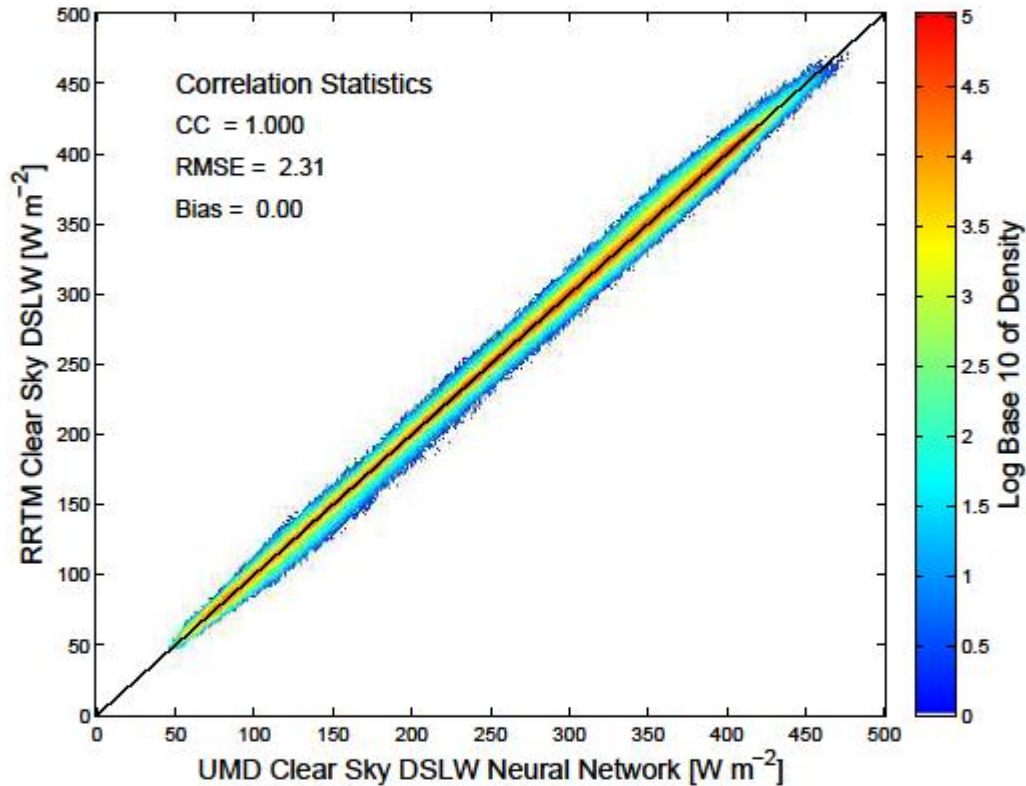


Figure 3.2 Comparison of the DSLW/UMD v2 (MODIS) artificial neural network model (x-axis) and the RRTM (y-axis) for calculation of the clear sky contribution to DSLW for daily averages of 2007. Because of the large number of data points used in the comparison and high overlap colors are used to indicate the \log_{10} density of observations.

3.3. Evaluation of the Cloud Base Temperature Model

DSLW/UMD v1 as well as the other satellite based models used in the evaluation (ISCCP-FD and GEWEX-SRB) utilize the statistical model by Wang et al. (2000) to determine the cloud vertical structure used in calculating the cloud contribution to DSLW. Previous analysis shows differences between models and ground truth are largest in the Polar Regions, where, because of the cold air and

dry climate, clouds have the largest influence on DSLW. Therefore, improvement of the cloud vertical structure model should have a significant impact on the model's ability to estimate DSLW especially in the high latitude regions. This improvement is accomplished using an artificial neural network in DSLW/UMD v2 (MODIS) to determine the cloud base temperature. The *Wang et al. (2000)* statistical model and the neural network model are evaluated using active satellite measurement data, the 2B-GEOPROF-LIDAR data set, which is a combination of CPR and CALIOP measurements. The height of the lowest hydrometeor layer from 2B-GEOPROF-LIDAR is interpolated to find the temperature of the cloud base using the temperature and geopotential profile from ERA-Interim re-analysis. The top panel in Figure 3.3 shows the comparison of cloud base temperature calculated from the DSLW/UMD v2 (MODIS) artificial neural network versus observed from satellite data for 2008. There is an overall good agreement between the model and the observations with a correlation coefficient of 0.92, RMSE of 4.89 K and bias of -0.09 K. The p-value for both correlations is 0.0000, indicating that the correlation is significant. The bottom part of Figure 3.3 shows the comparison of the cloud base temperature calculated using the cloud vertical thickness model by *Wang et al. (2000)* versus observed from satellite data for 2008. The cloud thickness from *Wang et al. (2000)* was added to the cloud top height as given by satellite observations to determine the cloud base height. This was then interpolated using ERA-Interim temperature profile to produce the cloud base temperature. Comparison of the *Wang et al. (2000)* cloud thickness model with satellite observations for 2008 gives a correlation coefficient of 0.16, an

RMSE of 19.67 K, and a bias of -2.52 K. The artificial neural network to calculate cloud base temperature significantly outperforms the statistical model by *Wang et al.* (2000) in all metrics used for comparison.

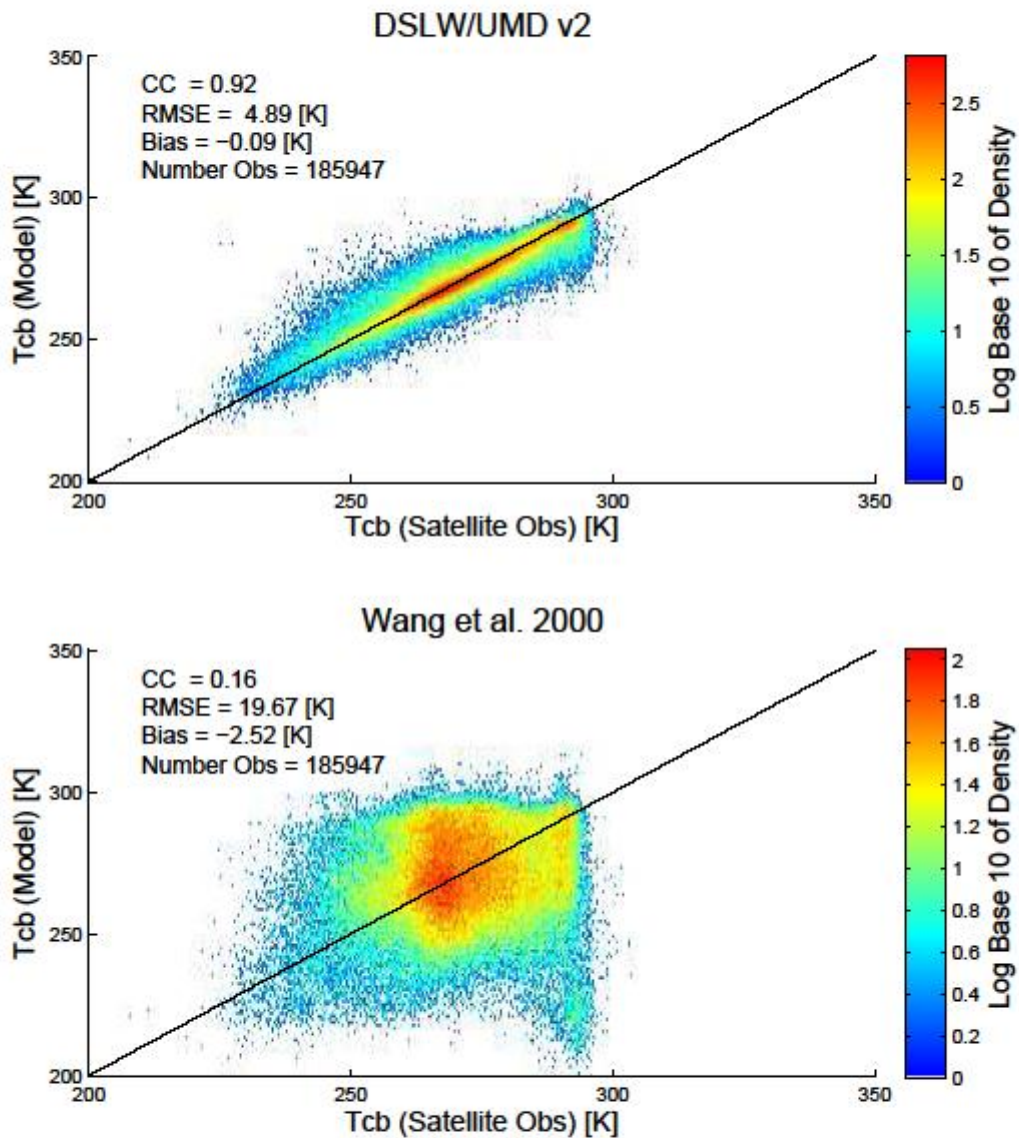


Figure 3.3 Comparison of cloud base temperature observed by CPR and CALIOP in 2008 vs temperature calculated from DSLW/UMD v2 artificial neural network (top) and the cloud thickness model from *Wang et al.* 2000 (bottom).

3.4. All Sky Component

The all sky component of DSLW as estimated by both models is evaluated against a worldwide network of ground measurements from the World Radiation Monitoring Center – Baseline Surface Radiation Network (WRMC-BSRN) and by comparison with independent satellite based inference schemes and numerical models that are based on radiative transfer computations. Figure 3.4 provides a graphical representation of the locations of the BSRN ground stations. The BSRN network has stations in Polar, Mid-Latitude, and Tropical regions; the stations are mostly located in North America and Western Europe, namely, in Mid-Latitudes. Five stations in Brazil that at the time of this study had unresolved quality control issues were not used.

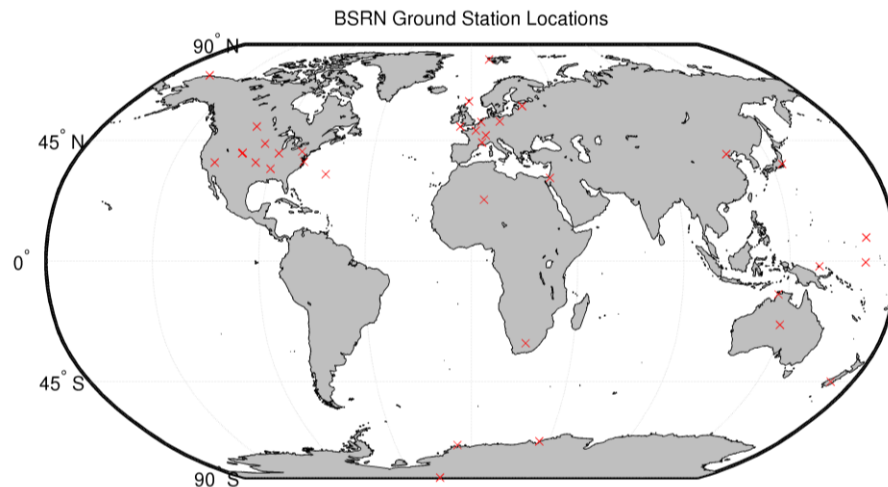


Figure 3.4 A global map showing the locations of the BSRN ground stations used in the analysis.

The independent models used for comparison were chosen to represent various categories. The ECMWF (<http://www.ecmwf.int/>) ERA-Interim Re-analysis model assimilates a variety of sources of meteorological parameters but clouds are produced internally. Calculations for both the radiation and cloud physics modules are done at a 3-hourly time scale. The ERA-Interim DSLW data used in the comparison are at a 1.5° resolution. Similar to ERA-Interim, the National Center for Environmental Predictions (NCEP) and the Department of Energy (DOE) Re-analysis II from the National Oceanic and Atmospheric Administration (NOAA), NCEP-DOE Re-analysis II, assimilates a variety of sources of meteorological parameters, and produces clouds internally. The temporal resolution for the radiation and cloud physics modules is at an hourly time scale. The spatial resolution of the NCEP-DOE II data is at the T62 Gaussian Grid ($\sim 1.8^\circ$). Both ERA-Interim and NCEP-DOE Re-analysis II use the Rapid Radiative Transfer Model (RRTM) developed by the Atmospheric and Environmental Research (AER) group. The International Satellite Cloud Climatology Project, ISCCP-FD model (*Zhang et al.* 2004) utilizes satellite observations from ISCCP cloud products (D1) gridded at a 280 km equal area grid and then transformed to a 2.5° equal angle grid. The ISCCP-FD model uses the Goddard Institute of Space Studies (GISS), Global Circulation Model (GCM) radiative transfer code and satellite data from the Television InfraRed Observational Satellite (TIROS) Operational Vertical Sounder as primary source for temperature and humidity profiles. DSLW from ISCCP-FD is derived every three hours and averaged into daily values. The Global Energy and Water Cycle

Experiment (GEWEX) Surface Radiation Budget (SRB) model (*Stackhouse et al.* 2000) utilizes the radiative transfer code developed by *Fu et al.* (1997). The GEWEX-SRB utilizes ISCCP cloud data gridded to 1° resolution. In GEWEX-SRB the DSLW is derived at a 3-hourly temporal resolution and averaged into daily values. Temperature and humidity profiles are taken from Goddard EOS Data Assimilation System, level-4 (GEOS-4) re-analysis data. GEWEX-SRB in addition provides a quality check product for their daily averaged DSLW. This product is based on the parameterization derived by *Gupta et al.* (1992) and was also included in the evaluation. Table 3.2 summarizes the RT based models along with their primary inputs.

Table 3.2 Information on DSLW/UMD v1 and four commonly used radiative transfer based methods for calculating DSLW, including name of radiative transfer model or parameterization, resolution of global DSLW, cloud input source, and primary source for temperature and humidity profiles.

Scheme	RT Model / Parameterization	Resolution	Cloud Input	Temperature & Humidity
DSLW/UMD	Clear sky parameterization based on Rapid Radiative Transfer Model. Cloud contribution Parameterization based on Schmetz <i>et al.</i> (1986) and Martin <i>et al.</i> (1984)	1.0°	MODIS	ERA-Interim re-analysis
			Level 3 Data	
ERA-Interim	Rapid Radiative Transfer Model (RRTM)	1.5°	Cloud physics model	Various satellite and in-situ assimilated observations
NCEP-DOE Re-analysis II	Rapid Radiative Transfer Model (RRTM)	T62 Gaussian Grid (~1.8°)	Cloud physics model	Various satellite and in-situ assimilated observations
ISCCP-FD	Goddard Institute of Space Studies (GISS) Global Circulation Model (GCM)	2.5°	ISCCP-D1	Television Infra-Red Observation Satellites (TIROS) Operational Vertical Sounder
GEWEX SRB	Fu <i>et al.</i> (1997) radiative transfer model	1.0°	ISCCP-DX	Goddard EOS Data Assimilation System, level-4 GEOS-4

Numerical Weather Prediction Model

Satellite Observation Model

3.4.1. DSLW/UMD v1

Daily averages of the all sky component of DSLW/UMD v1 are compared with ground station measurements for each year from 2003 to 2007 independently and also aggregated for all years. Figure 3.5 shows the comparison between model and ground stations; it can be seen that the model is less accurate at lower values of DSLW. This typically occurs in the higher latitudes where temperature inversions commonly exist and clouds have a significant impact. These problems

are addressed in the v2 of the model.

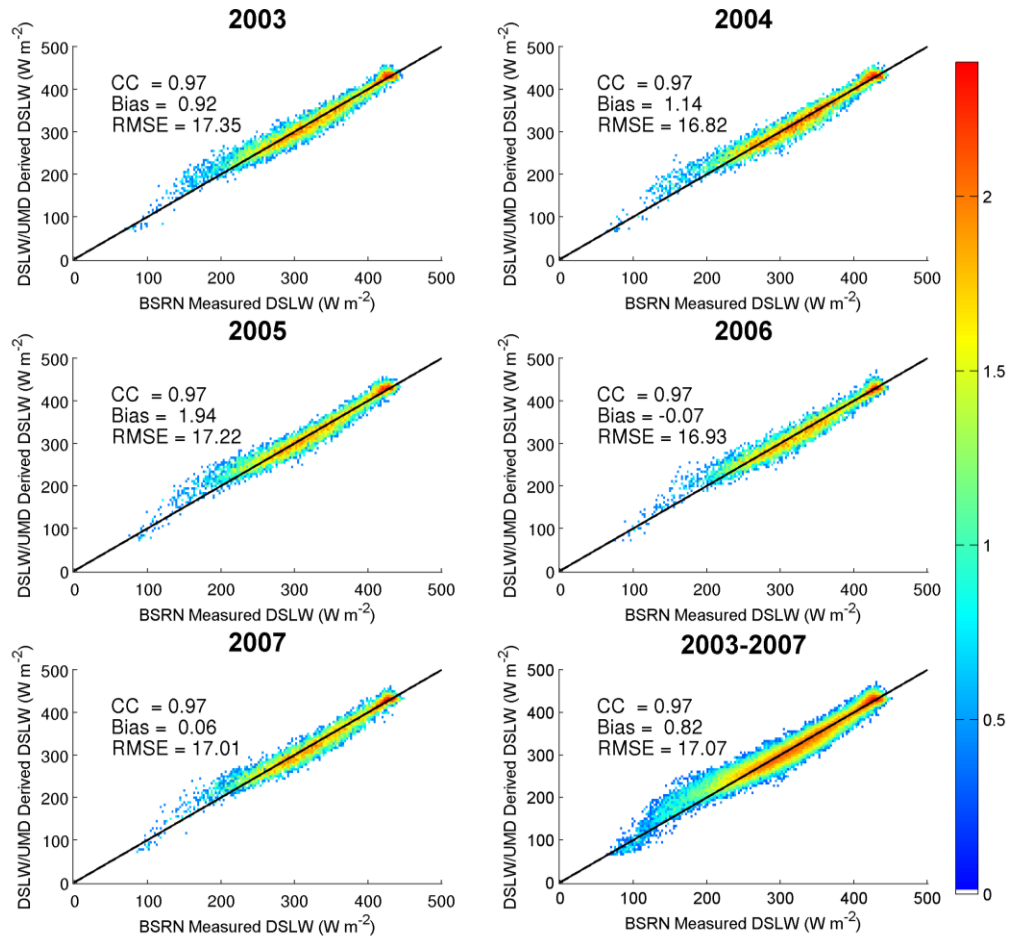


Figure 3.5 A plot of DSLW/UMD v1 derived data versus BSRN ground stations for each year and for aggregated years 2003 to 2007. The black line follows a one-to-one comparison. The color scale is given as \log_{10} of the density. The bias and RMS are given in $W m^{-2}$.

Not only is it useful to know how the model compares against ground truth but it is informative to see performance relative to present day model estimates. Summary statistics for correlation between DSLW/UMD v1, present

day models, and BSRN are shown in Table 3.3. The correlation coefficients for the DSLW/UMD v1 algorithm is 0.97 for all years, while the bias and RMSE range from -0.07 to 1.93 (W m^{-2}) and 16.82 to 17.35 (W m^{-2}), respectively. The p-value for all the model correlations is 0.000, indicating that the correlations are significant. The DSLW/UMD v1 algorithm is consistently among the highest in correlation and lowest in bias and RMSE among the models. The number of data points used for the comparison of DSLW/UMD v1 is slightly less than for the other models. This is due to retrieval failures of cloud top properties in the MODIS product over regions where relative humidity was non-retrievable from the Global Data Assimilation System (GDAS) temperature and moisture profiles (<http://modis-atmos.gsfc.nasa.gov/validation.html>). The MODIS cloud top properties algorithm was modified for data beyond November 2007 to better deal with this issue.

Table 3.3 Statistics for daily average comparison of DSLW predicted by each model compared with BSRN ground station observations for each year. Statistics include correlation coefficient, bias, root mean square error, and number of ground stations included in analysis.

Algorithm	Correlation Coefficient	Bias (W m⁻²)	RMSE (W m⁻²)	# of Stations
<i>2003</i>				
DSLW/UMD v1	0.97	0.92	17.35	33
ISCCP-FD	0.92	8.40	31.99	33
ERA-Interim	0.95	-8.00	26.80	33
NCEP-DOE Re-analysis 2	0.96	-15.26	28.34	33
GEWEX QC v3.0	0.96	1.85	23.47	33
GEWEX SRB v3.0	0.96	-1.29	22.91	33
<i>2004</i>				
DSLW/UMD	0.97	1.14	16.82	32
ISCCP-FD	0.93	8.02	29.92	32
ERA-Interim	0.95	-7.11	26.25	32
NCEP-DOE Re-analysis 2	0.97	-14.45	27.52	32
GEWEX QC v3.0	0.96	1.40	22.48	32
GEWEX SRB v3.0	0.96	-1.77	22.29	32
<i>2005</i>				
DSLW/UMD	0.97	1.93	17.22	33
ISCCP-FD	0.92	8.84	30.84	33
ERA-Interim	0.95	-7.43	26.19	33
NCEP-DOE Re-analysis 2	0.96	-14.91	28.31	33
GEWEX QC v3.0	0.96	1.84	22.87	33
GEWEX SRB v3.0	0.96	-1.02	22.47	33

2006				
DSLW/UMD	0.97	-0.07	16.93	32
ISCCP-FD	0.91	9.33	32.15	32
ERA-Interim	0.95	-8.66	26.02	32
NCEP-DOE Re-analysis 2	0.97	-14.24	26.68	32
GEWEX QC (Gupta) v3.0	0.96	1.88	22.26	32
GEWEX SRB v3.0	0.96	-0.95	21.86	32
2007				
DSLW/UMD	0.97	0.06	17.01	32
ISCCP-FD	0.91	9.34	32.48	32
ERA-Interim	0.95	-9.01	25.87	32
NCEP-DOE Re-analysis 2	0.97	-14.82	27.76	32
GEWEX QC (Gupta) v3.0	0.96	2.01	22.92	32
GEWEX SRB v3.0	0.96	-1.12	22.22	32

Figure 3.6 shows the comparison of daily averaged DSLW from models and ground stations for aggregated years between 2003 and 2007. Both numerical weather prediction models, NCEP/DOE II, and ERA-Interim show large negative biases for these years, meaning that the models under predict the value of DSLW compared to ground truth. For all years aggregated, DSLW/UMD v1 has the closest agreement with ground observations relative to the other models.

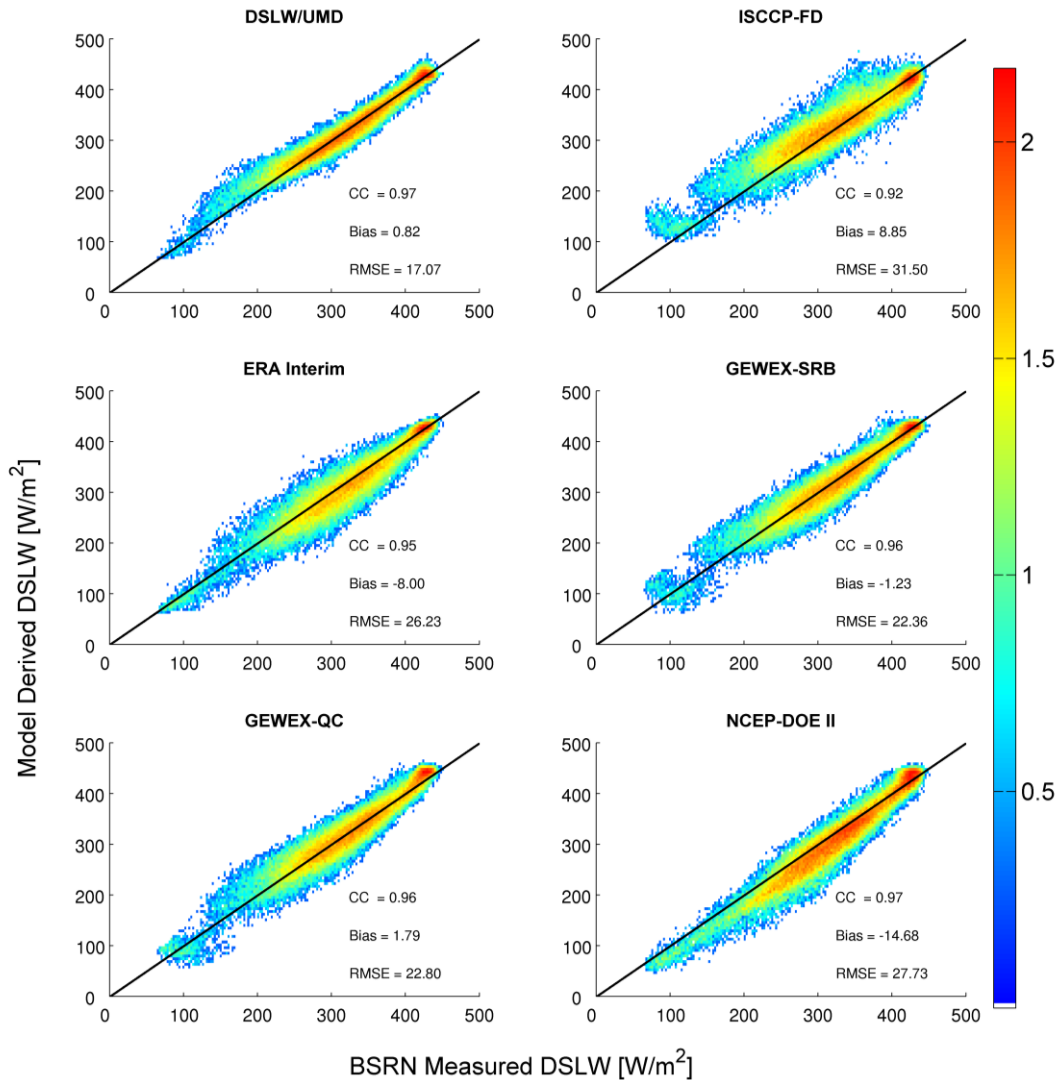


Figure 3.6 A plot of the model derived DSLW (DSLW/UMD, ISCCP-FD, ERA-Interim, GEWEX-SRB, GEWEX-QC, and NCEP-DOE II) versus the BSRN ground station measured values. The black line follows a one-to-one comparison. The color scale is given as \log_{10} of the density. All values are based on daily data from 2003 to 2007. The bias and RMSE are given in W m^{-2} .

Differences in monthly mean results are presented in Figure 3.7. Shown are the monthly mean DSLW/UMD v1 for January 2007; the difference between the DSLW/UMD v1 and ERA-Interim, NCEP DOE II, and ISCCP-FD,

respectively. As seen, both numerical models underestimate DSLW at high altitude regions such as the Tibetan Plateau when compared to the MODIS based DSLW/UMD v1 results. ERA-Interim and DSLW/UMD v1 both utilize the same inputs for temperature and humidity profiles as well as similar methods for calculating clear sky contribution to DSLW. The Tibetan Plateau nominally has low water vapor concentration which reaches a minimum in January (*Gao et al. 2003*); this increases the impact of clouds on DSLW. On the other hand, ISCCP-FD overestimates the LW fluxes in the desert regions of Africa and overestimates them in North America, Greenland, and Antarctica. ISCCP-FD utilizes the TIROS Operational Vertical Sounder (TOVS) for temperature and humidity inputs. TOVS is known to overestimate the total column moisture for dry atmospheres as reported in *Stephens et al. (1994)*. In order to fully understand the difference between the results a thorough investigation of the various approaches needs to be undertaken and is beyond the scope of this paper.

Figure 3.8 shows the zonally and globally averaged DSLW for all the models used for the period 2003 to 2007. Most of the discrepancy between the models exists in Polar and Northern Hemisphere Mid-Latitude regions where the air is less saturated than in the Tropics thus increasing the influence of temperatures and clouds which differ in the models that were evaluated. It also demonstrates that the models accurately capture the fact that the Southern Hemisphere Polar region receives less DSLW than the Northern Hemisphere Polar region.

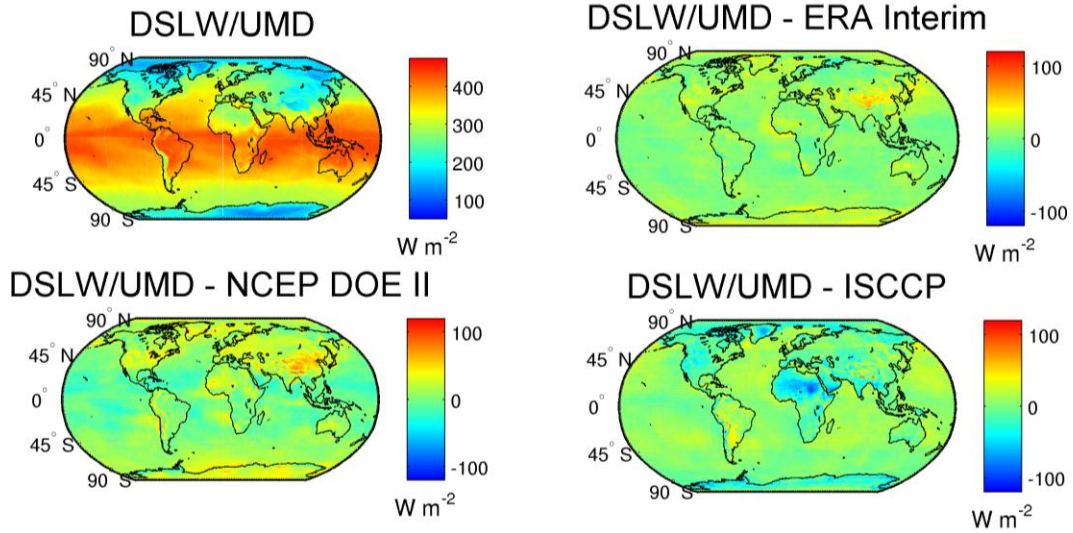


Figure 3.7 A sample plot of monthly averaged DSLW calculated from DSLW/UMD v1 and the difference between DSLW/UMD v1 and ERA-Interim, NCEP DOE II and ISCCP. For the difference plots a negative value indicates that a particular model predicts a higher value of DSLW compared to the DSLW/UMD v1 model.

DSLW Averaged Flux: 2003-2007

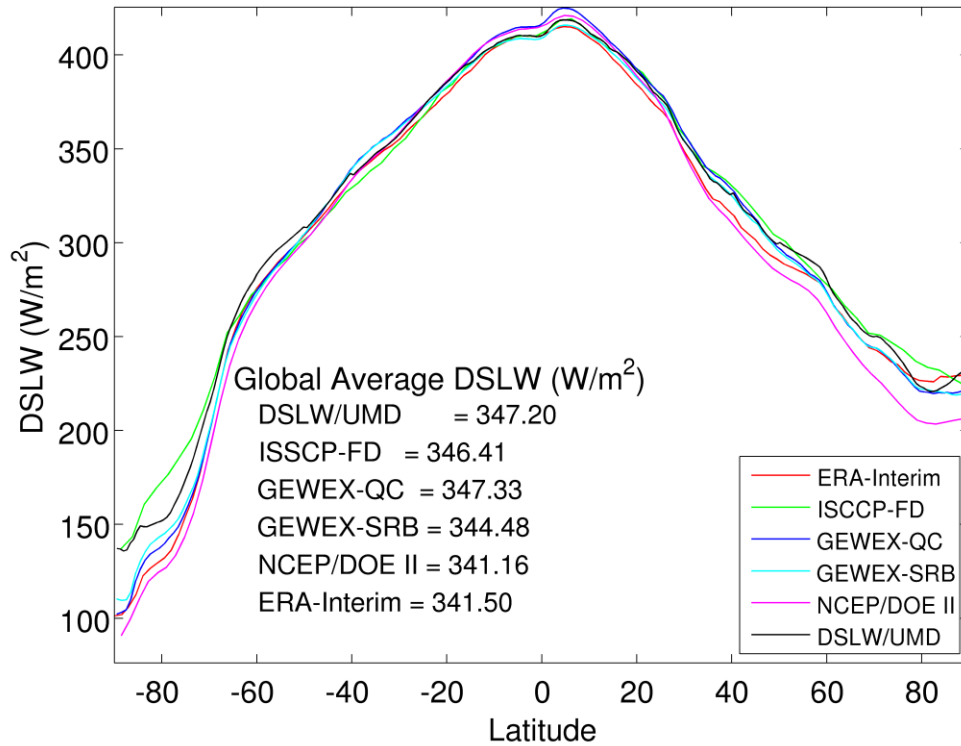


Figure 3.8 Zonally and globally averaged daily DSLW for 2003-2007 for all models used in comparison.

BSRN ground stations are stratified into Tropical, Mid-Latitude, and Polar latitudinal belts. We define the Tropics located between -23.5°N and 23.5°N , the Mid-Latitudes between $\pm 66.5^\circ\text{N}$ and $\pm 23.5^\circ\text{N}$, and the Polar Regions between $\pm 66.5^\circ\text{N}$ and $\pm 90^\circ\text{N}$ latitudes. The majority of models, including the DSLW/UMD v1 predict DSLW with greatest accuracy in the tropical region that has relatively high water vapor and temperature as compared to the other regions. Water vapor has the most influence on DSLW (Niemela et al. 2001). Radiative transfer model runs have shown that the majority of the contribution to DSLW

comes from within the first few hundred meters of the surface (*Zhao et al.* 1994; *Schmetz et al.* 1986). Most parameterizations and radiative transfer based models are well adept at calculating the contribution of DSLW due to water vapor. Therefore, with accurate inputs of water vapor, in areas such as the Tropics the DSLW estimates are in good agreement with observations, as illustrated in Figure 3.9.

The first five plots of Figure 3.9 show histograms of the monthly averaged RMSE (W m^{-2}) for each latitudinal band. The solid line is the mean RMSE of all ground stations for the entire period. The last plot in Figure 3.9 shows monthly averaged total column water vapor (kg m^{-2}) and lines corresponding to the average 2-meter temperature, for each latitudinal band, as derived from ERA-Interim re-analysis data for the period 2003 to 2007.

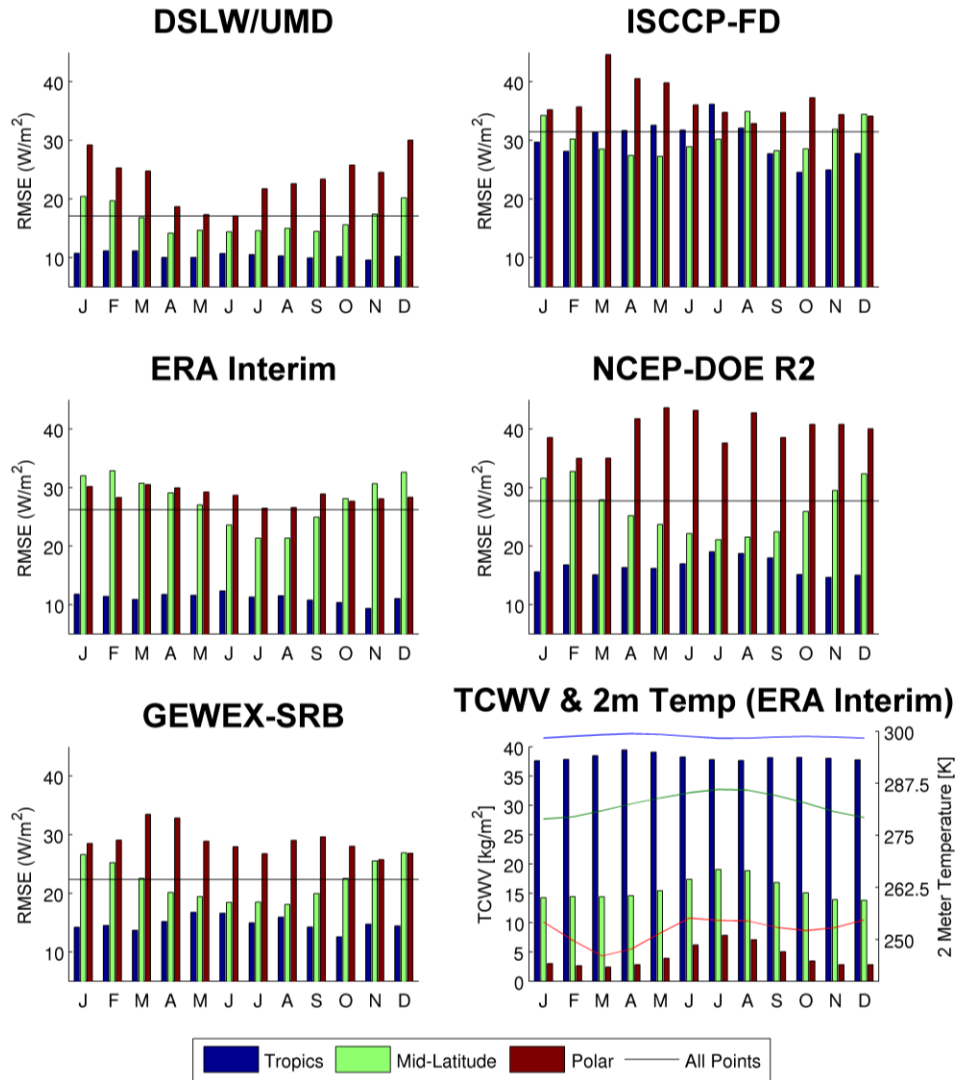


Figure 3.9 In the first five panels, the bars for each model represent the average value of RMSE (W m^{-2}) for each month for the combined years 2003 to 2004. The comparison is broken down into latitudinal regions: Tropical (blue), Mid-Latitude (green), and Polar (red). The black line is the mean RMSE of all ground stations for the entire period. The last graph depicts the averaged total column water vapor (kg m^{-2}) derived from ERA-Interim re-analysis broke down by month and region.

The lines correspond to 2-meter surface temperature from ERA-Interim re-analysis. The blue line represents the Tropical, green the Mid-Latitudes, and the red corresponds to the Polar Regions.

The correlation between water vapor amount and near surface temperature and the ability of models to predict DSLW is further illustrated in the inter-annual variability of total column water vapor and near surface temperature in the Mid-Latitudes and to some extent in the Polar Regions. During June through September there is an increase in the averaged total column water vapor and 2-meter temperature, which corresponds well to an increase in accuracy of DSLW prediction in the Mid-Latitudes and to a lesser extent in the Polar Regions. With dryer, cooler air in the Polar Regions, the effect of clouds, which are the most difficult aspect to model, play a more important role in the contribution to DSLW. Figure 3.9 suggests that there may be a critical point in terms of water vapor and near surface temperature at which the effects of clouds on DSLW becomes almost negligible. The performance of the DSLW/UMD v1 approach in the Mid-Latitudes and Polar Regions is most likely affected by the improved input parameters to the inference scheme.

3.4.2. DSLW/UMD v2

The all sky component of DSLW, which is the sum of the clear sky and cloud component, as estimated with the DSLW/UMD v2 (MODIS) model is evaluated against a worldwide network of ground measurements from the World Radiation Monitoring Center – Baseline Surface Radiation Network (WRMC-BSRN) and by comparison with independent satellite based inference schemes and numerical models that are based on radiative transfer computations. The

BSRN ground stations used in the evaluation are the same used for evaluating DSLW/UMD v1 in chapter 2 (Figure 3.4). The BSRN network has stations in Polar, Mid-Latitude, and Tropical regions; the stations are mostly located in North America and Western Europe, namely, in Mid-Latitudes.

In addition to implementing the DSLW/UMD v2 model with MODIS cloud data, we implement it with the ISCCP DX satellite data (<http://isccp.giss.nasa.gov/>). This is the same type of satellite data used in the ISCCP-FD and GEWEX-SRB models. For DSLW/UMD v2 ISCCP DX, the raw satellite data are gridded to an equal area grid corresponding to the area of a N128 Gaussian grid cell on the equator. The satellite data are then converted to match the N128 Gaussian grid of the independent meteorological parameters used. The calculation of clear sky flux for DSLW/UMD v2 (DX) is identical to that of the MODIS version (i.e., same inputs and results). The cloud contribution to DSLW/UMD v2 (DX) is calculated with the same artificial neural network model as trained with MODIS data. Ideally, the new artificial neural network model would be trained using co-located DX and 2B-GEOPROF-LIDAR data. This will be the subject of future work.

Model results are compared against BSRN ground stations on a daily time scale for each year from 2003 to 2009 and also as aggregated for all years. The resulting statistics as broken down by year are listed in Table 3.4. Figure 3.10 shows scatter density plots of model calculated daily averaged DSLW against BSRN measurements for 2003 to 2007 along with the aggregated statistics. The p-value for all correlations given is 0.000, indicating that the correlations are

significant. The years 2008 and 2009 are not included in the analysis for Figure 3.10 because data for this time period were not available at the time of this study for the GEWEX SRB and DSLW/UMD v2 (DX) models. For daily averages aggregated over 2003 to 2007, from Figure 3.10 it can be seen that DSLW/UMD v2 model applied with MODIS data has the best agreement with ground observations as compared with the other models. In addition, DSLW/UMD v2 implemented with DX data has better agreement with ground truth than the other models (except DSLW/UMD v2 MODIS). The cloud vertical structure neural network model has not been optimized for use with the DX satellite data.

Table 3.4 Statistics for daily average comparison of DSLW predicted by each model compared with BSRN ground station observations for each year. Statistics include correlation coefficient, bias, and root mean square error.

Algorithm	Correlation Coeff	Bias (W m⁻²)	RMSE (W m⁻²)
2003			
DSLW/UMD v2 (MODIS)	0.98	-0.16	16.16
DSLW/UMD v2 (DX)	0.96	-0.69	21.67
ISCCP-FD	0.92	8.40	31.99
ERA-Interim	0.95	-8.00	26.80
NCEP-DOE Re-analysis 2	0.96	-15.26	28.34
GEWEX QC v3.0	0.96	1.85	23.47
GEWEX SRB v3.0	0.96	-1.29	22.91
2004			
DSLW/UMD v2 (MODIS)	0.98	0.29	15.16
DSLW/UMD v2 (DX)	0.96	-0.37	21.25
ISCCP-FD	0.93	8.02	29.92
ERA-Interim	0.95	-7.11	26.25
NCEP-DOE Re-analysis 2	0.97	-14.45	27.52
GEWEX QC v3.0	0.96	1.40	22.48
GEWEX SRB v3.0	0.96	-1.77	22.29

2005			
DSLW/UMD v2 (MODIS)	0.98	0.84	15.74
DSLW/UMD v2 (DX)	0.96	-0.15	20.70
ISCCP-FD	0.92	8.84	30.84
ERA-Interim	0.95	-7.43	26.19
NCEP-DOE Re-analysis 2	0.96	-14.91	28.31
GEWEX QC v3.0	0.96	1.84	22.87
GEWEX SRB v3.0	0.96	-1.02	22.47
2006			
DSLW/UMD v2 (MODIS)	0.98	-1.05	15.96
DSLW/UMD v2 (DX)	0.96	-0.15	20.78
ISCCP-FD	0.91	9.33	32.15
ERA-Interim	0.95	-8.66	26.02
NCEP-DOE Re-analysis 2	0.97	-14.24	26.68
GEWEX QC v3.0	0.96	1.88	22.26
GEWEX SRB v3.0	0.96	-0.95	21.86
2007			
DSLW/UMD v2 (MODIS)	0.98	-1.04	15.85
DSLW/UMD v2 (DX)	0.96	-0.33	20.10
ISCCP-FD	0.91	9.34	32.48
ERA-Interim	0.95	-9.01	25.87
NCEP-DOE Re-analysis 2	0.97	-14.82	27.76
GEWEX QC v3.0	0.96	2.01	22.92
GEWEX SRB v3.0	0.96	-1.12	22.22

2008			
DSLW/UMD v2 (MODIS)	0.98	-0.61	15.90
DSLW/UMD v2 (DX)	N/A	N/A	N/A
ISCCP-FD	0.91	11.00	33.22
ERA-Interim	0.95	-10.23	27.33
NCEP-DOE Re-analysis 2	0.97	-16.97	28.26
GEWEX QC v3.0	N/A	N/A	N/A
GEWEX SRB v3.0	N/A	N/A	N/A
2009			
DSLW/UMD v2 (MODIS)	0.98	-1.67	16.34
DSLW/UMD v2 (DX)	N/A	N/A	N/A
ISCCP-FD	0.93	7.12	31.62
ERA-Interim	0.95	-9.75	27.60
NCEP-DOE Re-analysis 2	0.97	-19.40	31.42
GEWEX QC v3.0	N/A	N/A	N/A
GEWEX SRB v3.0	N/A	N/A	N/A

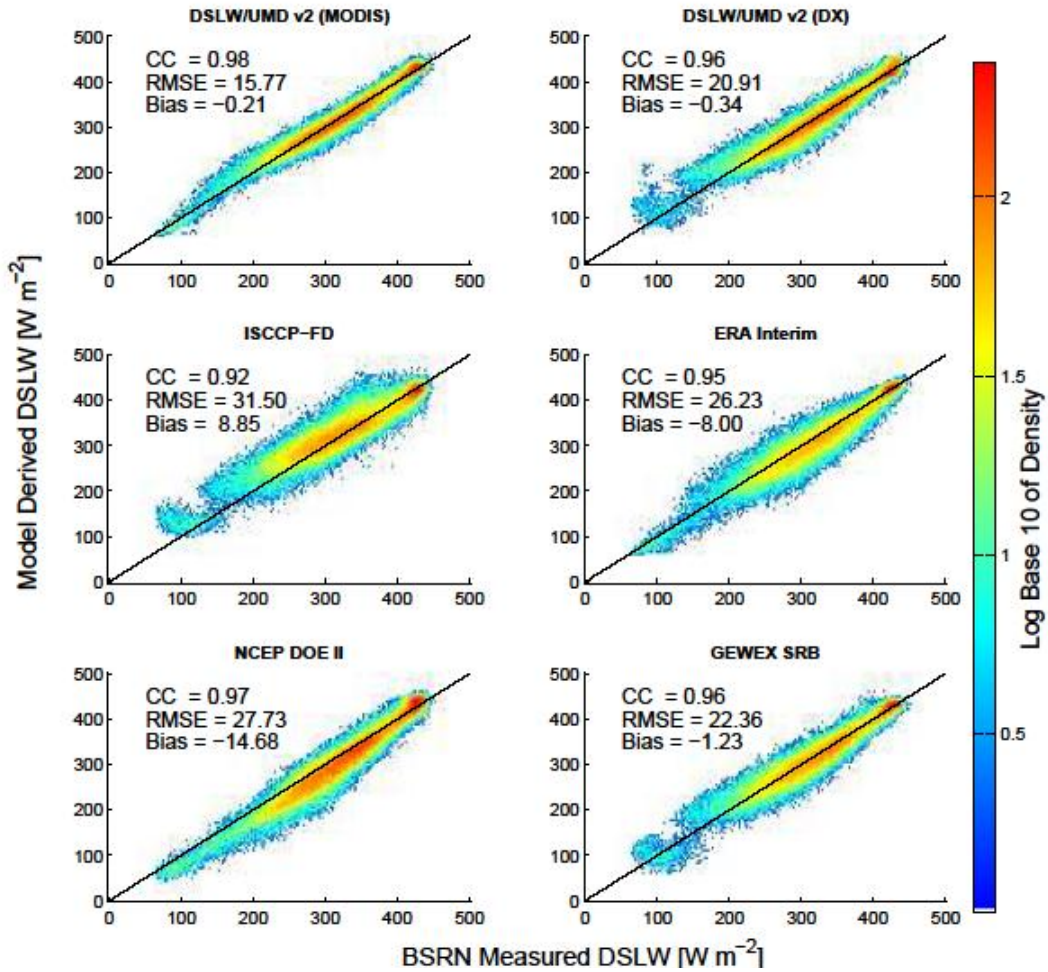


Figure 3.10 Model derived DSLW data versus BSRN ground stations aggregated over 2003 to 2007. The black line follows a one-to-one comparison. The color scale is given as \log_{10} of the density. GEWEX QC is a parameterization based quality control check for GEWEX SRB.

The RMSE between each model output and BSRN ground stations is overlaid on the BSRN geo-location in Figure 3.11. A colored circle is given at the geospatial location of each BSRN ground station. The color of each circle indicates the RMSE (W m^{-2}) between each model and BSRN ground station for

daily averages (2003 to 2007). This gives an idea of the performance of each model in the BSRN geographic locations.

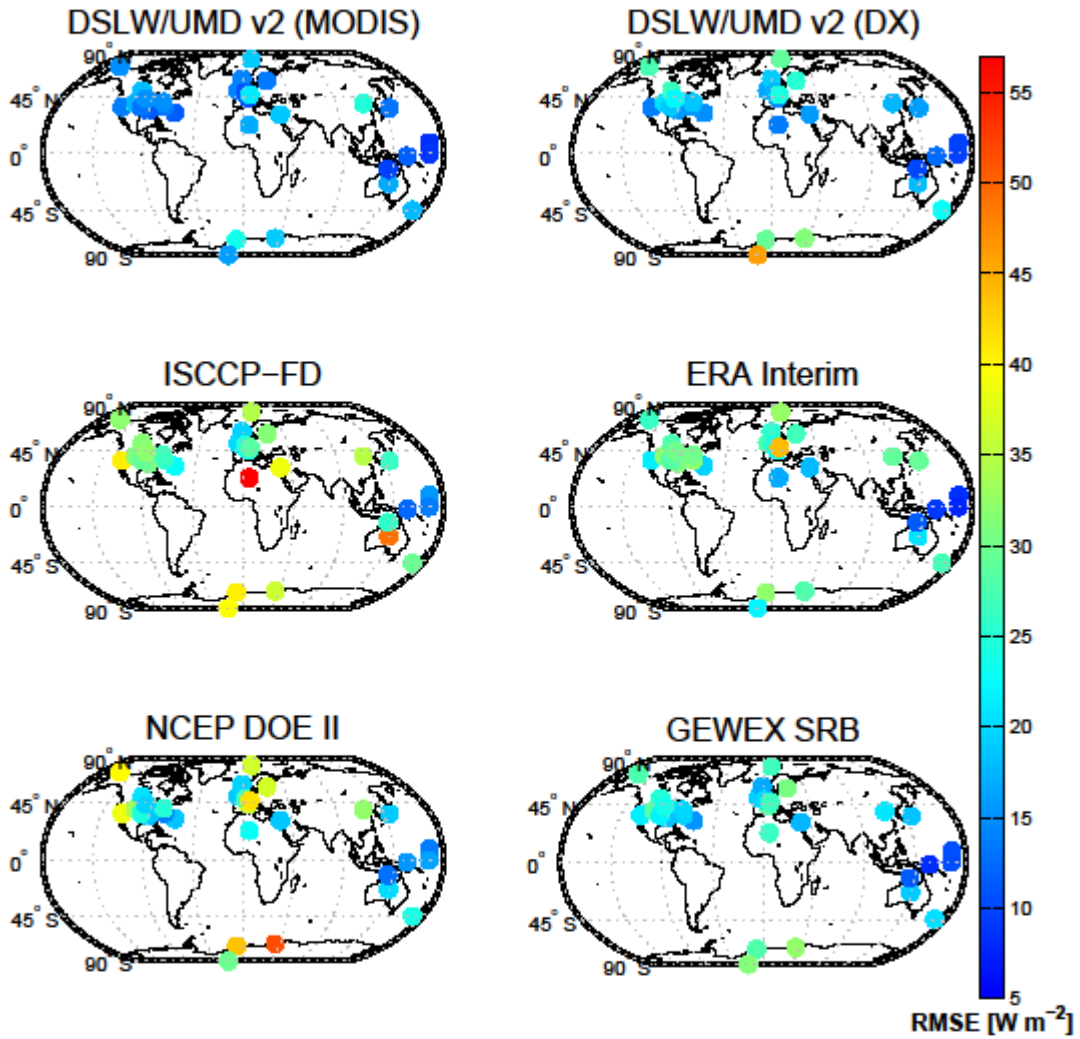


Figure 3.11 A colored circle is given at the geospatial location of each BSRN ground station. The color of each circle indicates the RMSE (W m^{-2}) between each model and BSRN ground station for daily averages (2003-2007).

BSRN ground stations are stratified into Tropical, Mid-Latitude, and Polar latitudinal belts. We define the Tropics as located between -23.5° N and 23.5° N, the Mid-Latitudes between $\pm 66.5^{\circ}$ N and $\pm 23.5^{\circ}$ N, and the Polar Regions between $\pm 66.5^{\circ}$ N and $\pm 90^{\circ}$ N latitudes. The DSLW from the majority of models is in best agreement with observations in the tropical region that has relatively high water vapor and temperature as compared to the other regions. Water vapor has the most influence on DSLW (*Niemela et al.* 2001). Radiative transfer model runs have shown that the majority of the contribution to DSLW comes from within the first few hundred meters of the surface (*Zhao et al.* 1994; *Schmetz et al.* 1986; Figure 2.3). Most parameterizations and radiative transfer based models are well adept at calculating the contribution of DSLW due to water vapor. Therefore, with accurate inputs of water vapor, in areas such as the Tropics the DSLW estimates are in good agreement with observations (Figure 3.12).

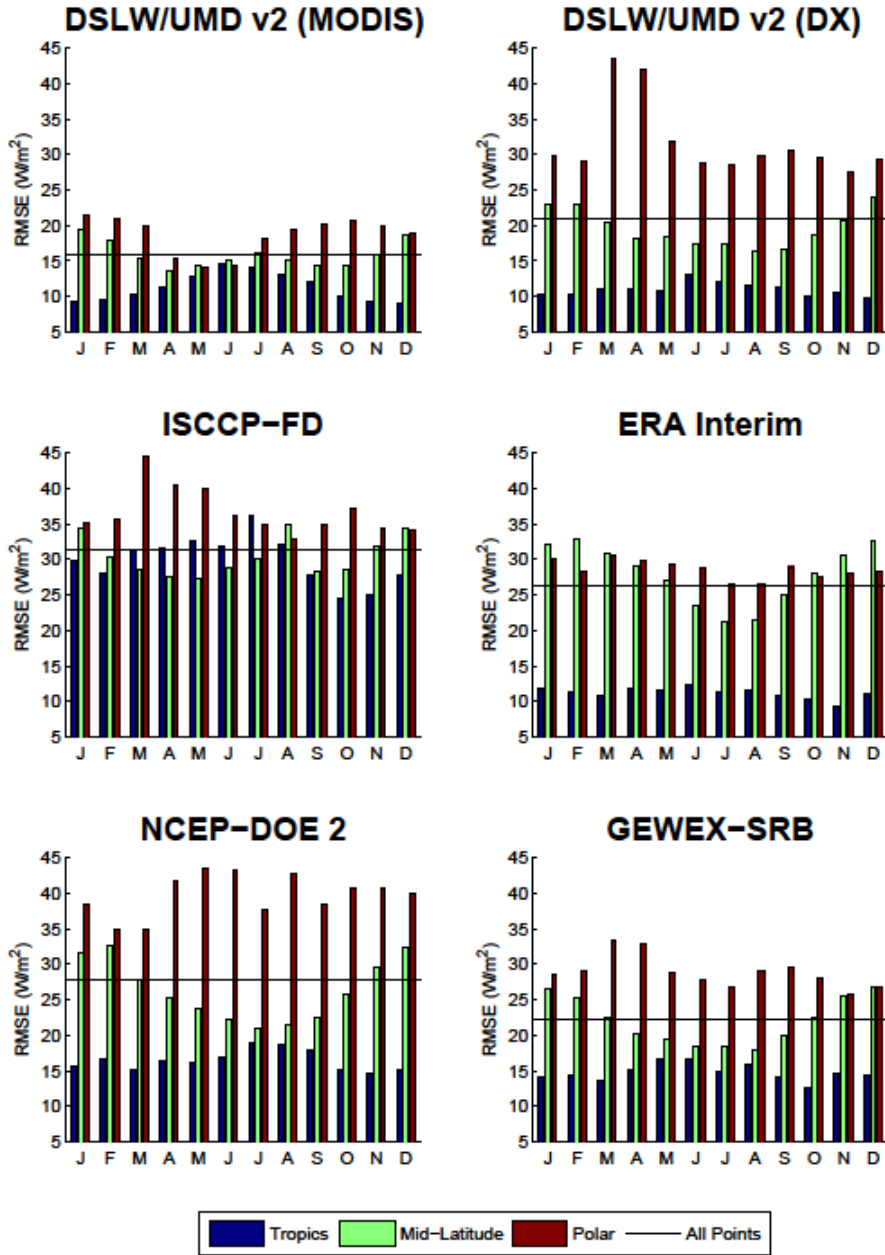


Figure 3.12 The bars for each model represent the average value of RMSE ($W m^{-2}$) for each month for the combined years 2003 to 2007. The comparison is broken down into latitudinal regions: Tropical (blue), Mid-Latitude (green), and Polar (red). The black line is the mean RMSE of all ground stations for the entire period.

Figure 3.12 shows histograms of the monthly averaged RMSE (W m^{-2}) for each latitudinal band. The solid line represents the RMSE for all the data points. One should note that there are two large spikes in the error bars between ground measurements and model calculations for models which use ISCCP-DX (DSLW/UMD v2 [DX], ISCCP-FD, and GEWEX-SRB) data for the months of March and April in the Polar Regions. This was traced to strong disagreements between model estimates and observations at the South Pole, especially at the SPO (South Pole) station. Since each model that utilizes the ISCCP data shows similar timing in the peaks as well as their magnitude, it is believed that this is related to data quality issues. In Figure 3.13, for the years under investigation, we present results of comparison of DSLW calculated by DSLW/UMD v2 model for the South Pole station (SPO), a region of strong disagreement between the DSLW/UMD v2 (MODIS) and DSLW/UMD v2 (DX) as well as over Goodwin Creek Mississippi (GCR), a region of good agreement between the two models. For both stations, the MODIS based DSLW is in good agreement with the BSRN ground measurement.

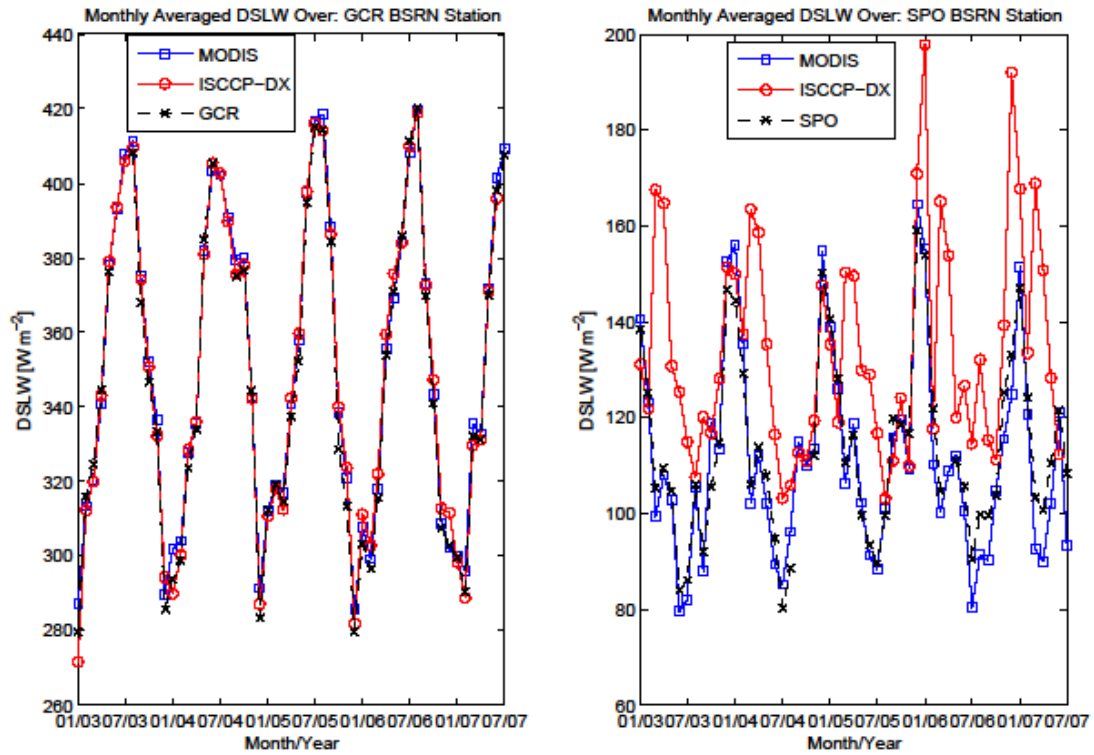


Figure 3.13 The time-series for monthly averaged DSLW calculated by DSLW/UMD v2 from MODIS and DX and measured by a BSRN ground station. DSLW as calculated from DSLW/UMD v2 is taken from the grid cell that includes the BSRN ground station. The GCR BSRN ground station is located at Goodwin Creek in Mississippi, USA. SPO BSRN ground station is located at the South Pole in Antarctica.

The ISCCP-DX based DSLW estimates agree well with the GCR BSRN ground station while the disagreement between ISCCP-DX and MODIS based DSLW estimates and the SPO station observations is quite large. To identify possible reasons for this disagreement we have compared both MODIS and ISCCP-DX cloud top pressure and cloud fraction (Figure 3.14), which are used in calculating the cloud contribution to DSLW over each ground station. There is

good agreement between MODIS and ISCCP-DX cloud properties over GCR where both estimates of DSLW closely track the BSRN observations. Over SPO, both ISCCP-DX cloud fraction and cloud top pressure differ significantly from MODIS where the ISCCP-DX based DSLW product shows strong disagreement with the BSRN ground station. Despite the large discrepancy between DSLW/UMD v2 (DX) and the SPO ground station for the months of March and April, this model provides the best overall agreement with the BSRN ground stations (for all years) out of all ISCCP-DX based models.

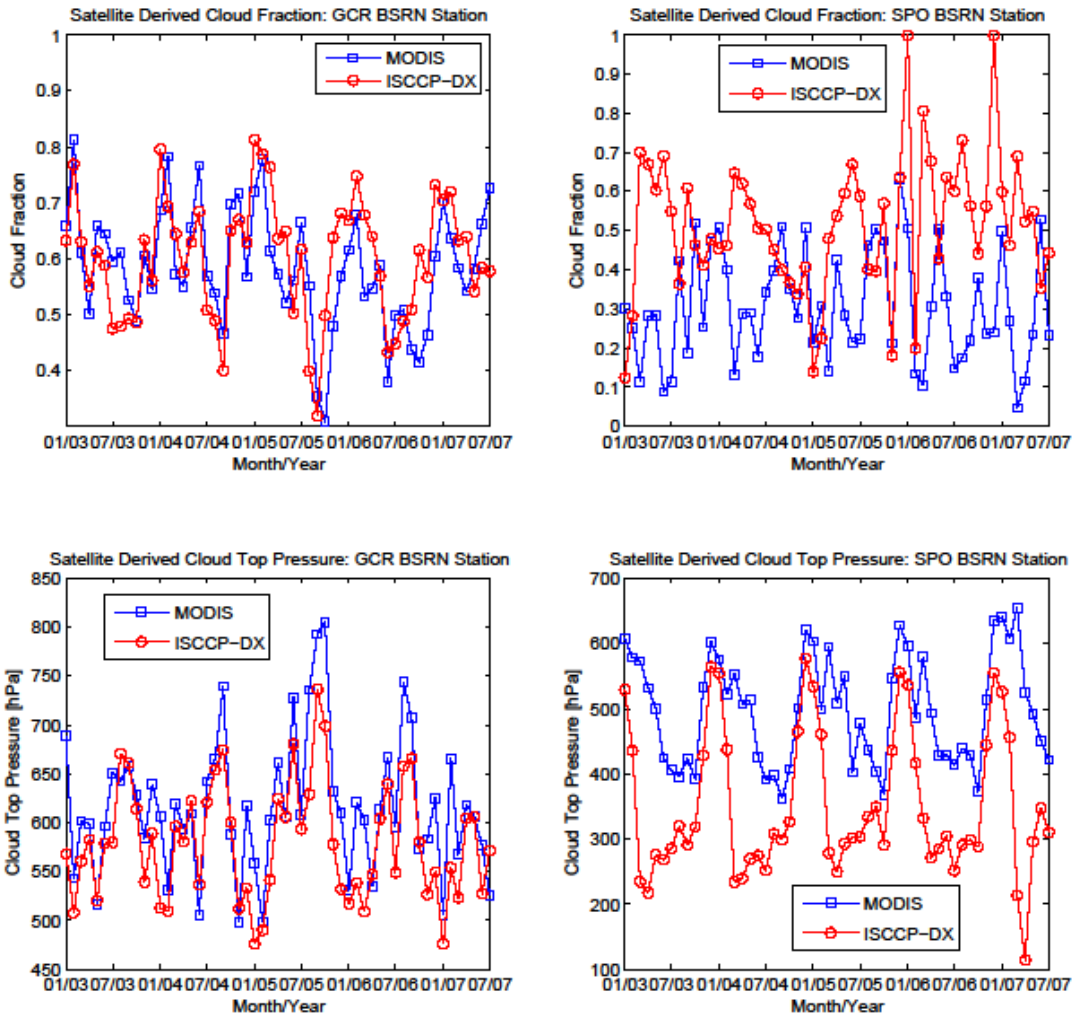


Figure 3.14 Top two figures show the monthly averaged cloud fraction as given by MODIS and ISCCP-DX over GCR and SPO BSRN ground stations. The bottom two figures show the monthly averaged cloud top pressure as given by MODIS and ISCCP-DX over GCR and SPO BSRN ground stations.

Figure 3.15 shows the zonally averaged all sky DSLW derived from each model from daily values averaged over 2003 to 2007. The total global average for each model is also given in the figure. The numerical models that internally generate clouds are denoted by blue lines while the models that derived cloud

information from satellite are denoted by black lines. Compared to the satellite based models the numerical models give an overall lower value of total global DSLW, which can be attributed to lower estimated value for DSLW in the Polar and Mid-Latitude regions. This is consistent with the strong negative bias or underestimation of DSLW by the numerical models as seen in Figure 3.6. The issue of underestimating DSLW from numerical models has been addressed before (*Garratt et al. 1995; Wild et al. 2001*). We postulate that the lower values of DSLW for numerical models are related to the generation of clouds within these models. This is supported by the fact that the under-estimation occurs primarily in the Mid-Latitude and Polar Regions where clouds have the largest influence on DSLW as seen in Figure 3.16 and both DSLW/UMD v2 (MODIS) and GEWEX-SRB models derive their temperature and humidity profiles from re-analysis models.

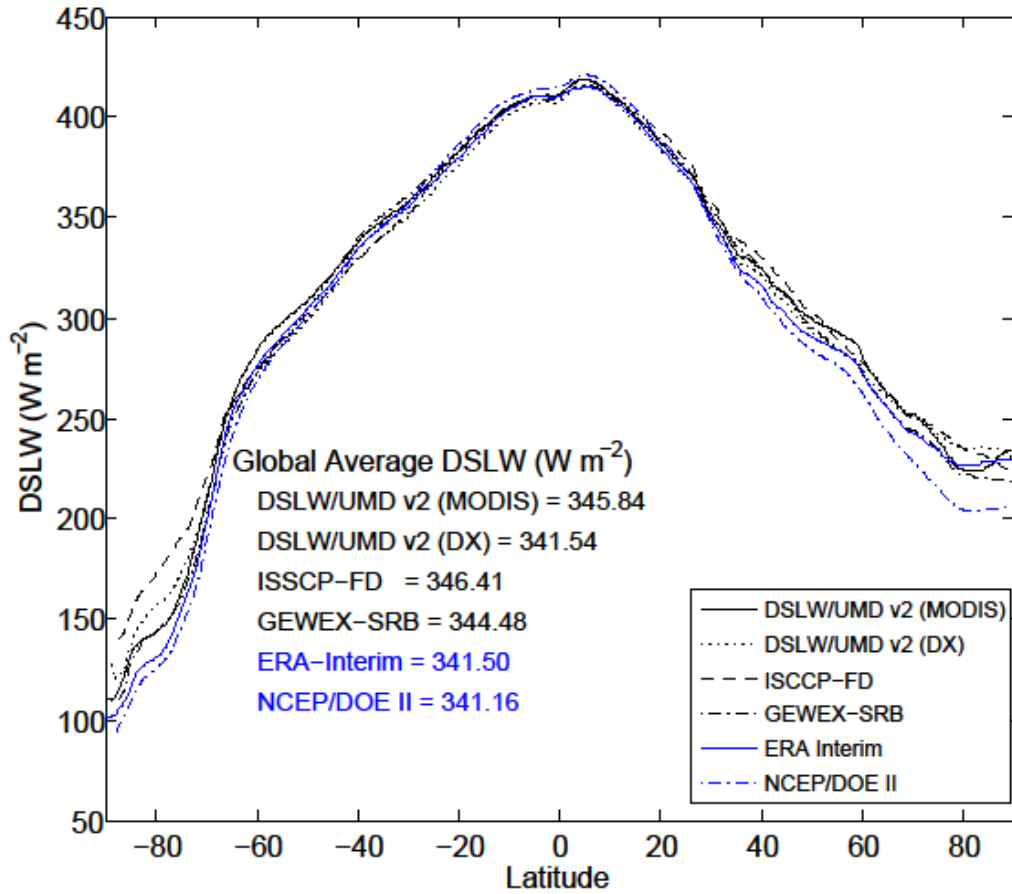


Figure 3.15 Lines represent zonally averaged all sky DSLW each model taken from daily data averaged over 2003 to 2007. The total global average for each model is also given.

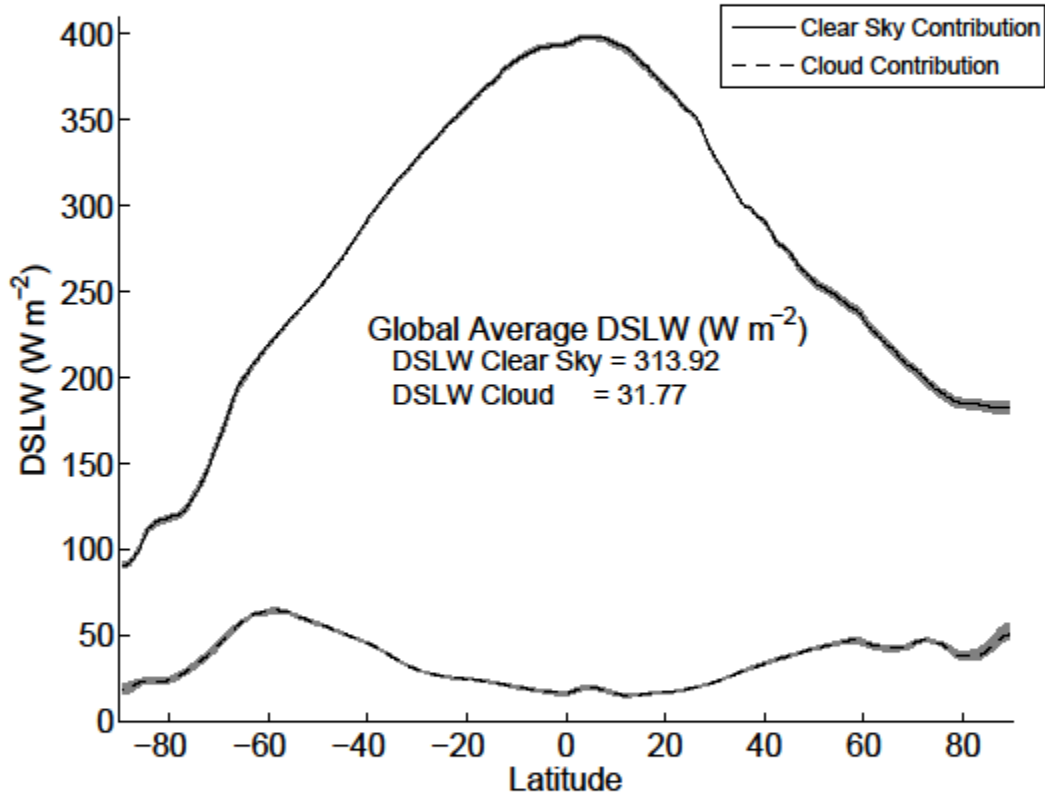


Figure 3.16 Solid-line represents the zonally averaged clear sky contribution to DSLW for all years 2003 to 2009. The dashed-line represents the cloud contribution to DSLW for all years 2003 to 2009. DSLW is calculated from DSLW/UMD v2 (MODIS) model. Shaded region represents the bounds as given by daily data averaged for each year between 2003 and 2009.

The zonal averages for clear sky and cloudy sky averaged over 2003 to 2009 are separated in Figure 3.16. Zonally, the largest influence on DSLW from clouds (65 W m^{-2}) occurs over the Southern Ocean at 60°S . This particular region is marked by extensive cloud cover ($>80\%$) with little seasonality (*Mace et al.* 2007) and cold sea surface temperature which are ideal conditions for larger contributions from clouds to DSLW. The shaded region in Figure 3.16 shows the

variance of daily values averaged over each year. The largest variation for both clear sky and cloud contribution again occur in the North Polar Region. Although the Tropics are known to have extensive and persistent cloud cover, the DSLW due to cloud forcing reaches a minimum in this region. This is due to the high humidity near the surface. Humid boundary layers tend to diminish the impact of clouds on DSLW (*Stephens et al.* 1981) by inhibiting the ability of the atmosphere to transmit longwave flux emitted by clouds to the surface.

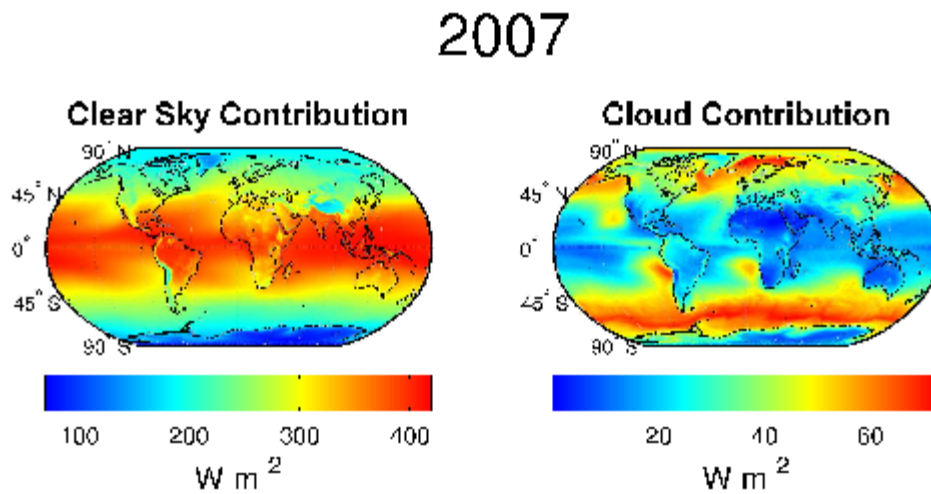


Figure 3.17 Plots of the clear sky and cloud contribution to DSLW from daily values averaged over 2007. DSLW calculations are from DSLW/UMD v2 (MODIS) model.

A sample plot of daily values of clear sky and cloud components (or cloud forcing) of DSLW calculated from DSLW/UMD v2 (MODIS) averaged over 2007 is given in Figure 3.17. Evident from this figure is the strong cloud component over the Southern Ocean and in the North Pole. Also evident is the

effect of orography on the clear sky contribution to DSLW. Higher elevations such as the Tibetan Plateau and the Andes mountains which have cooler temperatures and dryer air, tend to have less clear sky contribution to DSLW. The globally averaged values for each year (2003 to 2009) of clear sky, cloud forcing, and all sky DSLW as well as the globally averaged value for all years is given in Table 3.5.

Table 3.5 Total global clear sky, cloud forcing, and all sky DSLW for each year between 2003 and 2009 along with average aggregated overall years.

Year	Clear Sky DSLW (W m⁻²)	Cloud Forcing (W m⁻²)	All Sky DSLW (W m⁻²)
2003	313.94	31.88	345.82
2004	313.57	31.98	345.55
2005	314.59	31.79	346.38
2006	314.41	31.48	345.89
2007	313.85	32.11	345.96
2008	312.99	31.88	344.87
2009	314.10	31.24	345.34
2003-2009	313.92	31.77	345.69

There is little variation in the all sky DSLW from year to year, where slight increases in clear sky contribution tend to be offset by slight decreases in the cloud forcing and vice versa. The aggregated values of clear sky, cloud

forcing, and all sky DSLW for 2003 to 2009 are significantly different than those reported by *Kiehl et al. (1997)* who gave values of clear sky, cloud forcing, and all sky DSLW as: 278 W m^{-2} , 46 W m^{-2} , and 324 W m^{-2} , respectively. Although the values from *Kiehl et al. (1997)* were based on data from the Earth Radiation Budget Experiment (ERBE) that occurred during mid-1980's the differences are too large to be caused by changes in absorbing species. Using Global Climate Models (GCMs), *Wild et al. (1997)* showed that the doubling of CO_2 led to mean global increase of DSLW of about 10 W m^{-2} . The difference in clear sky between DSLW/UMD v2 (MODIS) and *Kiehl et al. (1997)*, is $\sim 36 \text{ W m}^{-2}$. In addition, *Trenberth et al. (2009)* provide an updated value for global all sky DSLW using CERES data from March 2000 to May 2004. Their value of 333 W m^{-2} is also significantly lower than the results found using DSLW/UMD v2 and when compared to the satellite models (ISCCP-FD and GEWEX-SRB) and numerical analysis models (NCEP/DOE II and ERA-Interim).

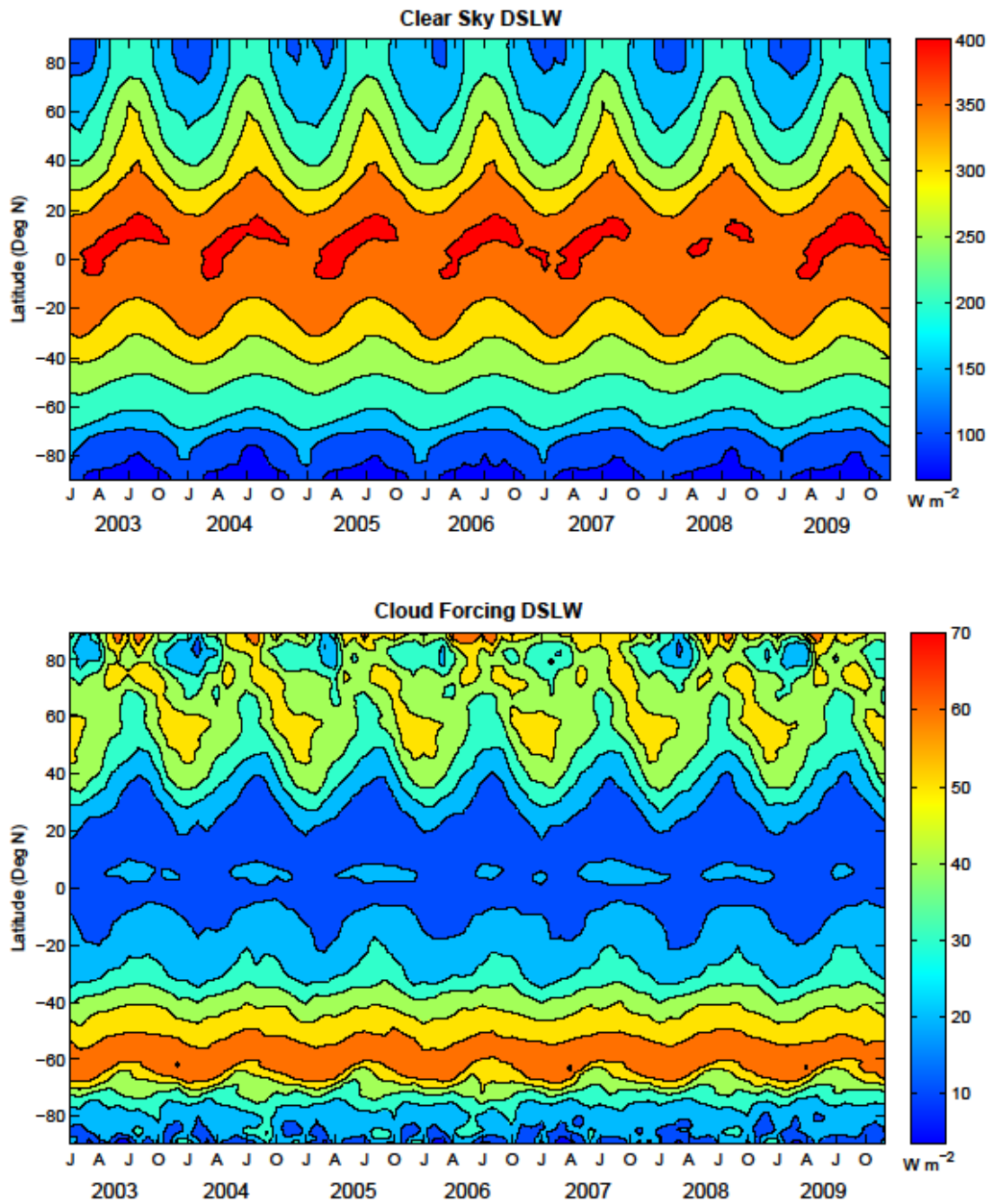


Figure 3.18 Monthly and zonally averaged clear sky DSLW and cloud forcing DSLW for 2003 to 2009.

Evident from Figure 3.18 is the strong annual cycle of both the clear sky and cloud forcing portion of DSLW. The ordinates are latitude bands averaged over longitude. The abscissas are monthly averages. The annual cycle is related to the change in the atmospheric temperature profile with regard to season. The Northern Hemisphere (NH) exhibits larger changes in both clear and cloud forcing compared to the Southern Hemisphere (SH), due to the differences in thermal inertia between the continental land mass in the NH and the oceans in the SH. The farther into the Polar Regions one goes the less there is a correlation between annual cycle and cloud forcing DSLW. The largest seasonal variability in cloud forcing can be seen in the Arctic region.

3.5. Conclusion

We have developed a new clear sky parameterization based on radiative transfer model computations using atmospheric re-analysis outputs and optimizing previous cloud contribution parameterizations with newly available information on clouds from high resolution MODIS data, meteorological parameters from ERA-Interim re-analysis, and a cloud vertical structure statistical model. We show that when compared to a global network of BSRN ground stations this approach (DSLW/UMD v1) predicts DSLW better than four radiative transfer based models.

Upon inspection and evaluation of DSLW/UMD v1 and other models, we determined areas where improvements in the estimation of DSLW are needed.

This led to the development of an artificial neural network framework for calculating the clear sky contribution to DSLW based on the RRTM and atmospheric re-analysis parameters, and the cloud contribution to DSLW based on the passive satellite observations of MODIS and atmospheric re-analysis parameters. The calculation of the cloud contribution to DSLW was aided by bridging the gap between global coverage of cloud top properties from passive satellite sensors and detailed vertical structure information from active sensors, using an artificial neural network to determine cloud base temperature. Training of the model was accomplished with co-located satellite data from MODIS, CPR, and CALIOP. We demonstrate that when compared to a global network of BSRN ground stations this approach predicts daily average DSLW better than radiative transfer based satellite inference schemes as well as a parameterization based model.

The results confirm that high quality representations of atmospheric water vapor and near surface temperature are essential for accurate modeling of DSLW within the Tropics. Within the Mid-Latitude region, a combination of water vapor, temperature, and clouds play a critical role in modeling DSLW, while in the Polar Regions, the importance of clouds for the estimation of DSLW is significant.

It is obvious from Figure 3.4 that the BSRN ground stations are not evenly distributed, which may influence the results of the evaluation. Separating into latitudinal regions helps to identify some of the reasons for the biases. For a more comprehensive evaluation, there is a need for additional ground stations in locations such as South America, Africa, the Arctic and Antarctic, and the Tibetan

Plateau. Regions such as the Arctic, Antarctic, and Tibetan Plateau should be of high priority because the cold and dry nature of these locations makes the influence of clouds on DSLW an important factor.

The models used in the comparison were implemented at a variety of spatial resolutions from 1° to 2.5° . Since water vapor, temperature, and clouds are highly spatially variable and have a significant impact on DSLW, model resolution plays an important role in the correlation between a grid cell model derived DSLW and a point measured value of DSLW. Possibly, the model resolution may play a role in the larger difference between the ISCCP-FD based estimates and BSRN observations.

We have shown evidence that the numerical models which internally generate clouds tend to under-predict values of DSLW in Mid-Latitudes and Polar Regions. Preliminary evidence points to this to be related to cloud contribution within the numerical models; however, further study is needed.

Chapter 4: Application to Arctic Sea Ice Melt

4.1. Abstract

Understanding the mechanisms behind the changes in the Arctic sea ice is quite challenging. Such changes have a broad implication in many areas such as climate, ecosystem development, and natural resource availability. The most immediate ecological changes are occurring for species that depend on sea ice for foraging, reproduction, and predator avoidance (*Post et al.* 2009). The loss of sea ice opens up the important North-East and North-West shipping passages during the summertime and allows access to the vast reserve of natural resources located beneath the Arctic sea floor. The United States Geological Survey (USGS) estimates that 22% of the world's undiscovered and recoverable oil and natural gas/liquid reserves may be located within the seafloor of the Arctic Region (*United States Geological Survey* 2008).

Satellite observations (1979 to present) have provided the tool to observe changes in the Arctic sea ice extent. These changes can be viewed on two temporal scales. A long-term trend (1979 to 2011) of decreasing sea ice extent that follows a slope of $-6.6 (+/- 1.8)$ % per decade as measured by a least squares regression of the ice extent anomalies for the month of October and seasonal oscillation of melt and freeze. The seasonal change in Arctic sea ice can be examined through the monthly sea ice concentration anomaly, where a given month's concentration is subtracted from a climatological mean (1979 to 2007)

established for that month.

In 2007, satellite observations revealed the largest seasonal change in sea ice extent since measurement began in 1979. The annual minimum sea ice extent in 2007 was 24% below the previous record set in 2005 and 37% lower than the 1979 to 2006 average (*Comiso et al. 2008*). The primary driving force behind the varying magnitudes in seasonal Arctic sea ice anomaly remains a mystery. Several factors are believed to play a role in the modulation of Arctic sea ice (*Kay et al. 2008*), although the relative contribution of each of these factors is unknown. They include: the thickness of sea ice (*Nghiem et al. 2007*), the ice-albedo feedback (*Perovich et al. 2007a, 2007b, 2008*), Arctic ocean heat transport (*Shimada et al. 2006*), atmospheric heat transport (*Serreze et al. 2007*), transport of sea ice through wind stress (*Rigor and Wallace 2004; Ogi and Wallace 2007*), and downwelling radiation (*Kay et al. 2008; Schweiger et al. 2007; Francis and Hunter 2006*). Since atmospheric profile temperature is the source function for DSLW and humidity affects the transmission of longwave radiation from the atmosphere to the surface, the evaluation of DSLW in the role of sea ice anomalies strongly overlaps with the role of atmospheric heat transport in sea ice anomalies. The relative contribution of each of these factors is unknown.

Several recent advancements in observation and modeling of high latitude regions provide a means to investigate the role of radiative components in Arctic sea ice anomalies. These include the improved estimates of DSLW obtained from DSLW/UMD v2 model, better retrievals of downwelling surface shortwave radiation (DSSW) from the DSSW/UMD model (*Niu et al. 2010*), which has been

optimized for high latitudes, as well as newly improved satellite and re-analysis data utilized as input for these models. Using these tools, the correlation between Arctic sea ice concentration and four radiative components are examined individually for the period 2003 - 2007. The radiative components are: all sky DSLW, all sky DSSW, all sky total downwelling shortwave and longwave radiation (DSSW + DSLW), and total cloud forcing. It is important to note that correlation does not imply causation. This is to say, showing a correlation between the radiative components and sea ice concentration is not sufficient to imply that one causes the other. In addition, we examine the relationship between the radiative components and sea ice concentration *anomalies* to determine if any of these components are responsible for the large 2007 sea ice concentration anomaly.

A previous study of *Kay et al. (2008)* related an increase in downwelling shortwave radiation due to an unseasonal reduction in cloudiness to the 2007 sea ice anomaly. *Schweiger et al. (2007)* ran the Pan-arctic Ice-Ocean Modeling and Assimilation System (PIOMAS) model and reported that downwelling shortwave radiation did not play a significant role in the 2007 sea ice anomaly. They further speculated that DSLW may have significantly contributed to the 2007 anomaly. In this study, we show over the region expressing the largest negative sea ice concentration anomaly for 2007 that the cloud fraction was not at a minimum and DSSW was not at a maximum as claimed by *Kay et al. (2008)*. We also show that part of the region analyzed by *Kay et al. (2008)* does not exhibit the large 2007 sea ice loss anomaly; rather, it follows the climatological mean. Ironically, this

area has the lowest average cloud fraction during the 2007 melting period.

Although we show there is significant correlation between radiative components and sea ice concentration, we show observational evidence that neither DSSW nor DSLW nor cloud forcing (including longwave and shortwave) are the primary drivers for the 2007 anomaly or other anomalies between 2003 and 2007.

4.2. Methodology

4.2.1. Downwelling Surface Longwave Radiation (DSLW)

For this study the DSLW/UMD v2 model has been adapted specifically for the Arctic Region by training both the clear sky and cloud base temperature neural networks with data limited to above 60°N. The model was evaluated at both daily and monthly timescales utilizing two North Pole ground stations from the Baseline Surface Radiation Network (BSRN) and the U.S. Department of Energy Atmospheric Radiation Measurement (ARM) Climate Research Facility. The ARM station is located in Barrow, Alaska (71.32° N, 203.4° E) (NSA), and BSRN facility is in Ny-Alesund, Spitsbergen (78.92° N, 11.95° E) (NYA). The estimated DSLW shows good agreement on both a daily and monthly time scale, from 2003 to 2007, with the ARM stations as summarized in Table 4.1. The correlations indicated in Table 4.1 have a p-value of 0.000 indicating that they are significant. Figure 4.1 shows a time series comparison of monthly averaged DSLW for the DSLW/UMD v2 model and ground stations.

Table 4.1 A summary of the correlation statistics between DSLW estimated from the DSLW/UMD v2 Polar model and two ARM ground stations. Comparison was done on a daily and monthly time scale.

Time Scale	Station	Correlation	Bias (W m^{-2})	RMSE (W m^{-2})
Daily	NSA	0.97	2.02	14.96
	NYA	0.94	0.03	18.44
Monthly	NSA	0.99	2.80	8.11
	NYA	0.99	0.33	8.13

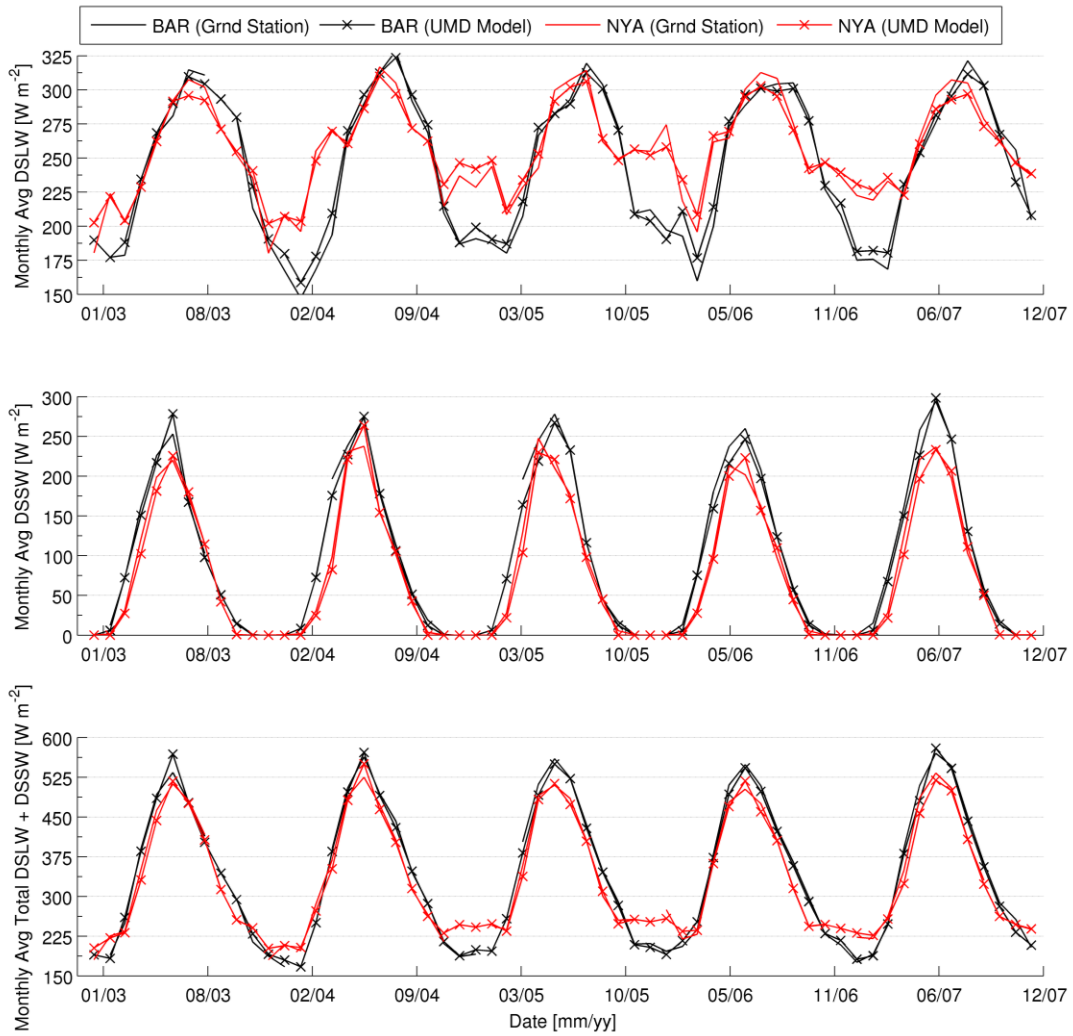


Figure 4.1 Comparison of monthly averaged values of DSSW, DSLW, and DSSW + DSLW, as calculated by the UMD models and observed by ground stations (NSA and NYA) for the period 2003-2007.

4.2.2. Downwelling Surface Shortwave Radiation (DSSW)

An inference scheme, for deriving DSSW fluxes that utilizes MODIS Level-3 Atmosphere Daily Global Product information was used (*Wang and Pinker 2009*). Information is available on atmospheric constituents, both water

and ice cloud properties and surface albedo. The spectral shortwave radiation is retrieved for a multi-layered atmosphere which accounts for surface elevation and for the representation of the vertical distribution of atmospheric variables.

The DSSW/UMD model has been updated to incorporate improved information on surface properties at high latitudes (*Niu et al.* 2010). Snow cover resolution has been increased from 0.25° to 0.05° at daily and monthly time scales. These MODIS snow cover products are available from the National Snow and Ice Data Center (NSIDC)

(http://nsidc.org/data/modis/data_summaries/index.html). While the original scheme used monthly mean sea ice extent at 1° (~ 111 km) resolution from the Special Sensor Microwave/Imager (SSM/I, NOAA/NESDIS National Climate Data Center [NCDC]), the updated version uses 25 km sea ice concentrations at both daily and monthly time scales as derived from the Nimbus-7 Scanning Multichannel Microwave Radiometer (SMMR) and the Defense Meteorological Satellite Program (DMSP) SSM/I (based on a NASA algorithm (*Cavalieri et al.*, 1996 and updated in 2008) (<http://nsidc.org/data/nsidc-0051.html>). The fixed values of spectral reflectance of sea ice in the original scheme have been updated for four distinct phases in the margin areas of the Arctic (winter stationary, spring melt season, summer stationary, and autumn freeze up) according to *Zhang et al.* (2003) and *Belchansky et al.* (2004). Since the daily snow cover has many missing values at high latitudes, they have been replaced with monthly mean values.

On a daily and monthly timescales, from 2003 to 2007, estimations of

DSSW from DSSW/UMD agree well with ARM ground station data as summarized in Table 4.2. The correlations have a p-value of 0.000, indicating that the correlation is significant. Figure 4.1 shows a time series comparison of monthly averaged DSSW for the DSLW/UMD v2 model and ground stations.

Table 4.2 A summary of the correlation statistics between DSSW estimated from the DSLW/UMD v2 Polar model and two ARM ground stations. Comparison was done on a daily and monthly time scale.

Time Scale	Station	Correlation	Bias (W m^{-2})	RMSE (W m^{-2})
Daily	NSA	0.99	-4.92	18.80
	NYA	0.97	-1.82	25.34
Monthly	NSA	0.99	-5.13	10.64
	NYA	1.00	-2.32	10.22

4.2.3. Sea Ice Data

Arctic sea ice concentration anomaly is calculated by taking the difference between a monthly climatology of sea ice concentration and the actual monthly concentration. The monthly climatology represents a mean ice concentration for each month of the year derived from data from 1979 to 2007. The actual monthly concentration is derived using measurements from the SMMR on the Nimbus-7 satellite and from three SSM/I sensors on DMSP F8, F11, and F13 satellites (Comiso 1999, updated 2008). This data set is generated using the Advanced Microwave Scanning Radiometer – Earth Observing System (AMSR-E) Bootstrap Algorithm with daily varying tie-points. Both data-sets are available

from the National Snow and Ice Data Center (NSIDC, <http://nsidc.org/data/nsidc-0051.html>).

4.2.4. Equal Area Comparison

The importance of applying an equal area grid for comparison of quantities in the Arctic should not be ignored. When taking averages of various spatial regions in the Arctic it is important that each grid cell is of the same area such that its contribution to the average is not misrepresented. In the Polar Regions (60°N to 90°N) the area of a 1° by 1° grid cell can range from 6,123 km² (centered at 60.5°N latitude) to 109 km² (centered at 89.5°N latitude). One can use a weighted mean, weighted by the area of each grid cell or develop the mean from an equal area grid. The analysis presented here conforms to the latter.

4.3. Results

4.3.1. Cloud Fraction and Arctic Sea Ice Melt Area

The analysis done in *Kay et al.* (2008) is for the Western Arctic 120°W to 180°W (180°E to 240°E) and 70°N to 90°N. This is the region they chose to represent the large 2007 Arctic sea ice concentration anomaly. Within this region they claim that a “reduced cloudiness and enhanced downwelling shortwave radiation contributed to the record 2007 sea ice extent loss.” However, closer inspection of this region shows that this may not necessarily be the case.

Subdividing the *Kay et al.* (2008) region 180°E to 240°E, it can be seen

that half of this region, namely, 180° E to 210° E, represents the large 2007 sea ice concentration anomaly. The other half, 210° E to 240° E, exhibits melting similar to the climatological mean calculated from 1979 to 2007. The time series of Arctic sea ice concentration anomaly for the regions, 180° E to 210° E/70° N to 90° N and 210° E to 240° E/70° N to 90° N is shown in Figure 4.2a and Figure 4.2b. Evident from this figure is that the 180° E to 240° E region inspected by *Kay et al.* (2008) does not include the most dramatic decreases in sea ice that occurs in the region 150° E to 180° E. In addition, region 120° E to 150° E also shows significant decrease in sea ice concentration in 2007. The monthly averaged sea ice anomaly over the entire Arctic for October 2007, which is the month of the most dramatic decrease in sea ice concentration anomaly, is shown in Figure 4.3. Upon inspection of Figure 4.3 one can see that a region of interest for analyzing the sea ice concentration anomaly is 120° E to 210° E, confirming the findings from Figure 4.2.

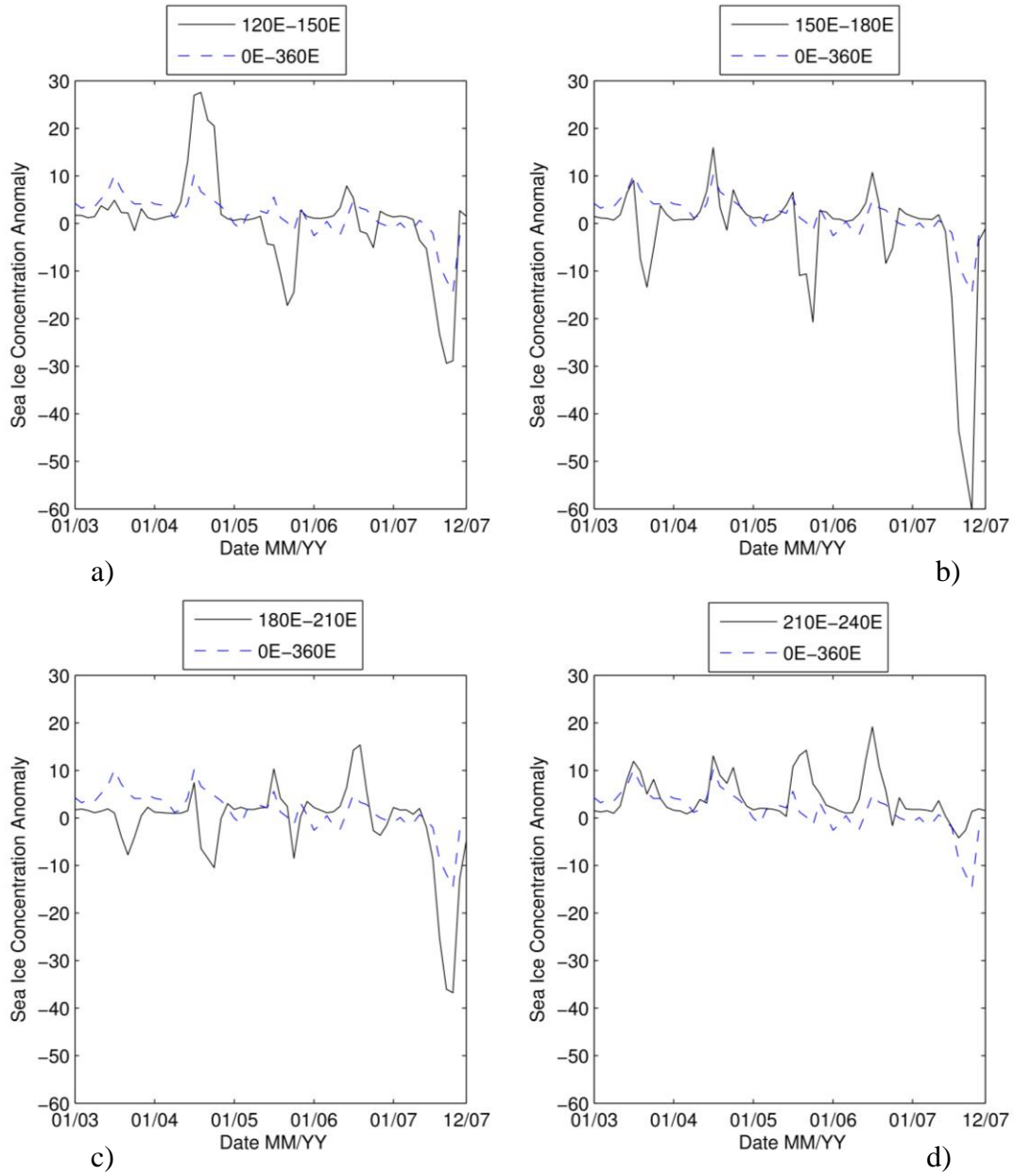


Figure 4.2 Time-series of Arctic sea ice concentration anomalies for different regions of the Arctic. Graphs c) and d) make up the region analyzed by *Kay et al.* (2008), 180° E to 240° E. Graphs a) and b) show additional regions displaying the characteristic 2007 large decrease in sea ice with the region 150° E to 180° E showing the largest anomaly.

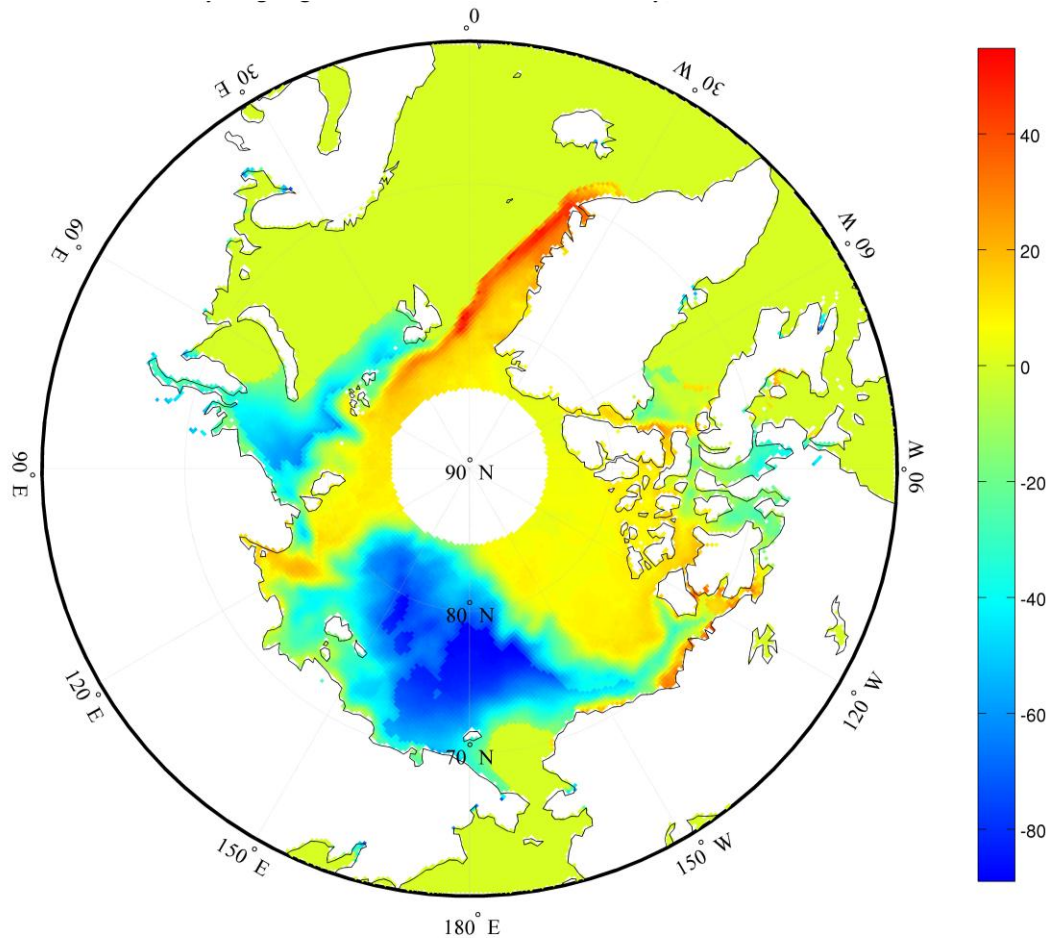


Figure 4.3 Monthly averaged Arctic sea ice concentration anomaly for October 2007. This time represents when the 2007 sea ice concentration anomaly was at its largest (negative) value.

Kay et al. (2008) used observations from MODIS, CloudSat, and CALIOP to show that the region 180° E to 240° E exhibits large reductions in cloud fractions during the 2007 melt period. Our analysis confirms this result; however, closer inspection of the region reveals a different conclusion regarding the link between cloud fraction and sea ice concentration anomalies. As previously mentioned, half of the region displayed the large decrease in sea ice concentration

anomaly for 2007 and the other half was similar to the climatological mean. This region has the lowest cloud fraction for June, July, and August in 2007 (Figure 4.4). In the region that shows the largest decrease in sea ice concentration anomaly in 2007, the lowest cloud fraction occurs in June, July, and August of 2005, not 2007 (Figure 4.5).

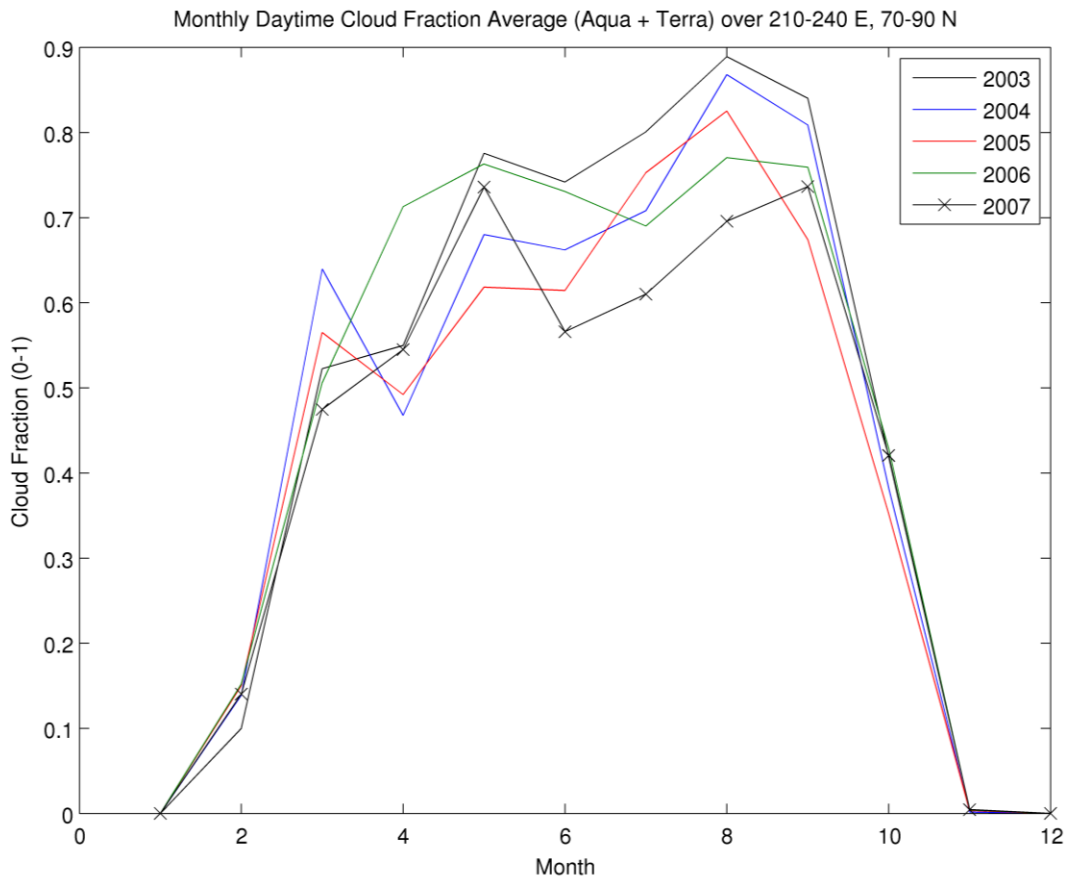


Figure 4.4 Monthly averaged daytime cloud fraction from MODIS using both Aqua and Terra spacecraft over 180° E to 210° E and 70° N to 90° N region.

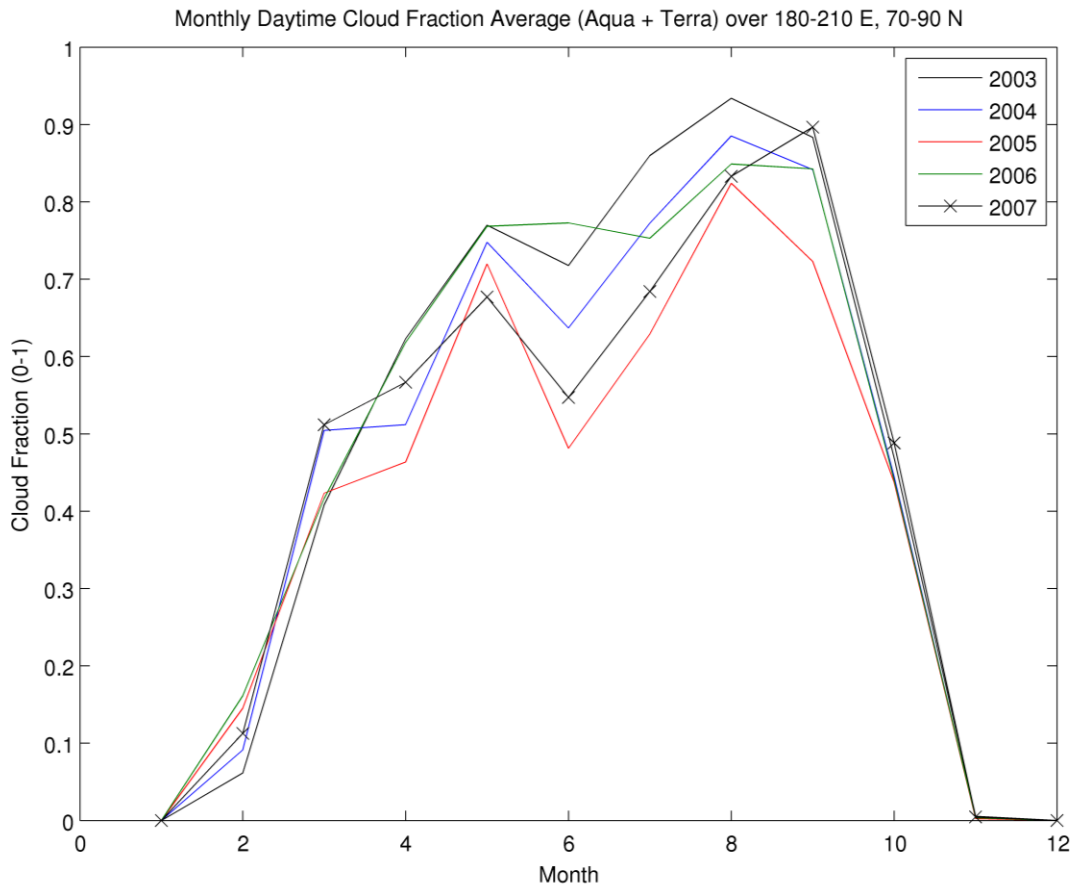


Figure 4.5 Monthly averaged daytime cloud fraction from MODIS using both Aqua and Terra spacecraft over 180° E to 210° E and 70° N to 90° N region.

The Arctic region from 90° N to 70° N and 120° E to 210° E includes the record setting Arctic sea ice loss in the 2007 melt season, during which the monthly ice extent was 23% smaller than the previous record in 2005 (*Stroeve et al.* 2008). This region was chosen because it captures a large majority of the most dramatic loss in sea ice to date (Figure 4.2). Initially, the cloud fraction from MODIS daytime observations over this region is examined (Figure 4.6) illustrating that during the months of June, July, and August the year 2005 had a lower cloud fraction than 2007, and that 2004 had a lower cloud fraction for July and August than 2007. This supports the idea that DSSW is not a primary driver for Arctic sea ice concentration anomalies. A summary of the cloud fraction for the regions discussed in this section is given in Table 4.3, which shows that the region 120° E to 210° E is representative of the majority of the 2007 sea ice loss. The region defined by 180° E to 240° E was used by *Kay et al.* (2008) for the claim that DSSW was the cause of the 2007 sea ice concentration anomaly. A portion of this region, 180° E to 210° E exhibits the large sea ice concentration anomaly of 2007; however, half of this region, 210° E to 240° E, shows positive or no significant sea ice concentration anomaly for 2007.

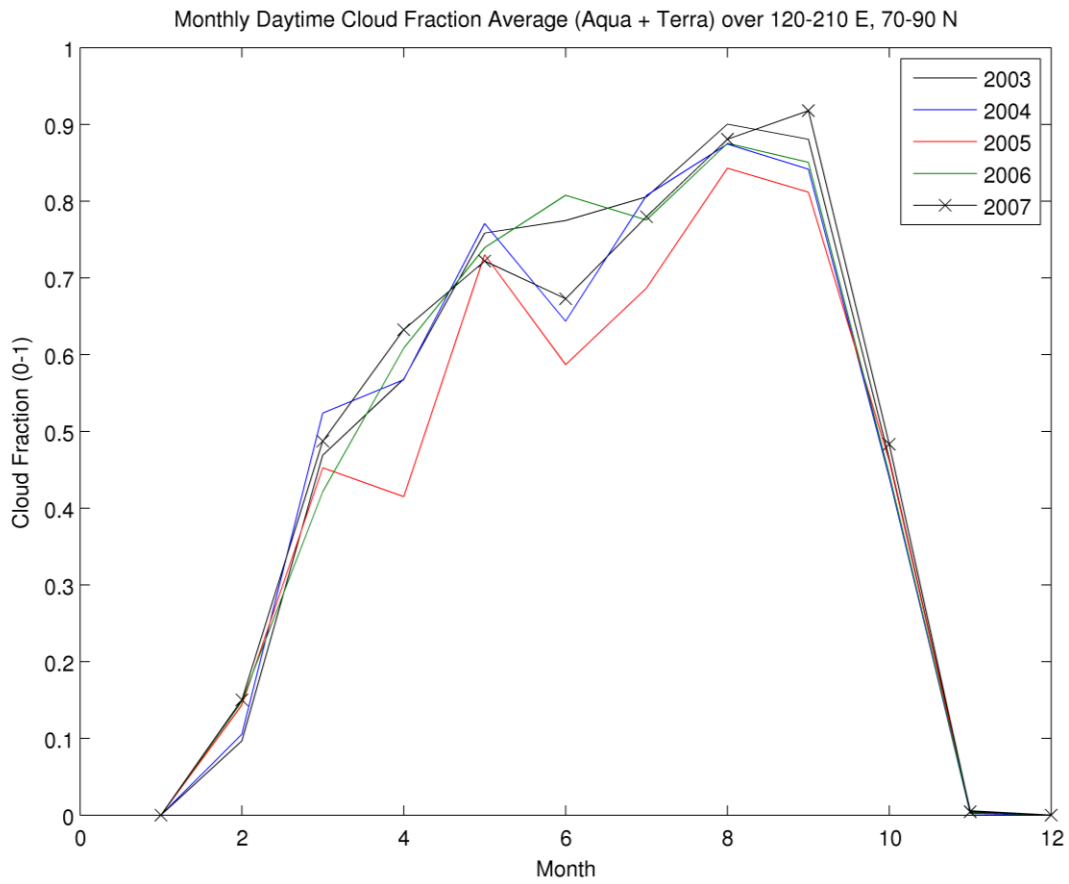


Figure 4.6 Monthly averaged daytime cloud fraction from MODIS using both Aqua and Terra spacecraft over 120° E to 210° E and 70° N to 90° N region.

Table 4.3 A summary of the cloud fractions averaged over June, July and August for years 2003 to 2007 for each region discussed in this section. Red numbers indicate the lowest cloud fraction for melt year.

	<i>Melt Year</i>				
	2003 (JJA)	2004 (JJA)	2005 (JJA)	2006 (JJA)	2007 (JJA)
120°E-210°E	0.827	0.775	0.705	0.819	0.778
180°E-240°E	0.824	0.755	0.688	0.761	0.656
180°E-210°E	0.837	0.765	0.645	0.791	0.688
210°E-240°E	0.811	0.746	0.731	0.731	0.624

4.3.2. Radiant Exposure

In order to evaluate the role of various radiation components as primary drivers to the sea ice anomalies from 2003 to 2007 we first define several useful quantities. One is the cumulative sum of the radiant exposure for each melt year. Radiant exposure has the units of J m^{-2} and is estimated by multiplying the monthly average value of irradiance by the number of seconds within the month. For each year between 2003 and 2007 the cumulative sum of radiant exposure was calculated beginning on January of each year. The cumulative sum of the radiant exposure tracks the energy density that an area has received since the beginning of the year, allowing one to compare the amount of energy received from a specific radiation component prior to the beginning of seasonal melt (or specific anomaly) for each year. If a specific component of radiation is considered a primary driver of sea ice anomalous events then there should be a correlation

between the cumulative sum of radiant exposure and the event. The radiant exposure is useful when evaluating the relationship between DSLW and sea ice concentration. Unlike DSSW, DSLW occurs even when sunlight is not present (i.e., during the Arctic winter). Using the radiant exposure as a metric for comparison allows a similar starting point for each year investigated. This is similar to the initial value of DSSW which is 0 W m^{-2} at the beginning of each year. The next component of interest is cloud forcing defined as the sum of cloud contribution to DSLW and the cloud contribution to DSSW, where the cloud contribution to either longwave or shortwave is the all sky flux less the clear sky flux.

The cumulative sum of the radiant exposure due to DSSW, DSLW, DSSW + DSLW and cloud forcing along with the sea ice anomaly is displayed in Figure 4.7. For this region and time period the sea ice anomaly shows a biennial characteristic, with local minima and maxima occurring every two years.

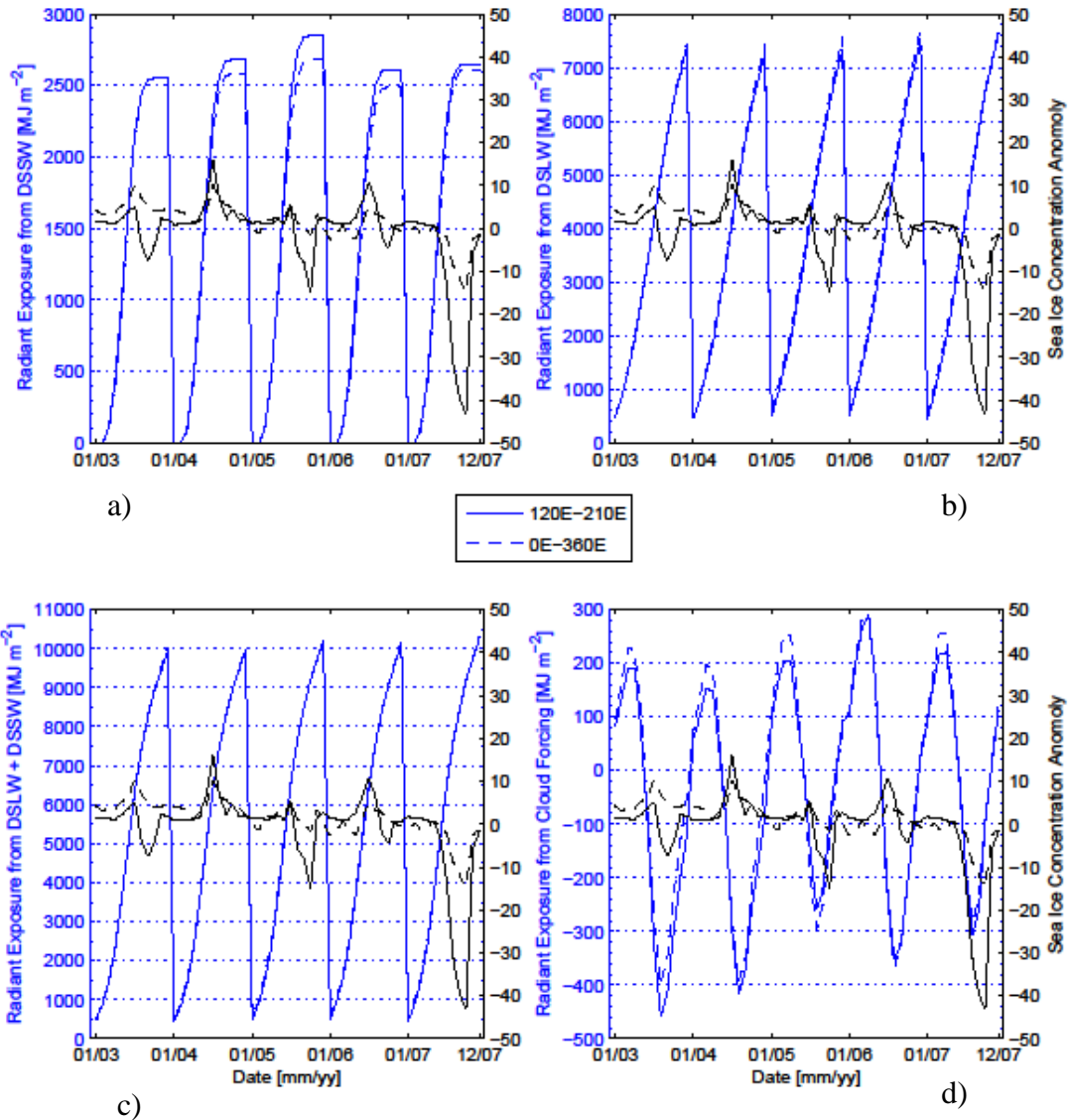


Figure 4.7 Shows the cumulated radiant exposure for DSSW (a), DSLW (b), DSSW + DSLW (c), and Cloud Forcing (d) cumulated from the beginning of each year along with the monthly averaged sea ice concentration anomaly. The solid line represents the area from 120° E to 210° E while the dashed line represents 0° E to 360° E.

4.3.3. DSSW

Figure 4.7a shows the cumulative radiant exposure for DSSW for each year along with the sea ice concentration anomaly. It shows, as noted by others (Kay *et al.* 2008), that there was an increase in downwelling shortwave radiation in 2007 as compared to 2006. The maximum radiant exposure for 2007 was 2650 MJ m⁻² while the maximum radiant exposure for 2006 was 2611 MJ m⁻² (Table 4.4); it also shows that from 2003 to 2007 there were two years with greater radiant exposure than 2007. The maximum radiant exposure during 2005 was significantly greater than 2007 with a value of 2850 MJ m⁻² and 2004 had a value of 2680 MJ m⁻². One should also note that during 2004, the second highest year in terms of maximum radiant exposure due to DSSW, a positive sea ice concentration anomaly was seen throughout the year. The numerical values of yearly maximum radiant exposure are given in Table 4.4 and graphically displayed in Figure 4.8.

Table 4.4 Maximum value of radiant exposure for DSSW, DSLW, DSSW + DSLW, and Cloud Forcing cumulated from the beginning of the year. Red values indicate the largest occurring value for each type of radiant exposure for time period 2003 to 2007.

	Radiant Exposure Yearly Maximum Value (MJ m⁻²)			
	DSSW	DSLW	DSSW + DSLW	Cloud Forcing
2003	2551.83	7375.88	9927.71	191.81
2004	2680.28	7247.79	9928.07	151.32
2005	2849.85	7340.92	10190.77	203.75
2006	2611.31	7492.48	10103.79	288.73
2007	2650.15	7636.83	10286.98	219.96

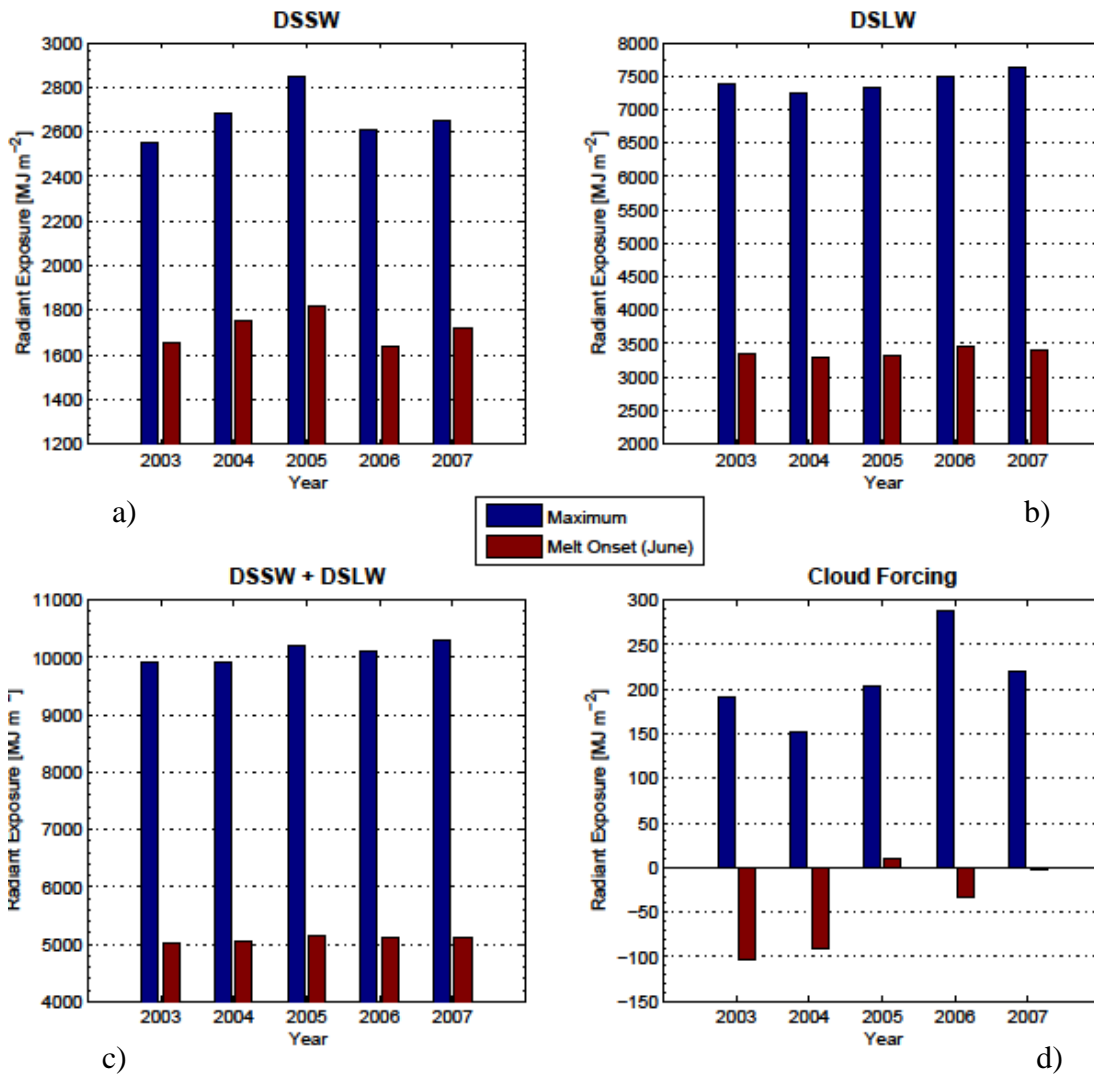


Figure 4.8 Maximum radiant exposure (blue bar) and radiant exposure cumulated until melt onset (red bar) for years 2003-2007 for DSSW (a), DSLW (b), DSSW + DSLW (c), and Cloud Forcing (d).

In addition to examining the maximum radiant exposure due to DSSW each year, which typically happens after the melt onset, we have examined the radiant exposure accumulated from the beginning of the year to the melt onset,

which is the month of June as shown by *Markus et al.* (2009). Again, both 2005 and 2004 exhibit larger radiant exposures for this condition as seen in Table 4.5 and a positive sea ice concentration anomaly exists throughout the year for the second highest radiant exposure accumulated until June. The numerical values of radiant exposure accumulated until melt onset are given in Table 4.5 and displayed in Figure 4.8.

Table 4.5 Radiant exposure for DSSW, DSLW, DSSW + DSLW, and Cloud Forcing cumulated from the beginning of the year to melt onset (June). Red values indicate the largest occurring value for each type of radiant exposure for time period 2003 to 2007.

	Radiant Exposure Until Melt Onset (June) (MJ m⁻²)			
	DSSW	DSLW	DSSW + DSLW	Cloud Forcing
2003	1652.66	3360.02	5012.69	-103.27
2004	1753	3288.84	5041.85	-90.88
2005	1819.38	3334.61	5153.99	11
2006	1639.75	3460.54	5100.28	-33.43
2007	1719.60	3405.39	5124.99	-2.81

The change in radiant exposure (DSSW) from melt onset (June) to the maximum decrease in sea ice anomaly for 2007 (October) is shown in Figure 4.9a. Figure 4.9d shows the change in the sea ice concentration anomaly from melt onset (June) to the maximum decrease in sea ice anomaly for 2007 (October). The gray area indicates regions where there was no change in sea ice concentration anomalies during this time. This figure shows the spatial distribution of the change in radiant exposure and sea ice concentration anomalies between June and October for 2007. The largest increases in DSSW occur over

regions of the Beaufort Sea, where there was an increase in the sea ice concentration anomaly as seen in Figure 4.9d. The regions that exhibit the largest decreases in sea ice concentration anomalies do not show any significant increase in DSSW for this period as compared to other regions.

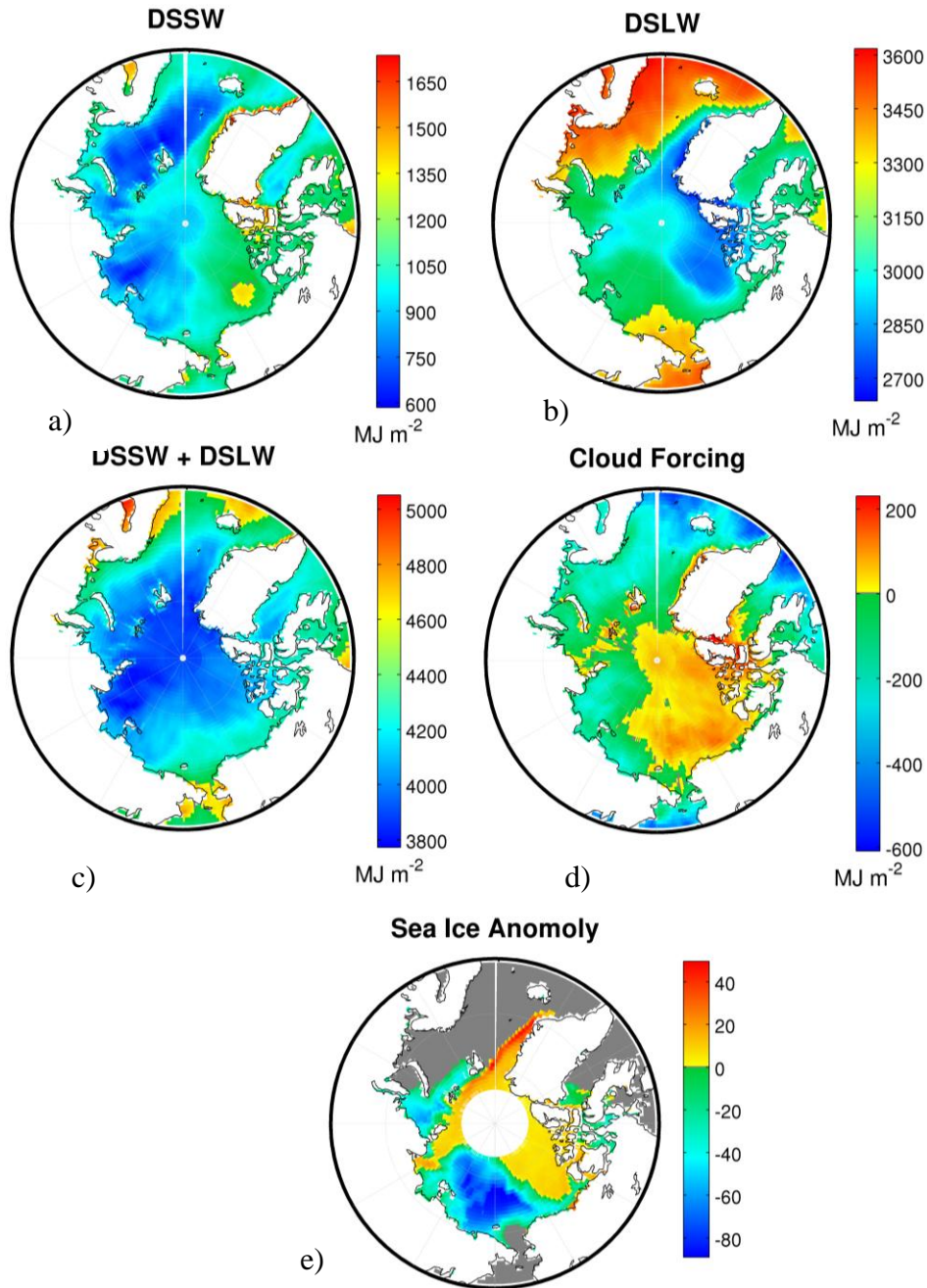


Figure 4.9 Plots a) through d) show the spatial distribution of the change in radiant exposure between melt onset (June) and the maximum decrease in sea ice concentration anomaly for 2007 (October). Plot e) shows the monthly average of the spatial distribution of the sea ice concentration anomaly for October 2007. Grey areas indicate areas with no change in radiant exposure or sea ice concentration anomaly.

The work of *Kay et al. (2008)* implies that the cloud fraction minimum in 2007 for the region they investigated implied an increase in DSSW (due to lack of clouds) that contributed to the record 2007 sea ice loss. Figure 4.10 shows the monthly averaged DSSW for the region we feel most captures the record 2007 sea ice loss. From this figure one can see that the maximum monthly DSSW occurred in June of 2005 corresponds to our analysis of cloud fraction for this region. The peak value for 2007 was less than that of 2005 and 2004.

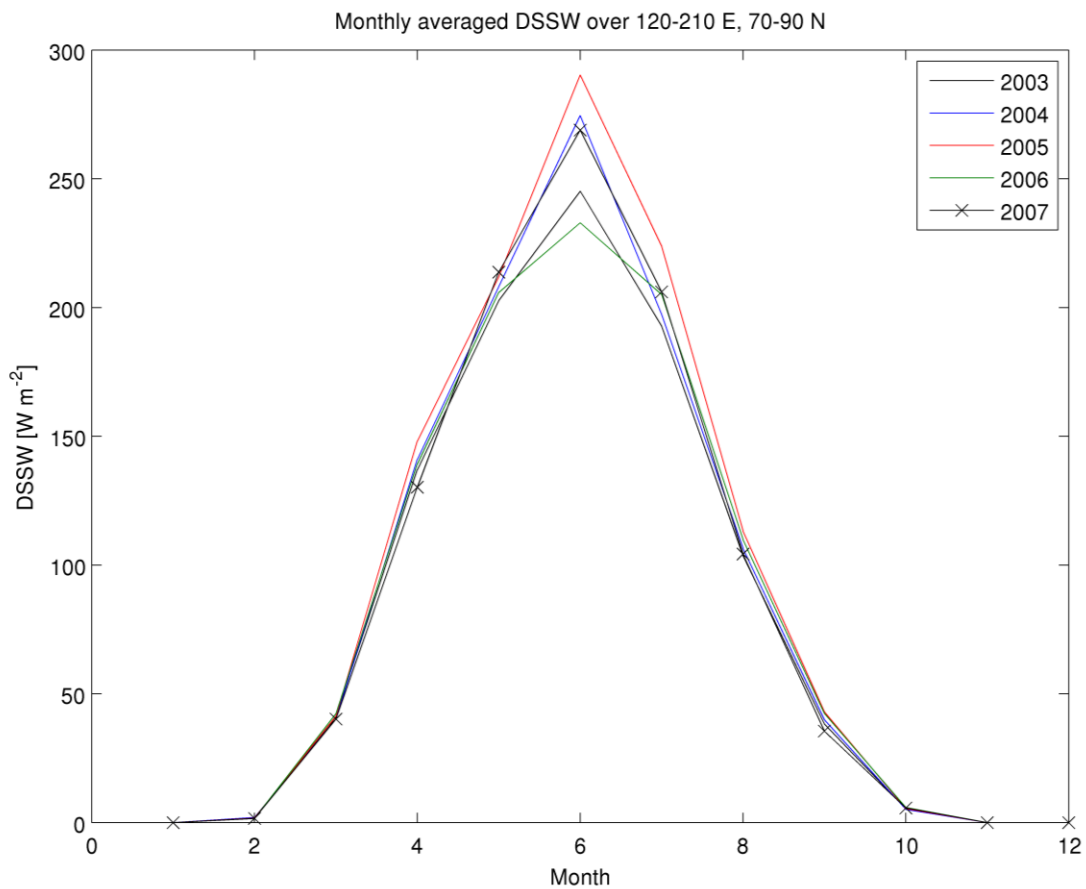


Figure 4.10 Monthly averaged DSSW for 120° E to 210° E and 70° N to 90° N.

In addition to examining whether DSSW is a primary driver to the sea ice concentration anomalies between 2003 and 2007, it is useful to examine the correlation between DSSW and sea ice concentration. It is important to once again point out that correlation does not imply causation. Just because two time series show strong correlation, one may not infer that there exists causation between them. Figure 4.11 shows the irradiance from DSSW, DSLW, DSSW + DSLW, and cloud forcing along with monthly sea ice concentration and climatology. This figure also confirms the previous assertion regarding the role of DSSW in sea ice concentration anomalies. The first figure of this graph shows that the largest monthly peak value in DSSW occurred in 2005.

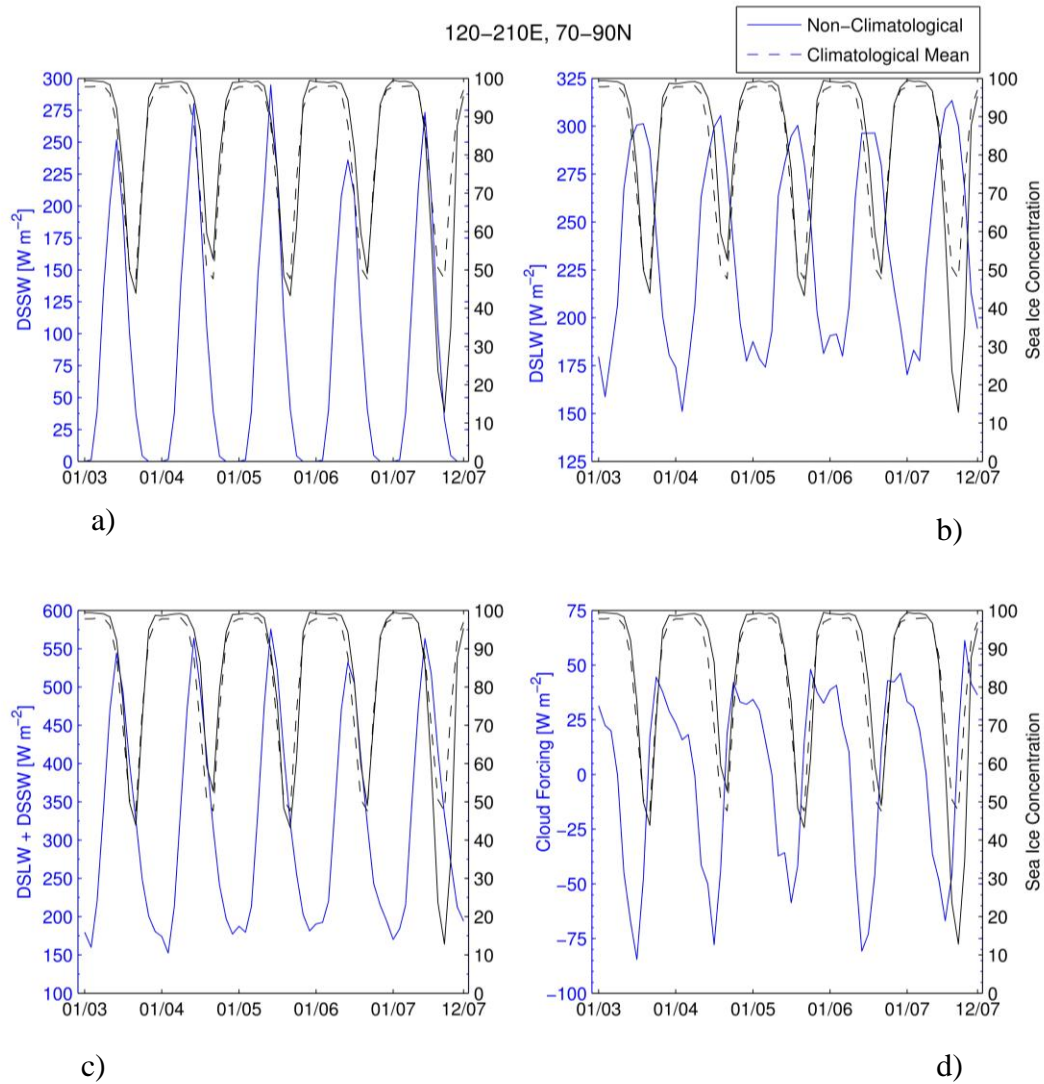


Figure 4.11 Monthly averaged irradiance (blue line) for DSSW (a), DSLW (b), DSSW + DSLW (c), and Cloud Forcing (d), monthly averaged observed sea ice concentration (black solid line) and monthly averaged sea ice concentration from climatology (black dashed line) bounded by 120° E to 210° E/70° N to 90° N.

The cross correlation between the radiative components and sea ice concentration is shown in Figure 4.12. The cross-correlation sequence is

normalized such that the autocorrelations at 0th lag are 1.0. A negative lag corresponds to radiation signal preceding the sea ice signal and a positive signal corresponds to the opposite. The dashed line indicates the 95% confidence interval.

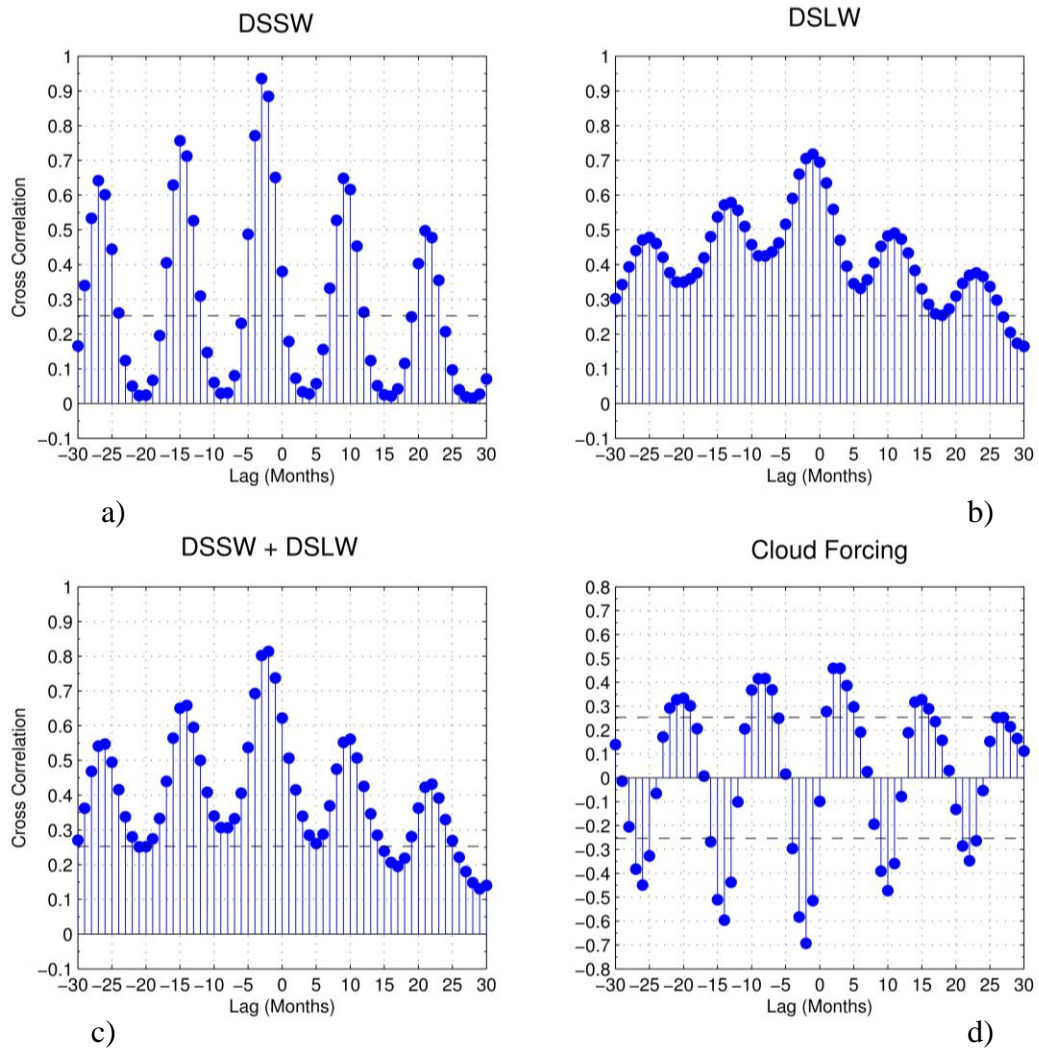


Figure 4.12 The cross correlation between radiative components and Arctic sea ice concentration for region 120° E to 210° E and 70° N to 90° N. A negative lag corresponds to radiation signal preceding the sea ice signal and a positive signal corresponds to the opposite. The dashed line indicates the 95% confidence interval.

It is clear from Figure 4.12a that there is a strong correlation between the DSSW irradiance and the Arctic sea ice concentration, with the radiative signal leading the sea ice concentration by about 3 months. There is good evidence that DSSW has some relationship to the melting of the Arctic sea ice; however, previous analysis indicates that it is most likely not the primary driver for the anomalies seen between 2003 and 2007.

4.3.4. DSLW

Figure 4.7b shows the accumulated radiant exposure for DSLW for each year along with the sea ice concentration anomaly. The maximum radiant exposure due to DSLW shows an increasing trend for each year, with the exception of 2003, which was larger than 2004 and 2005 (Table 4.2 and Figure 4.8). This is consistent with the trend of increasing temperatures in the Arctic. The change in sea ice will have an impact on the amount of DSLW received. Less ice allows for increased heat transport between the ocean and atmosphere, thereby increasing the DSLW. Therefore, in order to examine the role of DSLW in the 2007 anomaly it is useful to look at the radiant exposure due to DSLW accumulated until melt onset (Table 4.3 and Figure 4.8). The largest case for this value occurred in 2006. In addition, the values of DSLW radiant exposure accumulated until the melt onset do not correlate with the decrease in sea ice

concentration anomaly with the exception of 2004, which has the lowest values and also shows a net gain of sea ice through the year. The largest gain in DSLW radiant exposure between June and October occurs in 2007 and corresponds to the largest decrease in sea ice concentration anomaly. This demonstrates the positive feedback between melting sea ice and DSLW; however, considering the previous discussion, the direct influence of ice loss on DSLW may be more significant than the direct influence of DSLW on sea ice loss.

The change in radiant exposure (DSLW) from melt onset (June) to the maximum decrease in sea ice anomaly for 2007 (October) is shown in Figure 4.9a. This corresponds well with the loss of sea ice shown in Figure 4.9e. A larger increase in DSLW is seen in areas of larger sea ice loss. However, we rely on the fact that DSLW radiant exposure accumulated until melt onset was greatest during 2006, which corresponds to the fourth largest decrease in sea ice concentration anomaly (only larger than 2004). Although, the change in sea ice concentration has a strong effect on DSLW, DSLW is not the primary driver for seasonal sea ice concentration anomalies.

The correlation between DSLW irradiance and Arctic sea ice concentration as shown in Figure 4.11 is shown in Figure 4.12. There is a strong correlation between these two time-series with DSLW leading the sea ice concentration decrease by about a month. The lag between DSLW and sea ice concentration is less than the lag between DSSW and sea ice concentration.

4.3.5. DSLW + DSSW

Figure 4.7c shows the cumulated radiant exposure for DSLW and DSSW combined for each year along with the sea ice concentration anomaly. This represents the influence of total radiative energy. Because of the large influence of DSLW the maximum radiant exposure for DSLW + DSSW occurs in 2007. It is informative to look at radiant exposure of DSLW + DSSW prior to melt onset. The maximum value of radiant exposure accumulated until melt onset occurred during 2005, which coincides with the larger value of DSSW seen during this year.

The correlation between DSLW + DSSW irradiance and Arctic sea ice concentration as shown in Figure 4.11 is shown in Figure 4.12. There is a strong correlation between these two time-series, with DSLW + DSSW leading the sea ice concentration decrease by about 2 months. The lag between DSLW + DSSW and sea ice concentration is approximately the average of the lag between DSSW and sea ice concentration and DSLW and sea ice concentration.

4.3.6. Cloud Forcing

Cloud forcing in this study is defined as the difference in downwelling surface radiation between all sky and clear sky for both longwave and shortwave radiation. The maximum value of radiant exposure (289 MJ m^{-2}) due to cloud forcing, occurred in 2006 as seen in Figure 4.7, Figure 4.8, and Table 4.2. The maximum value was preceded by the second largest increase in sea ice

concentration anomaly behind 2004. The maximum radiant exposure prior to the 2007 sea ice concentration anomaly was the second highest 220 MJ m^{-2} .

The largest value of radiant exposure due to cloud forcing accumulated from the beginning of the year to melt onset occurs during 2005, which is the only year from 2003 to 2007 to have a positive value (11 MJ m^{-2}). All other years exhibit a net deficit in cloud forcing leading to melt onset. In 2003 the lowest value was achieved during this time period (-103 MJ m^{-2}); however, this year represents the third largest decrease in sea ice concentration anomaly, ahead of 2004 and 2006.

The change in radiant exposure (Cloud Forcing) from melt onset (June) to the maximum decrease in sea ice anomaly for 2007 (October) is shown in Figure 4.9d. The gray area in the last plot shows regions where there the net effect of cloud forcing is zero. This figure shows the spatial distribution of the change in radiant exposure June and October for 2007. It is evident from this figure that there exists significant regions including East Siberian and Laptev Sea where the cloud forcing from DSLW and DSSW was negative from June to October, yet there still was a large loss in sea ice. In addition, parts of the Beaufort Sea showed positive radiant exposure due to cloud forcing while increases in sea ice concentration anomalies occurred.

The lack of correlation of maximum radiant exposure and radiant exposure accumulated to the sea ice concentration anomaly points to the fact that cloud forcing from DSLW and DSSW is not a primary driver for the large seasonal anomalies in sea ice concentration. In addition, the lack of correlation between the

spatial distribution of cloud forcing from melt onset to October for 2007 and the maximum sea ice concentration anomaly show that cloud forcing was not the primary driver in the large 2007 sea ice concentration anomaly.

The correlation between cloud forcing irradiance and Arctic sea ice concentration as shown in Figure 4.11 is shown in Figure 4.12. There is a strong negative correlation between these two time-series with cloud forcing leading the sea ice concentration decrease by about 2 months. Negative correlation indicates that as the clouds influence causes a decrease in downwelling surface radiation (i.e., tendency to head toward negative forcing values), the sea ice concentration also decreases, which seems counter intuitive. Since we may not infer causality from correlation, it is educated speculation; however, the author believes that although analysis shows strong correlation between cloud forcing and sea ice concentration, there is no direct link between the two. It is possible that the cloud forcing is not strong enough to have an influence on the Arctic sea ice concentration and that there is an underlying phenomena that is modulating both of them. This phenomenon could be related to the seasonality of Arctic Sea ice melt and freeze. As winter darkness encompasses the Arctic, the cloud forcing will become positive as seen in Figure 4.11. This is because clouds will always emit longwave radiation from their surface. During the winter, there is little or no shortwave radiation for the cloud to block, so the cloud forcing becomes due to the longwave and is positive (*Wang and Key, 2005a*). The winter time also coincides with the accumulation of Arctic Sea ice. The opposite is true in the summer. The cloud forcing due to SW is more significant than the cloud forcing

due to longwave, thus giving the cloud forcing an overall negative value.

However, this also corresponds to the Arctic Sea ice melt season. So even though there is a negative forcing due to clouds there is a decrease in sea ice concentration.

4.4. Conclusion

We have examined the role of DSSW, DSLW, DSSW + DSLW, and cloud forcing in the seasonal sea ice concentration anomalies between 2003 and 2007 and findings indicate that these factors are not the primary driver for seasonal sea ice concentration anomalies during this time. We also examined the correlation between the irradiance values of DSSW, DSLW, DSSW + DSLW, and cloud forcing and the Arctic sea ice concentration. These are two different analyses: The former is investigating the role of radiation in the sea ice concentration anomalies or departures from the climatological means, while the latter is investigating the relationship or correlation between the radiative components and the sea ice concentration. Although the radiant exposure due to DSLW accumulated until melt onset does not correlate with seasonal sea ice anomalies, through Figure 4.9 we show that there is a spatial relationship between the change in radiant exposure due to DSLW from melt onset (June) to maximum decrease in sea ice concentration anomaly (October) and loss in sea ice. This highlights the importance of heat transport from open water to the atmosphere versus ice and snow.

To the extent that DSLW represents the atmospheric heat transport as a

change in atmospheric temperature and humidity, we show that this component of atmospheric circulation is not the primary driver of large seasonal sea ice concentration anomalies. Although the radiative components are not primary drivers for modulating the seasonal sea ice anomalies, they no doubt play a role as shown through correlations. Quantification of the extent of that role is important in understanding sea ice loss and will be the focus of future research.

Chapter 5: Conclusions and Future Plans

5.1. Conclusions and Summary

This dissertation outlines the evolution of a methodology to estimate one of the most important and difficult parts of the surface radiation budget, downwelling surface longwave radiation (DSLW). Applying this methodology at high latitudes, further insight is gained as to the primary driver of Arctic sea ice concentration anomalies.

The initial model to estimate DSLW is a parameterization based model (DSLW/UMD v1) to calculate DSLW based on the latest high resolution ERA-Interim re-analysis and 1° MODIS level-3 cloud parameters. This model was unique in several aspects. It was among the first models to derive DSLW utilizing high resolution MODIS satellite and ERA-Interim re-analysis data. In addition, the parameterization to calculate the clear sky contribution to DSLW is globally applicable based on radiative transfer model runs. Previous parameterizations were based on a small sample of data points with limited spatial and temporal resolution. DSLW/UMD v1 clear sky parameterization was developed using global ERA-Interim re-analysis data (over 42 million data points).

When DSLW/UMD v1 along and several other present day models used to calculate DSLW against a worldwide network of ground station observation, evaluation reveals that the DSLW/UMD v1 model has better agreement to ground observations and shows areas for potential improvement of estimating DSLW.

The evaluation also revealed potential areas of improvement for estimating DSLW. These areas included consideration of inversions for the clear sky contribution of DSLW and the modeling of cloud vertical structure for the cloud contribution to DSLW.

A new model is developed (DSLW/UMD v2) utilizing artificial neural networks to calculate the clear sky and cloud contribution to DSLW. An artificial neural network for calculating clear sky DSLW is developed based on the Rapid Radiative Transfer Model (RRTM), which utilizes the temperature at the first 15 pressure levels (as defined by ERA-Interim) above the surface, thereby accounting for inversions. Comparison with RRTM shows that the artificial neural network does an excellent job estimating clear sky DSLW with significant reduction in computation time and input data. An artificial neural network is developed to predict cloud base temperature based on data derived from an algorithm that co-located MODIS passive instrument data to CPR and CALIPO active instrument data. Evaluation shows that the artificial neural network significantly improves the estimate of cloud base temperature over the model developed by *Wang et al. (2000)*. The comparison of DSLW/UMD v2 with the global network of BSRN stations shows improvement over its predecessor (v1) especially in the high latitude regions.

With the goal in mind of investigating the role of DSLW as a primary driver behind Arctic sea ice concentration anomalies, a modified version of DSLW/UMD v2 is developed (DSLW/UMD v2 Polar) specifically to estimate DSLW in the Polar Regions by training the artificial neural networks with high

latitude data exclusively. DSLW data from DSLW/UMD v2 Polar and downwelling surface shortwave data (DSSW) from a UMD developed model utilizing MODIS data are used to determine role of radiation in Arctic sea ice anomalies between 2003 and 2007. DSLW, DSSW, and cloud forcing from both shortwave and longwave were investigated as primary drivers for Arctic sea ice concentration anomalies. Previous studies showed conflicting results, where *Kay et al.* (2008) demonstrated that DSSW played a significant role in the 2007 Arctic sea ice concentration anomaly and *Schweiger et al.* (2007) showed through model runs that DSSW was not a primary driver. The analysis presented in this dissertation is the first known presentation of observational data showing that DSSW was not a primary driver in Arctic sea ice concentration anomalies especially in 2007. The analysis is also extended to longwave and cloud forcing. We show that there is a strong feedback from sea ice loss to DSLW; however, our analysis shows that DSLW was most likely not the primary driver for the large 2007 Arctic sea ice concentration anomaly. In addition, we investigated the role of cloud forcing in the realm of shortwave and longwave radiation. The analysis shows that cloud forcing is also not a primary driver for the Arctic sea ice concentration anomalies.

5.2. Future Plans

As is true for most models, the DSLW/UMD model continues to be a work in progress. Several areas of improvement have been identified. The current

cloud input data from MODIS is 1° equal angle gridded data. The NASA/Goddard MODIS Atmospheric team also provides raw satellite data at a 5 km degree resolution. The first modification of DSLW/UMD is to adapt the model to incorporate MODIS 5-km resolution cloud data. This would not affect the calculation of clear sky contribution to DSLW as it is dependent on meteorological parameters from ERA-Interim. The potential influence of higher resolution data on the cloud contribution to DSLW could be substantial. At the equator, going from 1° resolution to 5 km is equivalent to going from a 12388 km^2 cell to a 25 km^2 cell.

The DSLW/UMD model estimates downwelling longwave radiation only at the surface. The second modification to the model will be to create a layered model, such that upwelling and downwelling longwave radiation will be calculated at the surface as well as pre-defined intervals within the atmosphere. This will be accomplished by creating an artificial neural network to handle each atmospheric layer. A layered model is useful in calculating heating rates for different levels within the atmosphere.

In addition to model development, a planned future application of the DSLW/UMD model includes an update to the global investigation of the effects of cloud forcing on surface radiation. Previous studies on the global effect of cloud forcing have relied on ISCCP and Earth Radiation Budget Experiment (ERBE) data (launched in 1984). Our analysis showing the large discrepancy between ISCCP-FD estimates of DSLW and ground station data globally along with the recent availability of high quality and high resolution MODIS and ERA-

Interim make it timely to revisit this topic.

Bibliography

- llen, M. R., and W. J. Ingram, 2002: Constraints on future changes in climate and the hydrological cycle. *Nature*, **419**, 224-232.
- Belchansky, G. I., D. C. Douglas, and N. G. Platonov, 2004: Duration of the Arctic Sea Ice Melt Season: Regional and Interannual Variability, 1979-2001. *J. Climate.*, **17**, 67-80.
- Boer, G. J., 1993: Climate changes and the regulation of the surface moisture and energy budgets. *Climate Dyn.*, **8**, 225-239.
- Brutsaert, W., 1975: On a Derivable Formula for Long-Wave Radiation Form Clear Skies. *Water Resour. Res.*, **11**, 742-744.
- Cavalieri, D., C. Parkinson, P. Gloersen, and H. J. Zwally, 1996, updated 2008: Sea ice concentrations from Nimbus-7 SMMR and DMSP SSM/I passive microwave data [2007]. Boulder, Colorado USA: National Snow and Ice Data Center. Digital media.
- Chevallier, F., F. Cheruy, N. A. Scott, and A. Chedin, 1998: A neural network approach for a fast and accurate computation of longwave radiative budget. *J. Appl. Meteor.*, **37**, 1385-1397.
- Chevallier, F., J.-J. Morcrette, F. Cheruy, and N. A. Scott, 2000: Use of a neural-network-based longwave radiative transfer scheme in the EMCWF atmospheric model. *Quart. J. Roy. Meteor. Soc.*, **126**, 761-776.
- Clough, S. A., and M. J. Iacono, 1995: Line-by-line calculation of atmospheric fluxes and cooling rates 2. Application to carbon dioxide, ozone, methane,

- nitrous oxide and the halocarbons. *J. Geophys. Res.*, **100**, 16519-16535.
- Coakley, J. A., R. D. Cess, and F. B. Yurevich, 1983: The effect of tropospheric aerosol on the Earth's radiation budget: A parameterization for climate models. *J. Atmos. Sci.*, **40**, 116-138.
- Collins, W. D., 2001: Parameterization of generalized cloud overlap for radiative calculations in general circulation models. *J. Atmos. Sci.*, **58**, 3224-3242.
- Comiso, J., 1999, updated 2008: Bootstrap Sea Ice Concentrations from Nimbus-7 SMMR and DMSP SSM/I, 2003-2007. Boulder, Colorado USA: National Snow and Ice Data Center. Digital media.
- Cox, S. K., 1976: Observation of cloud infrared effective emissivity. *J. Atmos. Sci.*, **33**, 287-289.
- Dilley, A. C., and D. M. O'Brien, 1998: Estimating downward clear sky long-wave irradiance at the surface from screen temperature and precipitable water. *Q. J. R. Meteorol. Soc.*, **124**, 1392-1401.
- Dreyfus, G., 2004: *Neural networks: Methodology and applications*. Springer, 497 pp.
- Fu, Q., K-N. Liou, M. C. Cribb, T. P. Charlock, and A. Grossman, 1997: Multiple scattering parameterization in thermal infrared radiative transfer. *J. Atmos. Sci.*, **54**, 2799-2812.
- Gao B-C., P. Yang, G. Guo, S. K. Park, W. J. Wiscombe, and B. Chen, 2003: Measurements of water vapor and high clouds over the Tibetan Plateau with the Terra MODIS instrument. *IEEE T. Geosci. Remote.*, **41**, 895-900.
- Garratt, J. R., and A. J. Prata, 1995: Downwelling longwave fluxes at continental

surfaces – A comparison of observations with GCM simulations and implications for the global land-surface radiation budget. *J Climate*, 9, 646-655.

GLOBALVIEW-CH4: Cooperative Atmospheric Data Integration Project – Methane. CD-ROM, NOAA ESRL, Boulder Colorado [Also available on Internet via anonymous FTP to *ftp.cmdl.noaa.gov*, Path: *ccg/ch4/GLOBALVIEW*], 2009.

Gupta, S. K., 1989: A parameterization for longwave surface radiation from sun-synchronous satellite data. *J. Climate.*, **2**, 305-320.

Gupta, S .K., W. L. Darnell, and A. C. Wilber, 1992: A parameterization for longwave surface radiation from satellite data: recent improvements. *J. Appl. Meteor.*, **31**, 1361-1367.

Hagan, M., and M. Menhaj, 1994: Training feedforward networks with the Marquardt algorithm, *IEEE T. Neural. Networ.*, 5, 989-993.

Hornik, K., 1991: Approximation capabilities of multilayer feedforward networks. *Neural Networks*, 4, 251-257.

Idso, S. B., and R. D. Jackson, 1969: Thermal radiation from the atmosphere. *J. Geo. Res.*, **74**, 5397-5403.

Johannessen, O. M., M. W. Miles, and E. Bjorgo, 1996: Global sea-ice monitoring from microwave satellites, *Proc. 1996 IGARSS*, 932-934.

Kay, J. E., T. L'Ecuyer, A. Gettelman, G. Stephens, and C. O'Dell, 2008: The contribution of cloud and radiation anomalies to the 2007 Arctic sea ice extent minimum, *J. Geophys. Res. Lett.*, 35, L08503,

doi:10.1029/2008GL033451.

- Kiehl, J. T., and K. E. Trenberth, 1997: Earth's annual global mean energy budget. *B. AM. Meteorol. Soc.*, 78, 197-208.
- Krasnopolsky, V. M., 2007: Neural network emulations for complex multidimensional geophysical mappings: Applications of neural network techniques to atmospheric and oceanic satellite retrievals and numerical models. *Reviews of Geophysics*, 45, 34pp.
- Krasnopolsky, V. M, M. S. Fox-Rabinovitz, and D. V. Chalikov, 2005: New approach to calculation of atmospheric model physics: Accurate and fast neural network emulation of longwave radiation in a climate model. *Mon. Weather Rev.*, 133, 1370-1383.
- Krose, B. and P. van der Smagt, 1996: *An introduction to neural networks*. The University of Amsterdam, 135 pp.
- Lee, H-T., and R. G. Ellingson, 2002: Development of a nonlinear statistical model for estimating the downward longwave radiation at the surface from satellite observations. *J Atmos Ocean Tech.*, **19**, 1500-1515.
- Lind, R. J., and K. B. Katsaros, 1982: A model for longwave irradiance for use with surface observations. *J. Appl. Met.*, **21**, 1015-1023.
- Mace, G. G., R. Marchand, Q. Zhang, and G. Stephens, 2007: Global hydrometeor occurrences as observed by CloudSat: Initial observations from summer 2006. *Geophys Res Lett*, 34, 5 pp.
- Markus, T., J.C. Stroeve, and J. Miller, 2009: Recent changes in Arctic sea ice melt onset, freezeup, and melt season length, *J. Geophys. Res.*, **114**,

C12024, doi:10.1029/2009JC005436.

- Marquardt, D. W., 1963: An algorithm for least-squares estimation of nonlinear parameters. *Journal of the Society for Industrial and Applied Mathematics*, **11**, 431-441.
- Martin, M., and P. Berdahl, 1984: Characteristics of infrared sky radiation in the United States. *Sol Energy.*, **33**, 321-336.
- Mitchell, J. B., 1983: The seasonal response of a general circulation model to changes in CO₂ and sea temperatures. *Quart. J. Roy. Meteor. Soc.*, **109**, 113-152.
- Mitchell, J. B., C. A. Wilson, and W. M. Cunningham, 1987: On CO₂ climate sensitivity and model dependence of results. *Quart. J. Roy. Meteor. Soc.*, **113**, 293-322.
- Mlawer, E. J., S. J. Taubman, P. D. Brown, M. J. Iacono, S. A. Clough, 1997: Radiative transfer for inhomogenous atmospheres: RRTM, a validated correlated-k model for the longwave. *J. Geophys. Res.*, **102**, 16663-16682.
- Moody, E. G., M. D. King, C. B. Schaaf, D. K. Hall, and S. Platnick, 2007: North hemisphere five-year average (2000-2004) spectral albedos of surface in the presence of snow: statistics computed from Terra MODIS land products. *Remote Sens. Environ.*, **111**, 337-345.
- Morcrette, J., 2002: The surface downward longwave radiation in the ECMWF forecast system. *J. Climate.*, **15**, 1875-1892.
- Nghiem, S. V., I.G. Rigor, D. K. Perovich, P. Clemente-Colon, J. W. Weatherly, and G. Neumann, 2007: Rapid reduction of Arctic perennial sea ice, *J.*

- Geophys. Res. Lett.*, **34**, L19504, doi:10.1029/2007GL031138.
- Niemela, S., P. Raisanen, and H. Savijarvi, 2001: Comparison of surface radiative flux parameterizations Part I: Longwave radiation. *Atmos Res.*, **58**, 18pp.
- Niu, X., R.T. Pinker, and M. F. Cronin, 2010: Radiative fluxes at high latitudes, *J. Geophys. Res. Lett.*, **37**, L20811, doi:10.1029/2010GL044606.
- Nussbaumer, E. A., and R. T. Pinker, 2011: Estimating Surface Longwave Radiative Fluxes at Global Scale. *Q. J. Roy. Meteor. Soc.* [In Press].
- Nussbaumer, E. A., R. T. Pinker (2012), Estimating surface longwave radiative fluxes from satellites utilizing artificial neural networks, *J. Geophys. Res-Atmos.*, [In Press].
- Ogi, M., and J. M. Wallace, 2007: Summer minimum Arctic sea ice extent and the associated summer atmospheric circulation, *J. Geophys. Res. Lett.*, **34**, L12705, doi:10.1029/2007GL029897.
- Perovich, D. K., B. Light, H. Eicken, K. F. Jones, K. Runciman, and S. V. Nghiem, 2007a: Increasing solar heating of the Arctic Ocean and adjacent seas, 1979-2005: Attribution and role in the ice-albedo feedback, *J. Geophys. Res. Lett.*, **34**, L19505, doi:10.1029/2007GL031480.
- Perovich, D. K., S. V. Nghiem, T. Markus, and A. Schweiger, 2007b: Seasonal evolution and interannual variability of the local solar energy absorbed by the Arctic sea ice-ocean system, *J. Geophys. Res.*, **112**, C03005, doi:10.1029/2006JC003558.
- Perovich, D. K., J. A. Richter-Menge, K. F. Jones, and B. Light. 2008: Sunlight, water, and ice: Extreme Arctic sea ice melt during the summer of 2007, *J.*

- Geophys. Res. Lett.*, **35**, L11501, doi:10.1029/2008GL034007.
- Platt, C. R., and K. Bartusek, 1974: Structure and optical properties of some middle-level clouds. *J. Atmos. Sci.*, **31**, 1079-1088.
- Poore, K., J-H. Wang, and W. B. Rossow, 1995: Cloud layer thickness from a combination of surface and upper-air observations. *J. Climate.*, **8**, 550-558.
- Post, E., et al., 2009: Ecological dynamics across the Arctic associated with recent climate change, *Science*, **325**, doi:10.1126/science.1173113.
- Prata, A. J., 1996: A new long-wave formula for estimating downward clear-sky radiation at the surface. *Q. J. R. Meteorol. Soc.*, **122**, 1127-1151.
- Ramanathan, V., 1986: Scientific use of surface radiation budget data for climate studies, surface radiation budget for climate applications edited by J. T. Shutles and G. Ohring, Publ. 1169, NASA, Washington D.C.
- Rigor, I. G., and J. M. Wallace, 2004: Variations in the age of Arctic sea-ice and summer sea-ice extent, *J. Geophys. Res. Lett.*, **31**, L09401, doi:10.1029/2004GL019492.
- Rumelhart, D. E, G. E Hinton, and R. J. Williams, 1986: Learning representations by back-propagation errors. *Nature*, 323, 533-536.
- Schmetz, P., J. Schmetz, and E. Raschke, 1986: Estimation of daytime downward longwave radiation at the surface from satellite and grid point data. *Theor. Appl. Climatol.*, **37**, 136-149.
- Schweiger, A. J., J. Zhang, R. W. Lindsay, and M. Steele, 2008: Did unusually sunny skies help drive the record sea ice minimum of 2007? *J. Geophys.*

- Res. Lett.*, **35**, L10503, doi:10.1029/2008GL033463.
- Serreze, M. C., M. M. Holland, and J. Stroeve, 2007: Perspectives on the Arctic's shrinking sea-ice cover, *Science*, **315**, 1533-1536, doi:10.1126/science.1139426.
- Shimada, K., T. Kamoshida, M. Itoh, S. Nishino, E. Carmack, F.A. McLaughlin, S. Zimmermann, and A. Proshutinsky, 2006: Pacific Ocean inflow: Influence on catastrophic reduction of sea ice cover in the Arctic Ocean, *J. Geophys. Res. Lett.*, **33**, L08605, doi:10.1029/2005GL025624.
- Stackhouse, P. W., S. K. Gupta, S. J. Cox, M. Chiacchio, and J. C. Mikovitz, 2000: The WCRP/GEWEX surface radiation budget project release 2: an assessment of surface fluxes at 1 degree resolution. Technical Report. UMI Order Number: NASA-2000-irs-pws. NASA-2000-irs-pws. NASA Langley Technical Report Server.
- Stephens, G. L., D. L. Jackson, and J. J. Bates, 1994: A comparison of SSM/I and TOVS column water vapor data over the global oceans. *Meteorol. Atmos. Phys.*, **54**, 183-201.
- Stephens, G. L., and P. J. Webster, 1981: Clouds and climate: Sensitivity of simple systems. *J. Atmos. Sci.*, **38**, 235-247.
- Stephens, G. L., and P. J. Webster, 1984: Cloud decoupling of the surface and planetary radiative budgets. *J. Atmos. Sci.*, **41**, 681-686.
- Stroeve, J., M. Serezze, S. Drobot, S. Gearheard, M. Holland, J. Maslanik, W. Meier, and T. Scambos, 2008: Arctic sea ice plummets in 2007, *Eos Trans. AGU*, **89**, 13.

- Swinbank, W. C., 1963: Long-wave radiation from clear skies. *Q. J. R. Meteorol. Soc.*, **89**, 339-348.
- United States Geological Survey (USGS), 2008: 90 Billion Barrels of Oil and 1,670 Trillion Cubic Feet of Natural Gas Assessed in the Arctic [Press release]. Retrieved from http://www.usgs.gov/newsroom/article.asp?ID=1980&from=rss_home
- Wang, H., and R. T. Pinker, 2009: Shortwave radiative fluxes from MODIS: Model development and implementation, *J. Geophys. Res.*, **114**, D20201, doi:10.1029/2008JD010442.
- Wang, J., and W. B. Rossow, 1995: Determination of cloud vertical structure from upper-air observations. *J. Appl. Meteor.*, **34**, 2243-2258.
- Wang, J., W. B. Rossow, and Y. Zhang, 2000: Cloud vertical structure and its variations from a 20-yr global rawinsonde dataset. *J. Climate.*, **13**, 3041-3056.
- Wang, X., and J. Key, 2003: Recent trends in Arctic surface, cloud, and radiation properties from space. *Science*, **299** (5613), 1725-1728.
- Wang, X., and J. Key, 2005a: Arctic surface, cloud, and radiation properties based on the AVHRR Polar Pathfinder dataset. Part I: Spatial and temporal characteristics. *J. Clim.*, **18**, 2558-2574.
- Wang, X., and J. Key, 2005b: Arctic surface, cloud, and radiation properties based on the AVHRR Polar Pathfinder dataset. Part II: Recent trends. *J. Clim.*, **18**, 2575-2593.
- Wild, M., A. Ohmura, and U. Cubasch, 1997: GCM-Simulated surface energy

- fluxes in climate change experiments. *J. Climate*, 10, 3093-3110.
- Wild, M., A. Ohmura, and H. Gilgen, 2001: Evaluation of Downward Longwave Radiation in General Circulation Models. *J. Climate*, 14, 3227-3239.
- Wild, M. and R. Cechet, 2002: Downward longwave radiation in general circulation models: A case study at a semi-arid continental site. *Tellus Ser. A.*, 54, 330-337.
- WCRP-5, 1985: First implementation plan for the World Climate Research Program. WCRP Publication Series 5 (WMO/TD-No. 80), 123pp.
- Zhang, T., T. Scambos, T. Haran, L. D. Hinzman, R. G. Barry, and D. L. Kane, 2003: Ground-based and satellite-derived measurements of surface albedo on the North Slope of Alaska. *J. Hydrometeorology*, 4, 77-91.
- Zhang, Y-C., W. B. Rossow, A. A. Lacis, V. Oinas, and M. I. Mishchenko. 2004: Calculation of radiative fluxes from the surface to top of atmosphere based on ISCCP and other global data sets: Refinements of the radiative transfer model and the input data. *J. Geophys. Res.*, 109, 27pp.
- Zhao, W., W. R. Kuhn, and S. R. Drayson, 1994: The significance of detailed structure in the boundary layer to thermal radiation at the surface in climate models. *Geophys. Res. Lett.*, 21, 1631-1634.
- Zhou, Y., D. P. Kratz, A. C. Wilber, S. K. Gupta, and R. D. Cess, 2007: An improved algorithm for retrieving surface downwelling longwave radiation from satellite measurements. *J. Geophys. Res.*, 112, 13pp.